First-Principles Study of Phonon-Assisted Optical Properties and Exciton Dynamics

by

Chunhao Guo

A dissertation submitted in partial fulfillment of
the requirements for the degree of

Doctor of Philosophy

(Materials Science and Engineering)

at the

UNIVERSITY OF WISCONSIN–MADISON

2025

Date of final oral examination: May 7, 2025

The dissertation is approved by the following members of the Final Oral Committee:
Yuan Ping, Associate Professor, Materials Science and Engineering
Dane Morgan, Harvey D. Spangler Professor of Engineering, Materials Science and Engineering
Jun Xiao, Assistant Professor, Materials Science and Engineering
Elio König, Assistant Professor, Physics
Ilya Esterlis, Assistant Professor, Physics

This thesis is dedicated to my family, whose unwavering support and encouragement have been invaluable throughout this journey.

Acknowledgments

I am deeply grateful to my advisor, Professor Yuan Ping, for her invaluable support, guidance, and mentorship throughout my Ph.D. journey. When I first joined the group, I had very limited knowledge of ab initio calculations and the underlying physics. Professor Ping spent considerable time helping me work through technical details, patiently discussing challenges, and offering insightful guidance as I navigated the complexities of research. She also made every effort to connect me with leading experts in the field, arranging valuable discussions that greatly helped me overcome difficult problems. I am truly fortunate to have pursued my Ph.D. under her high standards and professional mentorship, which not only deepened my academic foundation but also equipped me with critical research skills that will be essential for my future career.

I would also like to sincerely thank all members of my committee — Professor Dane Morgan, Professor Jun Xiao, Professor Elio König, and Professor Ilya Esterlis — for their valuable feedback and encouragement during my preliminary exam and thesis preparation. I am especially thankful to Professor Dane Morgan and Professor Jun Xiao for their thoughtful suggestions, which helped me improve the presentation of my research and better connect my work to broader scientific questions. I am also grateful to Professor Elio König and Professor Ilya Esterlis for organizing the APS March Meeting practice session and providing constructive feedback, which was instrumental in strengthening both my understanding of the physical picture and my scientific communication skills.

I am deeply thankful to our former postdoctoral researchers, Dr. Feng Wu and Dr. Junqing Xu, for their indispensable assistance in setting up computational resources and carefully verifying every step of the theoretical derivations we worked on together. Completing my first project on substrate screening with such high quality would not have been possible without their guidance and collaboration. I would also like to express my sincere appreciation to Dr. Gabriele Riva and Dr. Jacopo Simoni for their continuous support on my most recent project on radiative lifetimes and exciton-phonon coupling. They devoted considerable time to scientific discussions and carefully reviewing every aspect of the derivations and implementations, for which I am truly grateful.

Finally, I would like to thank all former and current members of our research group for their support and collaboration. It has been a truly rewarding and memorable experience to work and grow together throughout my Ph.D. journey.

Contents

List of Tables

List of Figures

Abstract

Exciton-phonon interactions play a fundamental role in phonon-assisted radiative recombination and exciton dynamics in solids. In this work, we present a first-principles framework for computing phonon-assisted radiative lifetimes and exciton relaxation dynamics at finite temperatures. Starting from the solution of the Bethe-Salpeter equation, we construct an effective excitonic Hamiltonian that incorporates both exciton-photon and exciton-phonon interactions. Phonon-assisted radiative lifetimes in anisotropic media are evaluated using time-dependent second-order perturbation theory. We further analyze the temperature and phonon-mode dependence of the phonon-assisted radiative lifetime and compare our results with available experimental data. In particular, we explain the nonmonotonic temperature dependence of the lifetime by identifying distinct mechanisms governing the low- and high-temperature regimes. To capture out-of-equilibrium dynamics, we perform real-time exciton relaxation simulations within the diagonal approximation of Lindbladian dynamics, providing direct insights into ultrafast thermalization and scattering pathways. In addition, we developed a reciprocal-space linear interpolation method for dielectric matrices that efficiently accounts for substrate screening effects in quasiparticle and excitonic properties of arbitrarily lattice-mismatched 2D interfaces, without introducing artificial strain. This advancement enables a systematic investigation of substrate-induced screening effects on quasiparticle energies and optical properties. Overall, our *ab-initio* theory provides a detailed microscopic understanding of phonon-mediated exciton relaxation, recombination processes, and substrate effects, offering valuable perspectives on phonon-assisted many-body interactions and their influence on optical phenomena in light-emitting and optoelectronic materials.

Chapter 1

Introduction

Exciton-phonon interactions play a fundamental role in governing the optical and transport properties of semiconductors. In particular, they are essential for describing phonon-assisted radiative processes and exciton dynamics in materials with indirect band gaps, where phonons are required to satisfy momentum conservation during photon emission. These phonon-mediated optical transitions are especially relevant in layered van der Waals (vdW) materials and other quantum systems, where the interplay between electronic many-body effects and lattice vibrations gives rise to rich and unconventional physical behavior [116, 94, 11].

Over the past decades, substantial progress has been made in the theoretical and computational understanding of excitons, which are quasiparticles of electron-hole pairs. This progress has been enabled by first-principles many-body perturbation theory (MBPT) based on the Bethe-Salpeter equation (BSE) [99, 35, 23, 77]. The BSE, typically built on top of quasiparticle corrections from the GW approximation, has successfully predicted exciton binding energies, finite-momentum dispersion [82], exciton-phonon scattering rates [4, 19], and optical spectra in both bulk and low-dimensional systems [83, 99]. However, most existing BSE applications focus on first-order or direct optical transitions [126, 72, 18] and do not capture phonon-assisted recombination processes, which require a second-order treatment involving both exciton-photon and exciton-phonon couplings.

Phonon-assisted luminescence, such as the indirect photoluminescence (PL) observed in hexagonal boron nitride (hBN) [116, 94], monolayer WSe_2 [11], and silicon [57], cannot be described using first-order optical processes alone. Instead, a second-order process involving both exciton and phonon interactions must be considered. Despite their significance, a fully *ab initio* many-body framework for computing phonon-assisted radiative lifetimes still remains to be developed. Earlier efforts have formulated such transitions at the single-particle level [64, 73, 110] or have treated exciton-photon and exciton-phonon in-

teractions separately [11, 19, 54], potentially missing the coupling effects between different scattering pathways [17].

In this work, we present a rigorous many-body formalism to compute phonon-assisted radiative lifetimes and simulate time-resolved exciton dynamics from first principles. Our approach is based on constructing an effective exciton-photon-phonon Hamiltonian in second quantization, combining excitonic states from the finite-momentum BSE [99] with exciton-phonon coupling derived from first-principles electron-phonon matrix elements [32, 4, 71, 19]. Radiative rates are evaluated using time-dependent second-order perturbation theory [98], with both phonon emission and absorption channels treated explicitly.

To capture out-of-equilibrium exciton dynamics in open quantum systems, we derive a quantum master equation in the Lindblad form [92, 91, 128, 131], which governs the evolution of the exciton density matrix under phonon scattering. In the semiclassical limit, this formulation reduces to the Boltzmann transport equation (BTE) [93, 49], enabling real-time simulation of exciton relaxation and thermalization. This framework also provides a foundation for future studies of exciton coherence, dephasing, and spin dynamics in realistic material systems.

In addition to phonon-assisted exciton dynamics, this thesis also addresses the challenge of accurately predicting quasiparticle energies in 2D interface systems with strong substrate screening effects. Two-dimensional materials provide an outstanding platform for exploring new physics and device applications, particularly when combined to form interfaces. Substrates can significantly modify the electronic structure of 2D materials, often requiring sophisticated many-body treatments for accurate predictions. In our earlier work [39], we developed a reciprocal-space linear interpolation method that enables substrate screening effects to be incorporated into GW calculations of arbitrarily mismatched interfaces, without applying artificial strain. We benchmarked this approach using hBN/SnS_2 heterostructures and hBN bilayers, and showed that it yields excellent agreement with explicit interface GW calculations.

We further extended this framework to excitonic properties by solving the substrate-screened BSE on top of substrate-screened GW calculations. In particular, we demonstrated the nonrigid shift of excitonic 1s and 2s peaks in supported monolayer hBN due to substrate screening, and provided a simple physical model based on the 2D hydrogenic exciton. Finally, we calculated exciton radiative lifetimes for monolayer hBN and WS_2 on various substrates at both zero and room temperatures, showing quantitative agreement with experimental data. These results highlight the importance of substrate effects in accurately modeling the excitonic behavior of 2D interfaces.

Chapter 2

Theoretical Background

2.1 Field operator

In the second quantization formalism [25, 2, 106], a single particle at position $\mathbf{x}$ in a many-particle system is created by the action of the field operator $\hat{\psi}^\dagger(\mathbf{x})$ on the vacuum state $|0\rangle$. This operation defines the single-particle state as $|\mathbf{x}\rangle = \hat{\psi}^\dagger(\mathbf{x})\,|0\rangle$. Here, $\mathbf{x} = (\mathbf{r}, \sigma)$ represents the combined index of the particle's spatial position $\mathbf{r}$ and spin polarization σ. By definition of the state overlap, the following identity holds:

$$\delta(\mathbf{y}-\mathbf{x}) = \langle \mathbf{y}|\mathbf{x}\rangle = \langle \mathbf{y}|\,\hat{\psi}^\dagger(\mathbf{x})\,|0\rangle = \langle 0|\,\hat{\psi}(\mathbf{x})\,|\mathbf{y}\rangle^* . \tag{2.1}$$

Applying Eq. (2.1) to an N-particle state $|\mathbf{y}_1 \cdots \mathbf{y}_N\rangle$, and utilizing the antisymmetric property of fermionic states, the state overlap $\langle \mathbf{x}_1 \cdots \mathbf{x}_N|\,|\mathbf{y}_1 \cdots \mathbf{y}_N\rangle$ can be expressed as:

$$\langle \mathbf{x}_1 \cdots \mathbf{x}_{N-1}|\,\hat{\psi}(\mathbf{x}_N)\,|\mathbf{y}_1 \cdots \mathbf{y}_N\rangle = \sum_{k=1}^{N} (-1)^{N+k} \delta(\mathbf{x}_N - \mathbf{y}_k)\,\langle \mathbf{x}_1 \cdots \mathbf{x}_{N-1}|\,|\mathbf{y}_1 \cdots \mathbf{y}_{k-1}\mathbf{y}_{k+1} \cdots \mathbf{y}_N\rangle . \tag{2.2}$$

This leads to the general relation:

$$\hat{\psi}(\mathbf{x})\,|\mathbf{y}_1 \cdots \mathbf{y}_N\rangle = \sum_{k=1}^{N} (-1)^{N+k} \delta(\mathbf{x} - \mathbf{y}_k)\,|\mathbf{y}_1 \cdots \mathbf{y}_{k-1}\mathbf{y}_{k+1} \cdots \mathbf{y}_N\rangle . \tag{2.3}$$

To compute the composite action of $\hat{\psi}(\mathbf{x})\hat{\psi}^\dagger(\mathbf{y})$ on the N-particle state $|\mathbf{y}_1 \cdots \mathbf{y}_N\rangle$, we proceed as follows:

$$\hat{\psi}(\mathbf{x})\hat{\psi}^{\dagger}(\mathbf{y})\,|\mathbf{y}_1\cdots\mathbf{y}_N\rangle = \hat{\psi}(\mathbf{x})\,|\mathbf{y}_1\cdots\mathbf{y}_N\mathbf{y}\rangle \tag{2.4}$$

$$= \delta(\mathbf{x}-\mathbf{y})\,|\mathbf{y}_1\cdots\mathbf{y}_N\rangle + \sum_{k=1}^{N}(-1)^{N+k+1}\delta(\mathbf{x}-\mathbf{y}_k)\,|\mathbf{y}_1\cdots\mathbf{y}_{k-1}\mathbf{y}_{k+1}\cdots\mathbf{y}_N\mathbf{y}\rangle \tag{2.5}$$

$$= \delta(\mathbf{x}-\mathbf{y})\,|\mathbf{y}_1\cdots\mathbf{y}_N\rangle - \hat{\psi}^{\dagger}(\mathbf{y})\sum_{k=1}^{N}(-1)^{N+k}\delta(\mathbf{x}-\mathbf{y}_k)\,|\mathbf{y}_1\cdots\mathbf{y}_{k-1}\mathbf{y}_{k+1}\cdots\mathbf{y}_N\rangle \tag{2.6}$$

$$= \delta(\mathbf{x}-\mathbf{y})\,|\mathbf{y}_1\cdots\mathbf{y}_N\rangle - \hat{\psi}^{\dagger}(\mathbf{y})\hat{\psi}(\mathbf{x})\,|\mathbf{y}_1\cdots\mathbf{y}_N\rangle\,. \tag{2.7}$$

From this, the anticommutation relations for fermionic field operators follow:

$$\left\{\hat{\psi}(\mathbf{x}),\hat{\psi}^{\dagger}(\mathbf{y})\right\} = \delta(\mathbf{x}-\mathbf{y}), \qquad \left\{\hat{\psi}(\mathbf{x}),\hat{\psi}(\mathbf{y})\right\} = \left\{\hat{\psi}^{\dagger}(\mathbf{x}),\hat{\psi}^{\dagger}(\mathbf{y})\right\} = 0, \tag{2.8}$$

where $\{\cdot,\cdot\}$ denotes the anticommutator. These relations encapsulate the antisymmetric nature of fermionic states.

Consequently, a general one-particle state $|n\rangle$ with quantum number n can be expressed in terms of the position-spin state $|\mathbf{x}\rangle$ via the completeness relation:

$$|n\rangle = \int d\mathbf{x}\;|\mathbf{x}\rangle\,\langle\mathbf{x}|n\rangle = \int d\mathbf{x}\;\varphi_n(\mathbf{x})\,|\mathbf{x}\rangle = \int d\mathbf{x}\;\varphi_n(\mathbf{x})\hat{\psi}^{\dagger}(\mathbf{x})\,|0\rangle\,. \tag{2.9}$$

Thus, we define the electron creation operator $\hat{c}_n^{\dagger}$ associated with the quantum number n as:

$$\hat{c}_n^{\dagger} = \int d\mathbf{x}\;\varphi_n(\mathbf{x})\hat{\psi}^{\dagger}(\mathbf{x}). \tag{2.10}$$

Similarly, the electron annihilation operator $\hat{c}_n$ can be defined by taking the complex conjugate:

$$\hat{c}_n = \int d\mathbf{x}\;\varphi_n^{*}(\mathbf{x})\hat{\psi}(\mathbf{x}). \tag{2.11}$$

where $\varphi_n(\mathbf{x}) = \langle\mathbf{x}|n\rangle$ represents the overlap between the states $|n\rangle$ and $|\mathbf{x}\rangle$, also known as the wavefunction in the position representation.

Similarly, the anticommutation relations for fermionic creation and annihilation operators are given by:

$$\left\{\hat{c}_i,\hat{c}_j^{\dagger}\right\} = \delta_{ij}, \qquad \left\{\hat{c}_i,\hat{c}_j\right\} = \left\{\hat{c}_i^{\dagger},\hat{c}_j^{\dagger}\right\} = 0. \tag{2.12}$$

By applying the orthonormality condition, we can express the field operator in terms of

the electron creation and annihilation operators as follows:

$$\hat{\psi}(\mathbf{x}) = \sum_n \varphi_n(\mathbf{x})\hat{c}_n, \qquad \hat{\psi}^\dagger(\mathbf{x}) = \sum_n \varphi_n^*(\mathbf{x})\hat{c}_n^\dagger. \tag{2.13}$$

2.2 Evolution operator and Heisenberg picture

So far, our discussion has focused on time-independent aspects. To introduce the time evolution of the system with a many-body Hamiltonian $\hat{H}(t)$, we begin with the well-known time-dependent Schrödinger equation:

$$i\frac{d}{dt}|\Psi(t)\rangle = \hat{H}(t)|\Psi(t)\rangle, \tag{2.14}$$

here $|\Psi(t)\rangle$ represents the ket state of the system. Throughout this thesis, we will employ atomic units, setting $\hbar = e = m_e = 4\pi\epsilon_0 = 1$. A special case occurs when $\hat{H}(t) = \hat{H}(t_0)$ is time-independent, where the solution follows from a first-order differential equation:

$$|\Psi(t)\rangle = e^{-i\hat{H}(t_0)(t-t_0)}|\Psi(t_0)\rangle, \tag{2.15}$$

But what is the form of a time-dependent total Hamiltonian? More generally, can we find a unitary operator $\hat{U}(t, t_0)$ that satisfies:

$$|\Psi(t)\rangle = \hat{U}(t, t_0)|\Psi(t_0)\rangle, \tag{2.16}$$

for time-dependent Hamiltonian? A natural approach is to divide the interval between t_0 and t into a sufficiently large number of time steps, so that the Hamiltonian $\hat{H}(t) \sim \hat{H}(t_p)$ within each sub-interval (t_p, t_{p+1}):

$$|\Psi(t)\rangle = \lim_{n\to\infty} \mathcal{T}\left\{e^{-i\Delta t\Sigma_{p=0}^n \hat{H}(t_p)}\right\}|\Psi(t_0)\rangle = \mathcal{T}\left\{e^{-i\int dt'\hat{H}(t')}\right\}|\Psi(t_0)\rangle, \tag{2.17}$$

where the $\mathcal{T}$ is the Wick's time-ordering operator, including a "$-$" sign for Fermion and "$+$" sign for Boson each time when switching the permutation of time. Therefore, the time evolution operator $\hat{U}(t, t_0)$ is:

$$\hat{U}(t, t_0) = \mathcal{T}\left\{e^{-i\int_{t_0}^t dt'\hat{H}(t')}\right\}. \tag{2.18}$$

Substituting Eq. 2.18 into Eq. 2.14 with the boundary condition $\hat{U}(t_0, t_0) = \hat{\mathbb{1}}$, we obtain:

$$\begin{aligned}\hat{U}(t, t_0) &= \hat{\mathbb{1}} - i\int_{t_0}^{t} dt_1 \hat{H}(t_1)\hat{U}(t_1, t_0) \\ &= \hat{\mathbb{1}} - i\int_{t_0}^{t} dt_1 \hat{H}(t_1) + (-i)^2 \int_{t_0}^{t} dt_1 \int_{t_0}^{t_1} dt_2 \hat{H}(t_1)\hat{H}(t_2)\hat{U}(t_2, t_0) \\ &\cdots \\ &= \sum_{k=0}^{\infty} (-i)^k \int_{t_0}^{t} dt_1 \int_{t_0}^{t_1} dt_2 \cdots \int_{t_0}^{t_{k-1}} dt_k \hat{H}(t_1)\hat{H}(t_2)\cdots\hat{H}(t_k).\end{aligned} \tag{2.19}$$

Using the identity for summation over all permutations P of the time ordering:

$$\int_{t_0}^{t} dt_1 \int_{t_0}^{t} dt_2 \cdots \int_{t_0}^{t} dt_k f(t_{P(1)}, \ldots, t_{P(k)}) = \sum_{P} \int_{t_0}^{t} dt_1 \int_{t_0}^{t_1} dt_2 \cdots \int_{t_0}^{t_{k-1}} dt_k f(t_1, \ldots, t_k),$$

we arrive at the commonly used definition of the time evolution operator with the time-ordering operator:

$$\hat{U}(t, t_0) = \sum_{k=0}^{\infty} \frac{(-i)^k}{k!} \int_{t_0}^{t} dt_1 \int_{t_0}^{t} dt_2 \cdots \int_{t_0}^{t} dt_k \mathcal{T}\left\{\hat{H}(t_1)\hat{H}(t_2)\cdots\hat{H}(t_k)\right\}. \tag{2.20}$$

By definition we have the relation:

$$\hat{U}(t_0, t)\hat{U}(t, t_0) = \mathbb{1}, \tag{2.21}$$

with the explicit form of the anti time-evolution operator $\hat{U}(t_0, t)$:

$$\hat{U}(t_0, t) = \bar{\mathcal{T}}\left\{e^{i\int_{t_0}^{t} dt' \hat{H}(t')}\right\}. \tag{2.22}$$

Therefore, the time-dependent quantum average of operator $\hat{O}(t)$ can be written as:

$$\langle\Psi(t)|\,\hat{O}(t)\,|\Psi(t)\rangle = \langle\Psi(t_0)|\,\hat{U}(t_0, t)\hat{O}(t)\hat{U}(t, t_0)\,|\Psi(t_0)\rangle\,. \tag{2.23}$$

This introduces the Heisenberg picture, in which the time-dependent operator $\hat{O}_H(t)$ is defined as:

$$\hat{O}_H(t) = \hat{U}(t_0, t)\hat{O}(t)\hat{U}(t, t_0). \tag{2.24}$$

Note that this definition in the Heisenberg picture also applies to field operators. The density operator, defined as $\hat{n}(\mathbf{x}) = \hat{\psi}^\dagger(\mathbf{x})\hat{\psi}(\mathbf{x})$, can be expressed in the Heisenberg picture

as:

$$\hat{n}_H(\mathbf{x},t) = \hat{U}(t_0,t)\hat{\psi}^\dagger(\mathbf{x})\hat{U}(t,t_0)\hat{U}(t_0,t)\hat{\psi}(\mathbf{x})\hat{U}(t,t_0) = \hat{\psi}^\dagger_H(\mathbf{x},t)\hat{\psi}_H(\mathbf{x},t), \tag{2.25}$$

where the field operators in the Heisenberg picture are defined as:

$$\hat{\psi}^\dagger_H(\mathbf{x},t) = \hat{U}(t_0,t)\hat{\psi}^\dagger(\mathbf{x})\hat{U}(t,t_0), \qquad \hat{\psi}_H(\mathbf{x},t) = \hat{U}(t_0,t)\hat{\psi}(\mathbf{x})\hat{U}(t,t_0). \tag{2.26}$$

It is important to emphasize that, up to this point, no perturbation has been applied. In the Heisenberg picture, the evolution operator $\hat{U}(t,t_0)$ must be constructed using the total Hamiltonian, including the perturbation Hamiltonian when present. Meanwhile, the states, expressed as $|\Psi_H\rangle = |\Psi(t_0)\rangle$, remain time-independent and are determined at the reference time t_0.

2.3 Gell-Mann and Low theorem

Let us consider an N-electron system interacting with a scalar field $V(\mathbf{r})$. In the context of solids, a typical choice for $V(\mathbf{r})$ is the electron-nuclei potential. The total (unperturbed) Hamiltonian in the second quantization, which includes both the one-particle interaction $\hat{H}_0$ and the two-particle interaction $\hat{H}_1$, can be written as:

$$\hat{H} = \hat{H}_0 + \hat{H}_1 = \int d\mathbf{x}\, \hat{\psi}^\dagger(\mathbf{x})h(\mathbf{r})\hat{\psi}(\mathbf{x}) + \frac{1}{2}\int d\mathbf{x}\, d\mathbf{x}'\, \hat{\psi}^\dagger(\mathbf{x})\hat{\psi}^\dagger(\mathbf{x}')v(\mathbf{r},\mathbf{r}')\hat{\psi}(\mathbf{x}')\hat{\psi}(\mathbf{x}). \tag{2.27}$$

The one-particle Hamiltonian $h(\mathbf{r})$ is:

$$h(\mathbf{r}) = -\frac{1}{2}\nabla^2 + V(\mathbf{r}), \tag{2.28}$$

while the two-particle interaction $v(\mathbf{r},\mathbf{r}')$ is the bare Coulomb interaction:

$$v(\mathbf{r},\mathbf{r}') = \frac{1}{|\mathbf{r}-\mathbf{r}'|}. \tag{2.29}$$

To study the equation of motion and its relation to the correlation function, a commonly used approach involves introducing an perturbative interaction Hamiltonian $\hat{H}'(t)$ of an external (scalar) potential $U(\mathbf{x},\mathbf{x}';t)$:

$$\hat{H}'(t) = \int d\mathbf{x}d\mathbf{x}'\psi^\dagger(\mathbf{x})U(\mathbf{x},\mathbf{x}';t)\psi(\mathbf{x}'), \tag{2.30}$$

practically, a physical local scalar potential will take the form:

$$U(\mathbf{x}, \mathbf{x}'; t) = U(\mathbf{x}; t)\delta(\mathbf{x}, \mathbf{x}'). \tag{2.31}$$

In this thesis, we adopt the alternative derivation approach proposed by Hedin [42, 43, 108], which employs functional derivatives of the Green's function (to be defined later). The physical picture originates from Schwinger's variational approach to the equations of motion for the one- and two-particle Green's functions [100]. This approach defines "interaction" differently compared to the conventional diagrammatic framework. For instance, the diagrammatic method [25, 2, 106] does not explicitly include the external potential U; instead, it applies Wick's theorem [121] to the electron-electron interaction term $\hat{H}_1$, as defined here. While both methods are physically equivalent (in perturbation theory), the alternative derivation provides a more direct connection to the equations of motion and conservation laws governing the Green's function, which will be explored in subsequent sections.

The interaction picture is typically defined under the adiabatic assumption, where the interaction is gradually switched on as $t \to -\infty$ and vanishes as $t \to +\infty$. At $t = 0$, the Hamiltonian corresponds to the full Hamiltonian of the interacting system. This is achieved by defining the new time-dependent Hamiltonian as:

$$\hat{H}_\eta(t) = \hat{H}(t) + e^{-\eta|t|}\hat{H}'(t), \tag{2.32}$$

where $\eta \to 0^+$ is a small positive parameter. This allows us to introduce the so called interaction picture, where the field operator and Hamiltonian is defined via the unperturbed Hamiltonian $\hat{H}$:

$$\hat{\psi}_I(\mathbf{x}, t) = e^{i\hat{H}t}\hat{\psi}(\mathbf{x})e^{-i\hat{H}t}; \tag{2.33}$$

$$\hat{H}'_I(t) = e^{i\hat{H}t}\hat{H}'(t)e^{-i\hat{H}t} = \int d\mathbf{x}d\mathbf{x}'\hat{\psi}^\dagger_I(\mathbf{x}, t^+)U(\mathbf{x}, \mathbf{x}'; t)\hat{\psi}_I(\mathbf{x}', t). \tag{2.34}$$

In the interaction picture, the state is time dependent as well:

$$|\Psi_I(t)\rangle = \hat{U}_\eta(t, t_0)\,|\Psi_I(t_0)\rangle \tag{2.35}$$

with the time evolution operator $\hat{U}_\eta(t, t_0)$ in the interaction picture is explicitly given by:

$$\hat{U}_\eta(t, t_0) = \sum_{k=0}^{\infty} \frac{(-i)^k}{k!} \int_{t_0}^{t} dt_1 \int_{t_0}^{t} dt_2 \cdots \int_{t_0}^{t} dt_k e^{-\eta(|t_1|+\cdots+|t_k|)} \mathcal{T}\left\{\hat{H}'_I(t_1)\hat{H}'_I(t_2)\cdots\hat{H}'_I(t_k)\right\}. \tag{2.36}$$

Let $t_0 \to -\infty$ and $\hat{H}_\eta \to \hat{H}$. In the Schrödinger picture, the eigenstate is given by:

$$|\Psi_S^N(t_0)\rangle = e^{-i\hat{H}t_0}\,|\Psi_0^N\rangle\,, \tag{2.37}$$

where $|\Psi_0^N\rangle$ is the eigenstate of the unperturbed time-independent Hamiltonian $\hat{H}$, satisfying:

$$\hat{H}\,|\Psi_0^N\rangle = E\,|\Psi_0^N\rangle\,. \tag{2.38}$$

In the interaction picture with $t_0 \to -\infty$, the eigenstate becomes time-dependent and can be expressed as:

$$|\Psi_I^N(t_0)\rangle = e^{i\hat{H}t_0}\,|\Psi_S^N(t_0)\rangle = |\Psi_0^N\rangle\,. \tag{2.39}$$

From this, we obtain the following important relation:

$$|\Psi_H^N\rangle = |\Psi_I^N(0)\rangle = \hat{U}_\eta(0,-\infty)\,|\Psi_0^N\rangle\,. \tag{2.40}$$

The same procedure can be extended to the limit $t_0 \to +\infty$. Gell-Mann and Low [28, 25] demonstrated that, under the adiabatic assumption, if the following limit exists at all orders in perturbation theory:

$$\lim_{\eta\to 0^+} \frac{\hat{U}_\eta(0,\pm\infty)\,|\Psi_0^N\rangle}{\langle\Psi_0^N|\,\hat{U}_\eta(0,\pm\infty)\,|\Psi_0^N\rangle} = \frac{|\Psi_H^N\rangle}{\langle\Psi_0^N|\Psi_H^N\rangle}, \tag{2.41}$$

then the resulting state becomes an eigenstate of the perturbed Hamiltonian $\hat{H}_\eta$. This result is widely known as the Gell-Mann and Low theorem, valid under the adiabatic assumption [25].

2.4 Interacting Green's function

Let us begin our discussion with the equilibrium, zero-temperature, real-time interacting Green's function, with an external time-dependent perturbation $\hat{H}'(t)$. In many-body physics, a correlation function is defined as the ground-state expectation value of a time-ordered product of operators. A special type of n-particle correlation function involves an equal number of creation and annihilation field operators. It is also referred to as a propagator or Green's function, formally defined [25] in the Heisenberg picture as:

$$G^{(n)}(1,\cdots,n;1',\cdots,n') = (-i)^n\,\langle\Psi_H^N|\,\mathcal{T}\left\{\hat{\psi}_H(1)\cdots\hat{\psi}_H(n)\hat{\psi}_H^\dagger(n')\cdots\hat{\psi}_H^\dagger(1')\right\}|\Psi_H^N\rangle\,. \tag{2.42}$$

Here, $j = (\mathbf{x}_j, t_j)$, with $j = 1, \ldots, n$, represents the joint index of position-spin and time, and $|\Psi_H^N\rangle$ denotes the N-particle Heisenberg ground state with relation defined as Eq. 2.40. The field operator in the Heisenberg picture is defined in Eq. 2.26. It is important to note that our definition of the unperturbed state $|\Psi_0^N\rangle$ corresponds to the ground state of the full unperturbed Hamiltonian $\hat{H} = \hat{H}_0 + \hat{H}_1$, rather than just $\hat{H}_0$, ensuring consistency with the Heisenberg picture.

However, this expression is challenging to use directly in perturbation theory. The objective is to express the field operators in terms of the unperturbed Hamiltonian. To achieve this, we employ the Gell-Mann and Low theorem to transition to the interaction picture. As an example, consider the general two-operator correlator (assuming $t > t'$):

$$\begin{aligned}
&\langle\Psi_H^N|\,\mathcal{T}\left\{\hat{A}_H(t)\hat{B}_H(t')\right\}|\Psi_H^N\rangle \\
&= \langle\Psi_0^N|\,\hat{U}_\eta^{-1}(0,-\infty)\left\{\hat{U}_\eta(0,t)\hat{A}_I(t)\hat{U}_\eta(t,0)\right\}\left\{\hat{U}_\eta(0,t')\hat{B}_I(t')\hat{U}_\eta(t',0)\right\}\hat{U}_\eta(0,-\infty)\,|\Psi_0^N\rangle \\
&= \langle\Psi_0^N|\,\hat{U}_\eta^{-1}(+\infty,-\infty)\mathcal{T}\left\{\hat{A}_I(t)\hat{B}_I(t')\hat{U}_\eta(+\infty,-\infty)\right\}|\Psi_0^N\rangle \\
&= \frac{\langle\Psi_0^N|\,\mathcal{T}\left\{\hat{A}_I(t)\hat{B}_I(t')\hat{U}_\eta(+\infty,-\infty)\right\}|\Psi_0^N\rangle}{\langle\Psi_0^N|\,\hat{U}_\eta(+\infty,-\infty)\,|\Psi_0^N\rangle}.
\end{aligned} \tag{2.43}$$

In the first step we use the result of Eq. 2.40. In the final step, we invoke the adiabatic assumption for a non-degenerate ground state. This assumption ensures that $\hat{U}_\eta(+\infty,-\infty)\,|\Psi_0^N\rangle$ is also a ground state, apart from a phase factor. As a result, $\hat{U}_\eta(+\infty,-\infty)$ only introduces a phase factor to the state. This operator is commonly referred to as the S-matrix:

$$\hat{S} = \hat{U}_\eta(+\infty,-\infty) = \mathcal{T}\left\{e^{-i\int_{-\infty}^{+\infty} dt\,\hat{H}_I'(t)}\right\}, \tag{2.44}$$

where $\mathcal{T}$ denotes the time-ordering operator, and $\hat{H}_I'(t)$ is the perturbative interacting Hamiltonian in the interaction picture. For convenience in notation, we define:

$$\hat{\psi}(1) = \hat{\psi}_I(\mathbf{x}_1, t_1) = e^{i\hat{H}t_1}\hat{\psi}(\mathbf{x}_1)e^{-i\hat{H}t_1}, \tag{2.45}$$

to represent the field operator in the interaction picture. Furthermore, unless otherwise specified, field operators indexed by numbers are assumed to be in the interaction picture. By applying the same operation to multiple field operators, we obtain the Green's function

in the interaction picture:

$$G^{(n)}(1,\cdots,n;1',\cdots,n') = \frac{\langle \Psi_0^N | \mathcal{T}\left\{\hat{S}\hat{\psi}(1)\cdots\hat{\psi}(n)\hat{\psi}^\dagger(n')\cdots\hat{\psi}^\dagger(1')\right\}|\Psi_0^N\rangle}{\langle \Psi_0^N | \mathcal{T}\{\hat{S}\}|\Psi_0^N\rangle}. \tag{2.46}$$

Thus far, we have established the foundational prerequisites necessary to address the equations of motion and subsequent perturbative treatments. Particular attention must be given to the precise definitions of the Green's function, S-matrix, field operators, and the various pictures. Since we are employing the functional derivative approach [42, 43, 108], as discussed earlier, the interaction terms are defined differently compared to the conventional diagrammatic approach presented in standard textbooks [25, 2, 106].

2.5 Equations of motion for operators in the Heisenberg picture

An operator $\hat{O}(t)$ is defined in the Heisenberg picture as:

$$\hat{O}_H(t) = \hat{U}(t_0,t)\hat{O}(t)\hat{U}(t,t_0), \tag{2.47}$$

where $\hat{U}(t,t_0)$ is the time evolution operator governed by the time-dependent Schrödinger equation with the boundary condition:

$$i\frac{d}{dt}\hat{U}(t,t_0) = \hat{H}(t)\hat{U}(t,t_0), \qquad \hat{U}(t_0,t_0) = \mathbb{1}. \tag{2.48}$$

From this, we derive the equations of motion for operators in the Heisenberg picture:

$$i\frac{d}{dt}\hat{O}_H(t) = \left[\hat{O}_H(t),\hat{H}_H(t)\right] + i\frac{\partial}{\partial t}\hat{O}_H(t). \tag{2.49}$$

where the notation for the partial time derivative of the operator in the Heisenberg picture refers to the time derivative of the operator in the Schrödinger picture.

For the unperturbed Hamiltonian $\hat{H}$ defined in Eq. 2.27, the equations of motion for the field operators can be written in the Heisenberg picture. Since there is no explicit time dependence of the field operator (so that the last term on the right-hand side of Eq. 2.49 vanishes), we have [106]:

$$i\frac{d}{dt_1}\hat{\psi}_H(1) = \left[h(1) + \int d3\, v(1,3)\hat{\psi}_H^\dagger(3)\hat{\psi}_H(3)\right]\hat{\psi}_H(1); \tag{2.50}$$

$$i\frac{d}{dt_2}\hat{\psi}_H^\dagger(2) = -\hat{\psi}_H^\dagger(2)\left[h(2) + \int d3\, v(2,3)\hat{\psi}_H^\dagger(3)\hat{\psi}_H(3)\right], \tag{2.51}$$

with the additional definitions $h(1) = h(\mathbf{r}_1)$ and $v(1,2) = v(\mathbf{r}_1, \mathbf{r}_2)\delta(t_1 - t_2)$.

Now, consider a special time-ordered correlation operator:

$$\hat{G}^n(1,\cdots,n;1',\cdots,n') = (-i)^n \mathcal{T}\left\{\hat{\psi}_H(1)\cdots\hat{\psi}_H(n)\hat{\psi}_H^\dagger(n')\cdots\hat{\psi}_H^\dagger(1')\right\}, \tag{2.52}$$

where $\mathcal{T}$ denotes the time-ordering operator. The equation of motion for this correlation operator can be expressed in the Heisenberg picture [106]:

$$\begin{aligned} &i\frac{d}{dt_k}\hat{G}^n(1,\cdots,n;1',\cdots,n') \\ &\quad = (-i)^n \mathcal{T}\left\{\hat{\psi}_H(1)\cdots\left(i\frac{d}{dt_k}\hat{\psi}_H(k)\right)\cdots\hat{\psi}_H(n)\hat{\psi}_H^\dagger(n')\cdots\hat{\psi}_H^\dagger(1')\right\} \\ &\qquad + \sum_{j=1}^{n}(-1)^{k+j}\delta(k,j')\hat{G}^{n-1}(1,\cdots,\overline{k},\cdots,n;1',\cdots,\overline{j'},\cdots,n'). \end{aligned} \tag{2.53}$$

Here, the notation $\overline{k}$ (or $\overline{j'}$) indicates that the corresponding indices are excluded from the correlation operator.

By applying the equation of motion for field operators, as given in Eq. 2.49, we achieve an important relation that connects the equations of motion of n- and $n \pm 1$-particle correlation operators. This relation is commonly referred to as the Martin-Schwinger hierarchy [106]:

$$\begin{aligned} &\left[i\frac{d}{dt_k} - h(k)\right]\hat{G}^n(1,\cdots,n;1',\cdots,n') \\ &= -i\int d\bar{1}\, v(k,\bar{1})\hat{G}^{n+1}(1,\cdots,n,\bar{1}^+;1',\cdots,n',\bar{1}^{++}) \\ &\quad + \sum_{j'=1}^{n}(-1)^{k+j'}\delta(k,j')\hat{G}^{n-1}(1,\cdots,\overline{k},\cdots,n;1',\cdots,\overline{j'},\cdots,n'), \end{aligned} \tag{2.54}$$

$$\begin{aligned}
&\hat{G}^n(1,\cdots,n;1',\cdots,n')\left[-i\frac{d}{dt_{k'}}-h(k')\right]\\
&=-i\int d\bar{1}\,v(k',\bar{1})\hat{G}^{n+1}(1,\cdots,n,\bar{1}^{--};1',\cdots,n',\bar{1}^{-})\\
&\quad+\sum_{j=1}^{n}(-1)^{k'+j}\delta(j,k')\hat{G}^{n-1}(1,\cdots,\bar{j},\cdots,n;1',\cdots,\overline{k}',\cdots,n').
\end{aligned}\tag{2.55}$$

This hierarchy describes the recursive structure of n-particle Green's functions in terms of $n\pm1$-particle Green's functions and is fundamental in many-body theory.

2.6 Martin-Schwinger hierarchy in the interaction picture

We begin by defining the one- and two-particle Green's functions. In the interaction picture, with an external perturbation $\hat{H}'$, these Green's functions are expressed as follows, based on Eq. 2.46:

$$G^{(1)}(1;2)=(-i)\frac{\langle\Psi_0^N|\,\mathcal{T}\left\{\hat{S}\hat{\psi}(1)\hat{\psi}^\dagger(2)\right\}|\Psi_0^N\rangle}{\langle\Psi_0^N|\,\mathcal{T}\{\hat{S}\}|\Psi_0^N\rangle},\tag{2.56}$$

$$G^{(2)}(1,2;1',2')=(-i)^2\frac{\langle\Psi_0^N|\,\mathcal{T}\left\{\hat{S}\hat{\psi}(1)\hat{\psi}(2)\hat{\psi}^\dagger(2')\hat{\psi}^\dagger(1')\right\}|\Psi_0^N\rangle}{\langle\Psi_0^N|\,\mathcal{T}\{\hat{S}\}|\Psi_0^N\rangle},\tag{2.57}$$

where the S-matrix $\hat{S}$ is defined in Eq. 2.44. Since the equations of motion for the field operator (Eqs. 2.50 and 2.51) are invariant under the gauge transformation of an external electromagnetic field [106], their structure remains unchanged in the interaction picture:

$$i\frac{d}{dt_1}\hat{\psi}(1)=\left[h(1)+\int d3\,v(1,3)\hat{\psi}^\dagger(3)\hat{\psi}(3)\right]\hat{\psi}(1);\tag{2.58}$$

$$i\frac{d}{dt_2}\hat{\psi}^\dagger(2)=-\hat{\psi}^\dagger(2)\left[h(2)+\int d3\,v(2,3)\hat{\psi}^\dagger(3)\hat{\psi}(3)\right].\tag{2.59}$$

Using the equation of motion for the time evolution operator $\hat{U}_\eta(t_1,t_2)$ in the interaction picture, we have:

$$\frac{d}{dt_1}\hat{U}_\eta(t_1,t_2)=-i\hat{H}'_I(t_1)\hat{U}_\eta(t_1,t_2);\qquad \hat{U}_\eta(t_1,t_2)\frac{d}{dt_2}=i\hat{U}_\eta(t_1,t_2)\hat{H}'_I(t_2),\tag{2.60}$$

where $\hat{H}'_I$ is the perturbative interaction Hamiltonian $\hat{H}'$ in the interaction picture, as defined in Eq. 2.34. Using this, we can formulate the generalized Martin-Schwinger hierarchy for the one-particle Green's function in the interaction picture [108]:

$$\left[i\frac{d}{dt_1} - h(1)\right] G^{(1)}(1;2) - \int d3U(1,3)G^{(1)}(3;2) + i\int d3v(1,3)G^{(2)}(1,3^+;2,3^{++}) = \delta(1,2); \tag{2.61}$$

$$G^{(1)}(1;2)\left[-i\frac{d}{dt_2} - h(2)\right] - \int d3G^{(1)}(1,3)U(3;2) + i\int d3v(2,3)G^{(2)}(1,3^{--};2,3^{-}) = \delta(1,2). \tag{2.62}$$

with the additional definition $U(1,2) = U(\mathbf{x}_1, \mathbf{x}_2, t_1)\delta(t_1 - t_2)$, note that letting $U \to 0$ recovers the standard definition of the equilibrium Green's function without perturbation [25, 2, 106].

2.7 Schwinger equation with variational potential

Taking the first-order variation of $\delta G^{(1)}(1;2)$ with respect to the external potential $U(4,3) = U(\mathbf{x}_4, \mathbf{x}_3; t_3)\delta(t_4 - t_3)$, we obtain the following identity [108, 12]:

$$\delta G^{(1)}(1;2) = (-i)\frac{\langle \Psi_0^N | \mathcal{T}\left\{\delta\hat{S}\hat{\psi}(1)\hat{\psi}^\dagger(2)\right\} | \Psi_0^N\rangle}{\langle \Psi_0^N | \mathcal{T}\{\hat{S}\} | \Psi_0^N\rangle} - \frac{\langle \Psi_0^N | \mathcal{T}\left\{\delta\hat{S}\right\} | \Psi_0^N\rangle}{\langle \Psi_0^N | \mathcal{T}\{\hat{S}\} | \Psi_0^N\rangle}. \tag{2.63}$$

Observe that the two-field operator term $\hat{\psi}^\dagger\hat{\psi}$ commutes with other two-field operators in the S-matrix [108, 12]. This allows us to apply the variation of the exponential inside the time-ordering operator as:

$$\begin{aligned}\delta\hat{S} = \delta\mathcal{T}\left\{e^{-i\int_{-\infty}^{+\infty} dt\, \hat{H}'_I(t)}\right\} &= (-i)\int_{-\infty}^{+\infty} dt\, \hat{H}'_I(t)\mathcal{T}\left\{e^{-i\int_{-\infty}^{+\infty} dt\, \hat{H}'_I(t)}\right\} \\ &= \mathcal{T}\left\{e^{-i\int_{-\infty}^{+\infty} dt\, \hat{H}'_I(t)}\right\}(-i)\int_{-\infty}^{+\infty} dt\, \delta\hat{H}'_I(t) \\ &= -i\hat{S}\int_{-\infty}^{+\infty} dt_3 \int d\mathbf{x}_4 d\mathbf{x}_3\, \hat{\psi}_I^\dagger(\mathbf{x}_4, t_3^+)U(\mathbf{x}_4, \mathbf{x}_3; t_3)\hat{\psi}_I(\mathbf{x}_3, t_3).\end{aligned} \tag{2.64}$$

Thus, we obtain the important relation commonly referred to as the Schwinger equation [100]:

$$G^{(2)}(1,3;2,4) = G^{(1)}(1;2)G^{(1)}(3;4) - \frac{\delta G^{(1)}(1;2)}{\delta U(4,3)}. \tag{2.65}$$

By substituting the Schwinger equation into the generalized Martin-Schwinger hierarchy, we can rewrite Eqs. 2.61 and 2.62 as follows. To simplify the notation, we omit the corner indices of (1) or (2) in the later sections:

$$\begin{aligned}\left[i\frac{d}{dt_1} - h(1) - U(1^+,1) + i\int d3\, v(1,3)G(3;3^+)\right]G(1;2) \\ -i\int d3\, v(1^+,3)\frac{\delta G(1;2)}{\delta U(3^+,3)} = \delta(1,2);\end{aligned} \tag{2.66}$$

$$\begin{aligned}G(1;2)\left[-i\frac{d}{dt_2} - h(2) - U(2,2^-) + i\int d3\, v(2,3)G(3^-;3)\right] \\ -i\int d3\, v(2^-,3)\frac{\delta G(1;2)}{\delta U(3,3^-)} = \delta(1,2).\end{aligned} \tag{2.67}$$

2.8 Schwinger–Dyson equation

To avoid referencing the variational external potential, a commonly used technique is to rewrite the equation by defining a new quantity that includes the $\delta G/\delta U$ term, referred to as the self-energy. Two alternative expressions can be defined from Eqs. 2.66 and 2.67:

$$\overrightarrow{\Sigma}(1;2) = \Sigma_H(1;2) + \overrightarrow{\Sigma}_{XC}(1;2); \qquad \overleftarrow{\Sigma}(1;2) = \Sigma_H(1;2) + \overleftarrow{\Sigma}_{XC}(1;2). \tag{2.68}$$

Here, $\Sigma_H(1;2)$ represents the Hartree self-energy:

$$\Sigma_H(1;2) = \delta(1,2)\left[-i\int d3 v(1,3)G(3;3^+)\right], \tag{2.69}$$

While $\overrightarrow{\Sigma}_{XC}(1;2)$ and $\overleftarrow{\Sigma}_{XC}(1;2)$ denote the exchange-correlation self-energy, they are defined from two alternative expressions in Eqs. 2.66 and 2.67:

$$\overrightarrow{\Sigma}_{XC}(1;2) = i\int d3\, d4\, v(1^+,3)\frac{\delta G(1;4)}{\delta U(3^+,3)}G^{-1}(4;2); \tag{2.70}$$

$$\overleftarrow{\Sigma}_{XC}(1;2) = i\int d3\, d4\, G^{-1}(1;4)\frac{\delta G(4;2)}{\delta U(3,3^-)}v(3,2^-). \tag{2.71}$$

where the inverse Green's function is defined through the following identity:

$$\int d3\, G^{-1}(1;3)G(3;2) = \int d3\, G(1;3)G^{-1}(3;2) = \delta(1,2). \tag{2.72}$$

Therefore the Eqs. 2.66 and 2.67 have a compact form with our definition of self energy:

$$\left[i\frac{d}{dt_1} - h(1) - U(1^+,1)\right] G(1;2) - \int d3\, \overrightarrow{\Sigma}(1;3)G(3;2) = \delta(1,2); \tag{2.73}$$

$$G(1;2)\left[-i\frac{d}{dt_2} - h(2) - U(2,2^-)\right] - \int d3\, \overrightarrow{\Sigma}(1;3)G(3;2) = \delta(1,2). \tag{2.74}$$

To properly define the inverse Green's function, $\overrightarrow{\Sigma}_{XC}(1;2)$ and $\overleftarrow{\Sigma}_{XC}(1;2)$ must be equal. This equality can be established using the conservation approximations for the Green's function [108, 106]. Accordingly, we adopt the unified notation $\Sigma_{XC} = \overrightarrow{\Sigma}_{XC} = \overleftarrow{\Sigma}_{XC}$ to represent the exchange-correlation self-energy.

Eqs. 2.73 and 2.74 are commonly referred to as the differential forms of the Schwinger–Dyson equations [108, 106], or simply as Dyson's equation in perturbation theory. To establish a clearer connection with Dyson's equation in the diagrammatic framework, we define the non-interacting one-particle Green's function G_0, which satisfies the following equations of motion:

$$\left[i\frac{d}{dt_1} - h(1)\right] G_0(1;2) = \delta(1,2); \tag{2.75}$$

$$G_0(1;2)\left[-i\frac{d}{dt_2} - h(2)\right] = \delta(1,2). \tag{2.76}$$

These expressions correspond to the zeroth-order Green's function, derived under the assumption that the two-particle electron-electron interaction $\hat{H}_1$ and the external perturbation $\hat{H}'$ vanish. Substituting Eqs. 2.75 and 2.76 into the differential forms given by Eqs. 2.73 and 2.74, we obtain:

$$\int d3\left[G_0^{-1}(1;3) - U(1,3) - \Sigma(1;3)\right] G(3;2) = \delta(1,2), \tag{2.77}$$

$$\int d3 G(1;3)\left[G_0^{-1}(3;2) - U(3,2) - \Sigma(3;2)\right] = \delta(1,2). \tag{2.78}$$

Comparing this result with the definition of the inverse Green's function in Eq. 2.72, we find:

$$G^{-1}(1;2) = G_0^{-1}(1;2) - U(1;2) - \Sigma(1;2), \tag{2.79}$$

and the corresponding integral form:

$$G(1;2) = G_0(1;2) + \int d3d4\, G_0(1;3)\,[U(3,4) + \Sigma(3;4)]\,G(4;2), \tag{2.80}$$

which represents the most commonly used form of Dyson's equation [25, 2, 106].

2.9 Vertex function and Hedin's equations

To close the equation of motion, it is necessary to eliminate the dependence on the variational external potential U. For this purpose, we define the total potential V as:

$$V(1) = U(1) - i\int d3\, v(1,3)G(3;3^+), \tag{2.81}$$

where $U(1)$ is a local scalar external potential, satisfying the relation $U(1) = U(1^+,1) = U(1,1^-)$. Using this definition, the exchange-correlation self-energy can be expressed through the chain rule [42, 43, 108, 12]:

$$\Sigma_{XC}(1;2) = -i\int d3\, d4\, d5\, v(1^+,3)G(1;4)\frac{\delta G^{-1}(4;2)}{\delta V(5)}\frac{\delta V(5)}{\delta U(3)}. \tag{2.82}$$

The last term on the right-hand side is closely related to the Schwinger equation 2.65. Noting that $-iG(1;1^+) = \langle\hat{n}(1)\rangle = n(1)$, where $\hat{n}(1) = \hat{\psi}^\dagger(1)\hat{\psi}(1)$ is the density operator in the interaction picture, we obtain:

$$\frac{\delta V(1)}{\delta U(2)} = \delta(1,2) + \int d3\, v(1,3)\frac{\delta n(3)}{\delta U(2)}. \tag{2.83}$$

By applying two delta functions to reduce the two-particle Green's function in the Schwinger equation 2.65 to a "bubble diagram," we derive:

$$\frac{\delta G(1;1^+)}{\delta U(2^+,2)} = i\frac{\delta n(1)}{\delta U(2)} = G(1;1^+)G(2;2^+) - G(1,2;1^+,2^+). \tag{2.84}$$

As we will see in a later section, the quantity $\delta n/\delta U$ corresponds to the density-density response function, as defined by the Kubo formula [25, 2, 106] in the linear response theory. This quantity is commonly known as the (reducible) polarizability χ:

$$\chi(1;2) = \frac{\delta n(1)}{\delta U(2)} = i\left[G(1,2;1^+,2^+) - G(1;1^+)G(2;2^+)\right]. \tag{2.85}$$

We will revisit this quantity in greater detail when discussing the two-particle correlation function and the Bethe-Salpeter equation. The left-hand side of Eq. 2.83 is commonly referred to as the inverse dielectric function, ϵ^{-1}, as defined in linear response theory. Consequently, Eq. 2.83 can be expressed as:

$$\epsilon^{-1}(1;2) = \delta(1,2) + \int d3\, v(1,3)\chi(3;2). \tag{2.86}$$

It is often convenient to express χ from Eq. 2.84 in terms of the total field V:

$$\begin{aligned}\chi(1;2) &= \int d3 \frac{\delta n(1)}{\delta V(3)} \frac{\delta V(3)}{\delta U(2)} \\ &= \int d3 \frac{\delta n(1)}{\delta V(3)} \left[\delta(3,2) + \int d4\, v(3,4)\chi(4;2)\right] \\ &= \chi_0(1;2) + \int d3d4\, \chi_0(1;3)v(3,4)\chi(4;2),\end{aligned} \tag{2.87}$$

where the irreducible polarizability χ_0 is defined as:

$$\chi_0(1;2) = \frac{\delta n(1)}{\delta V(2)}. \tag{2.88}$$

Similarly, the dielectric function ϵ can be expressed in terms of the irreducible polarizability χ_0:

$$\epsilon(1;2) = \delta(1,2) - \int d3\, v(1,3)\chi_0(3;2). \tag{2.89}$$

Finally, we examine the term $-\delta G^{-1}/\delta V$, which is commonly referred to as the vertex function Γ, as introduced in Eq. 2.82:

$$\begin{aligned}\Gamma(1,2;3) = -\frac{\delta G^{-1}(1;2)}{\delta V(3)} &= \delta(1,3)\delta(2,3) + \frac{\delta \Sigma_{XC}(1;2)}{\delta V(3)} \\ &= \delta(1,3)\delta(2,3) + \int d4d5 \frac{\delta \Sigma_{XC}(1;2)}{\delta G(4;5)} \frac{\delta G(4;5)}{\delta V(3)}.\end{aligned} \tag{2.90}$$

The last term on the right-hand side can be expressed in terms of an integral involving Γ:

$$\begin{aligned}\frac{\delta G(4;5)}{\delta V(3)} &= -\int d6d7\, G(4;6)G(7;5)\frac{\delta G^{-1}(6;7)}{\delta V(3)} \\ &= \int d6d7\, G(4;6)G(7;5)\Gamma(6,7;3),\end{aligned} \tag{2.91}$$

where we use the following identity from functional analysis:

$$\frac{\delta f(1;2)}{\delta g(3)} = -\int d4d5\, f(1;4)\frac{\delta f^{-1}(4;5)}{\delta g(3)} f(5;2). \tag{2.92}$$

A special case of Eq. 2.91 defines the irreducible polarizability χ_0 in terms of the vertex function:

$$\chi_0(1;2) = -i\frac{\delta G(1;1^+)}{\delta V(2)} = -i\int d3d4\, G(1;3)G(4;1)\Gamma(3,4;2). \tag{2.93}$$

Substituting this result, we derive the equation for the vertex function:

$$\Gamma(1,2;3) = \delta(1,3)\delta(2,3) + \int d4d5d6d7\, \frac{\delta\Sigma_{XC}(1;2)}{\delta G(4;5)} G(4;6)G(7;5)\Gamma(6,7;3). \tag{2.94}$$

As we will see in later discussions, this is the Bethe-Salpeter equation for the vertex function. To further simplify the self-energy, it is convenient to define a screened Coulomb potential W:

$$\begin{aligned}W(1,2) &= \int d3\, \epsilon^{-1}(1,3)v(3,2) \\ &= v(1,2) + \int d3d4\, v(1,3)\chi_0(3;4)W(4,2) \\ &= v(1,2) + \int d3d4\, v(1,3)\chi(3;4)v(4,2).\end{aligned} \tag{2.95}$$

Thus, Eq. 2.82 can be expressed compactly in terms of the screened Coulomb potential and the vertex function:

$$\begin{aligned}\Sigma_{XC}(1;2) &= i\int d3d4\, W(1^+,3)G(1,4)\Gamma(4,2;3) \\ &= i\int d3d4\, \Gamma(1,4;3)W(4^+,2)G(3,2^-).\end{aligned} \tag{2.96}$$

The equations for χ_0, Γ, W, and Σ_{XC}, along with Dyson's equation for the one-particle Green's function, are collectively known as Hedin's equations [42, 43, 108, 106].

2.10 Two-particle correlation function and Bethe–Salpeter equation

We define the right-hand side of the Schwinger equation 2.65 as the two-particle correlation function L:

$$L(1,3;2,4) = \frac{\delta G(1;2)}{\delta U(4,3)}. \tag{2.97}$$

Thus, the Schwinger equation can be expressed as:

$$L(1,3;2,4) = -G(1,3;2,4) + G(1;2)G(3;4), \tag{2.98}$$

which is the most commonly used definition for the two-particle correlation function L. In some literature, L is also defined with a prefactor of the imaginary unit i, so it reduces to the reducible polarizability when the diagram is closed with $3 \to 1, 4 \to 2$.

Applying the functional analysis identity from Eq. 2.92 to Eq. 2.97, we obtain:

$$\begin{aligned} L(1,2;1',2') = \frac{\delta G(1;1')}{\delta U(2',2)} &= -\int d3d4\, G(1;3)\frac{\delta G^{-1}(3;4)}{\delta U(2',2)}G(4;1') \\ &= \int d3d4\, G(1;3)\left[\delta(3,2')\delta(4,2) + \frac{\delta\Sigma(3;4)}{\delta U(2',2)}\right] G(4;1') \\ &= G(1;2')G(2;1') + \int d3d4d5d6\, G(1;3)G(4;1')\frac{\delta\Sigma(3;4)}{\delta G(6;5)}L(6,2;5,2'), \end{aligned} \tag{2.99}$$

where we introduce the Bethe-Salpeter (BS) Kernel Ξ and the zeroth-order correlation function L_0:

$$\Xi(3,5;4,6) = \frac{\delta\Sigma(3;4)}{\delta G(6;5)}, \qquad L_0(1,2;1',2') = G(1;2')G(2;1'). \tag{2.100}$$

Using these definitions, the Bethe-Salpeter equation (BSE) for the two-particle correlation function L takes the following form:

$$L(1,2;1',2') = L_0(1,2;1',2') + \int d3d4d5d6\, L_0(1,4;1',3)\Xi(3,5;4,6)L(6,2;5,2'). \quad (2.101)$$

This form is analogous to Dyson's equation for the one-particle Green's function, but it applies to the two-particle correlation function.

2.11 Practical Implementation of GW Approximation and Bethe–Salpeter Equation

2.11.1 Dynamical screening and exchange-correlation self-energy

The single-particle Green's function can be formally expressed by inserting a complete set of exact many-body eigenstates, which correspond to systems with $N+1$, and $N-1$ particles. This insertion allows us to decompose the Green's function into contributions from particle addition and removal processes, respectively. Specifically, we write:

$$\begin{aligned} G(\mathbf{x}_1,\mathbf{x}_2;t) = &-i\theta(t)\sum_m f_m(\mathbf{x}_1)f_m^*(\mathbf{x}_2)e^{i(\epsilon_0^N-\epsilon_m^{N+1})t} \\ &+i\theta(-t)\sum_n g_n^*(\mathbf{x}_2)g_n(\mathbf{x}_1)e^{-i(\epsilon_0^N-\epsilon_n^{N-1})t}, \end{aligned} \quad (2.102)$$

where $t = t_1 - t_2$ is the time difference, and $\theta(t)$ is the Heaviside step function, ensuring causality in the time ordering of operators. The terms $f_m(\mathbf{x})$ and $g_n(\mathbf{x})$ are defined as the many-body matrix elements:

$$f_m(\mathbf{x}) = \langle\Psi_0^N|\,\hat{\psi}(\mathbf{x})\,|\Psi_m^{N+1}\rangle\,, \quad g_n(\mathbf{x}) = \langle\Psi_n^{N-1}|\,\hat{\psi}(\mathbf{x})\,|\Psi_0^N\rangle\,, \quad (2.103)$$

where:

- $|\Psi_0^N\rangle$ is the ground state of the N-particle system,
- $|\Psi_m^{N+1}\rangle$ and $|\Psi_n^{N-1}\rangle$ are the excited states of the $(N+1)$- and $(N-1)$-particle systems, respectively,
- ϵ_0^N, ϵ_m^{N+1}, and ϵ_n^{N-1} are the corresponding total energies of these many-body states.

Physically, the first term represents the propagation of an added particle (electron addition), while the second term describes the propagation of a removed particle (electron

removal). By applying the Fourier transform to this time-domain expression, we translate the Green's function into frequency space. This results in the well-known Lehmann representation of the single-particle Green's function:

$$G(\mathbf{x}_1, \mathbf{x}_2; \omega) = \sum_m \frac{f_m(\mathbf{x}_1) f_m^*(\mathbf{x}_2)}{\omega - (\epsilon_m^{N+1} - \epsilon_0^N) + i\eta} + \sum_n \frac{g_n(\mathbf{x}_1) g_n^*(\mathbf{x}_2)}{\omega - (\epsilon_0^N - \epsilon_n^{N-1}) - i\eta}, \tag{2.104}$$

In practical implementations of many-body perturbation theory [25, 106, 108, 12, 70], the non-interacting Green's function G^0 is not constructed from free-particle states, but instead from the Kohn-Sham (KS) eigenstates obtained by solving the Kohn-Sham equations within density functional theory (DFT). The non-interacting Green's function in this basis is expressed as:

$$G^0(\mathbf{x}_1, \mathbf{x}_2; \omega) = \sum_{n\mathbf{k}} \varphi_{n\mathbf{k}}(\mathbf{x}_1) \varphi_{n\mathbf{k}}^*(\mathbf{x}_2) G_{n\mathbf{k}}^0(\omega), \tag{2.105}$$

where $\varphi_{n\mathbf{k}}(\mathbf{x}) = \langle \mathbf{x} | n\mathbf{k} \rangle$ are the Kohn-Sham wavefunctions, and $G_{n\mathbf{k}}^0(\omega)$ is the state-resolved non-interacting Green's function, given by:

$$G_{n\mathbf{k}}^0(\omega) = \frac{1 - f_{n\mathbf{k}}}{\omega - \epsilon_{n\mathbf{k}} + i\eta} + \frac{f_{n\mathbf{k}}}{\omega - \epsilon_{n\mathbf{k}} - i\eta}, \tag{2.106}$$

where $f_{n\mathbf{k}}$ is the occupation number of state $|n\mathbf{k}\rangle$, $\epsilon_{n\mathbf{k}}$ is the Kohn-Sham eigenvalue, and η is an infinitesimally small positive quantity.

The interacting Green's function $G_{n\mathbf{k}}(\omega)$ is obtained via Dyson's equation through the exchange-correlation self-energy $\Sigma_{n\mathbf{k}}^{XC}(\omega)$:

$$G_{n\mathbf{k}}(\omega) = G_{n\mathbf{k}}^0(\omega) + G_{n\mathbf{k}}^0(\omega) \Sigma_{n\mathbf{k}}^{XC}(\omega) G_{n\mathbf{k}}(\omega). \tag{2.107}$$

Since G^0 is defined in the Kohn-Sham basis, it already includes the mean-field exchange-correlation effects from DFT through the local exchange-correlation potential $v_{xc}[\rho_0](\mathbf{x})$. Therefore, when applying the many-body exchange-correlation self-energy Σ^{XC}, it is very important to subtract the DFT exchange-correlation contribution $\Sigma^{XC} \to \Sigma^{XC} - \Sigma_{DFT}^{XC}$ to avoid double counting.

The irreducible (non-interacting) polarizability χ^0, which describes the linear density

response of the electron system to an external perturbation, is defined at the lowest order within the random phase approximation (RPA) as:

$$\chi^0(1,2) = -iG(1;2)G(2;1), \tag{2.108}$$

where G is the single-particle Green's function. In practice, χ^0 is often expressed in the transition basis of the the Kohn-Sham states. In this representation, the frequency-dependent polarizability in real space becomes:

$$\chi^0(\mathbf{x}_1, \mathbf{x}_2; \omega) = \sum_{cv\mathbf{kq}} \varphi_{c\mathbf{k}}(\mathbf{x}_1)\varphi^*_{v\mathbf{k}-\mathbf{q}}(\mathbf{x}_1)\varphi_{v\mathbf{k}-\mathbf{q}}(\mathbf{x}_2)\varphi^*_{c\mathbf{k}}(\mathbf{x}_2)\,\chi^0_{cv\mathbf{kq}}(\omega), \tag{2.109}$$

where c and v label conduction and valence bands, respectively, and $\mathbf{k}$ and $\mathbf{q}$ are crystal wave-vectors. The transition-resolved polarizability is given by:

$$\begin{aligned}\chi^0_{cv\mathbf{kq}}(\omega) &= \frac{1}{2\pi}\int d\omega'\, G^0_{v,\mathbf{k}-\mathbf{q}}(\omega')G^0_{c\mathbf{k}}(\omega+\omega') \\ &= \frac{1}{\omega - (\epsilon_{c\mathbf{k}} - \epsilon_{v,\mathbf{k}-\mathbf{q}}) + i\eta} - \frac{1}{\omega + (\epsilon_{c\mathbf{k}} - \epsilon_{v,\mathbf{k}-\mathbf{q}}) - i\eta},\end{aligned} \tag{2.110}$$

within periodic boundary conditions, e.g. the Born–von Karman (BvK) condition used for crystals, the irreducible polarizability is Fourier-transformed into reciprocal space:

$$\chi^0_{\mathbf{G},\mathbf{G}'}(\mathbf{q},\omega) = \sum_{cv\mathbf{k}} \rho^*_{cv\mathbf{k}}(\mathbf{G})\rho_{cv\mathbf{k}}(\mathbf{G}')\,\chi^0_{cv\mathbf{kq}}(\omega), \tag{2.111}$$

where $\mathbf{G}$ and $\mathbf{G}'$ are reciprocal lattice vectors, and $\rho_{cv\mathbf{k}}(\mathbf{G})$ is the transition matrix element defined by:

$$\rho_{cv\mathbf{kq}}(\mathbf{G}) = \langle c\mathbf{k}|\, e^{i(\mathbf{q}+\mathbf{G})\cdot\mathbf{r}}\,|v\mathbf{k}-\mathbf{q}\rangle = \int d\mathbf{r}\, e^{i(\mathbf{q}+\mathbf{G})\cdot\mathbf{r}}\,\varphi^*_{c\mathbf{k}}(\mathbf{r})\,\varphi_{v,\mathbf{k}-\mathbf{q}}(\mathbf{r}). \tag{2.112}$$

The screened Coulomb potential W, which incorporates the effects of electronic screening is given in reciprocal space by:

$$W_{\mathbf{G},\mathbf{G}'}(\mathbf{q},\omega) = \frac{4\pi\epsilon^{-1}_{\mathbf{G},\mathbf{G}'}(\mathbf{q},\omega)}{|\mathbf{q}+\mathbf{G}||\mathbf{q}+\mathbf{G}'|}, \tag{2.113}$$

where $\epsilon^{-1}_{\mathbf{G},\mathbf{G}'}(\mathbf{q},\omega)$ is the inverse dielectric matrix evaluated within the random phase approximation (RPA), and is defined as:

$$\epsilon^{-1}(\mathbf{q},\omega) = \mathbb{1} + \nu(\mathbf{q})\chi(\mathbf{q},\omega), \tag{2.114}$$

with $\nu(\mathbf{q})$ representing the bare Coulomb interaction and $\chi(\mathbf{q},\omega)$ the reducible polarizability. The matrix elements of $\nu(\mathbf{q})$ in reciprocal space are given by:

$$\nu_{\mathbf{G}}(\mathbf{q}) = \frac{4\pi}{|\mathbf{q}+\mathbf{G}|^2}\delta_{\mathbf{G},\mathbf{G}'}. \tag{2.115}$$

Therefore, the exchange-correlation self-energy $\Sigma^{XC}_{n\mathbf{k}} = \langle n\mathbf{k}|\,\Sigma^{XC}\,|n\mathbf{k}\rangle$, within the G_0W approximation, can be expressed as the sum of exchange (Σ^X) and correlation (Σ^C) terms:

$$\Sigma^{XC} = \Sigma^X + \Sigma^C. \tag{2.116}$$

The exchange part of the self-energy is given by:

$$\Sigma^X_{n\mathbf{k}} = -\sum_{\nu,\mathbf{G}}\int \frac{d^3\mathbf{q}}{(2\pi)^3}\,\frac{4\pi}{|\mathbf{q}+\mathbf{G}|^2}\left|\rho_{n\nu\mathbf{k}\mathbf{q}}(\mathbf{G})\right|^2, \tag{2.117}$$

where the sum over ν runs over the occupied states, and $\rho_{n\nu\mathbf{k}\mathbf{q}}(\mathbf{G})$ is the plane-wave matrix element defined as:

$$\rho_{n\nu\mathbf{k}\mathbf{q}}(\mathbf{G}) = \langle n\mathbf{k}|\,e^{i(\mathbf{q}+\mathbf{G})\cdot\mathbf{r}}\,|\nu\mathbf{k}-\mathbf{q}\rangle\,. \tag{2.118}$$

The correlation part of the self-energy is given by:

$$\Sigma^C_{n\mathbf{k}}(\omega) = i\sum_{m,\mathbf{G},\mathbf{G}'}\int\frac{d^3\mathbf{q}}{(2\pi)^3}\int\frac{d\omega'}{2\pi}\,\frac{4\pi\epsilon^{-1}_{\mathbf{G},\mathbf{G}'}(\mathbf{q},\omega')}{|\mathbf{q}+\mathbf{G}||\mathbf{q}+\mathbf{G}'|}\rho_{nm\mathbf{k}\mathbf{q}}(\mathbf{G})\rho^*_{nm\mathbf{k}\mathbf{q}}(\mathbf{G}')G^0_{m\mathbf{k}-\mathbf{q}}(\omega-\omega'), \tag{2.119}$$

where $\epsilon^{-1}_{\mathbf{G},\mathbf{G}'}(\mathbf{q},\omega')$ is the inverse dielectric matrix computed within the RPA, and $G^0_{m\mathbf{k}-\mathbf{q}}$ is the non-interacting Green's function for state $m\mathbf{k}-\mathbf{q}$.

2.11.2 Exciton and Bethe-Salpeter equation

The Bethe-Salpeter kernel [90] with GW self-energy can be represented from Eq. 2.100 at the lowest order of screening as:

$$\begin{aligned}\Xi(3,5;4,6) = \frac{\delta\Sigma(3;4)}{\delta G(6;5)} &= -i\delta(3;4)\delta(5;6)v(3;6) + i\delta(3;6)\delta(4;5) \\ &\coloneqq \Xi^{x}(3,5;4,6) + \Xi^{d}(3,5;4,6),\end{aligned} \tag{2.120}$$

where Ξ^{x} and Ξ^{d} denote the exchange term from the Hartree self-energy and the direct term from the exchange-correlation self-energy, respectively. From Eq. 2.101, the Bethe-Salpeter equation for the two-particle correlation function reads:

$$L(1,2;1',2') = L_0(1,2;1',2') + \int d3\, d4\, d5\, d6\, L_0(1,4;1',3)\, \Xi(3,5;4,6)\, L(6,2;5,2'), \tag{2.121}$$

where $L_0(1,2;1',2') = G(1;2')G(2;1') = i\chi(1,2;1',2')$ is the two-particle non-interacting correlation function. The Lehmann representation of L_0 in the transition basis is:

$$L_0(1,2;1',2';\omega) = i\sum_{v,c}\left(\frac{\psi_c(\mathbf{x}_1)\psi_v^*(\mathbf{x}_1')\psi_v(\mathbf{x}_2)\psi_c^*(\mathbf{x}_2')}{\omega - (\omega_c - \omega_v) + i\eta} - \frac{\psi_v(\mathbf{x}_1)\psi_c^*(\mathbf{x}_1')\psi_c(\mathbf{x}_2)\psi_v^*(\mathbf{x}_2')}{\omega + (\omega_c - \omega_v) - i\eta}\right). \tag{2.122}$$

Within the quasi-particle approximation, where the collective excitations are represented by excitons (bound electron-hole pairs), the Lehmann representation of the two-particle correlation function L in the excitonic basis takes the form:

$$L(1,2;1',2';\omega) = i\sum_{S}\left(\frac{n_S(\mathbf{x}_1,\mathbf{x}_1')n_S^*(\mathbf{x}_2',\mathbf{x}_2)}{\omega - \omega_S + i\eta} - \frac{n_S(\mathbf{x}_2,\mathbf{x}_2')n_S^*(\mathbf{x}_1',\mathbf{x}_1)}{\omega + \omega_S - i\eta}\right), \tag{2.123}$$

where $n_S(\mathbf{x},\mathbf{x}') = \langle 0|\,\hat{\psi}^\dagger(\mathbf{x}')\hat{\psi}(\mathbf{x})\,|S\rangle$ is the exciton amplitude. This amplitude can be expressed in the transition basis as:

$$n_S(\mathbf{x},\mathbf{x}') = \sum_{v,c}\left(A_{vc}^S\psi_c(\mathbf{x})\psi_v^*(\mathbf{x}') + B_{vc}^S\psi_v(\mathbf{x})\psi_c^*(\mathbf{x}')\right), \tag{2.124}$$

where A_{vc}^S and B_{vc}^S are the resonant and anti-resonant components of the exciton amplitude, respectively.

From Eqs. 2.122, 2.123, and 2.124, the Bethe-Salpeter equation (BSE) eigenvalue problem becomes:

$$(\omega_c - \omega_v)A^S_{vc} + \sum_{v'c'} K^{AA}_{vc,v'c'}(\omega_S)A^S_{v'c'} + \sum_{v'c'} K^{AB}_{vc,v'c'}(\omega_S)B^S_{v'c'} = \omega_S A^S_{vc}, \tag{2.125}$$

$$(\omega_c - \omega_v)B^S_{vc} + \sum_{v'c'} K^{BB}_{vc,v'c'}(\omega_S)B^S_{v'c'} + \sum_{v'c'} K^{BA}_{vc,v'c'}(\omega_S)A^S_{v'c'} = -\omega_S B^S_{vc}. \tag{2.126}$$

The interaction kernels are given by:

$$K^{AA}_{vc,v'c'}(\omega_S) = i\int d3456\, \psi_v(\mathbf{x}_4)\psi^*_c(\mathbf{x}_3)\Xi(3,5;4,6;\omega_S)\psi_{v'}(\mathbf{x}_5)\psi^*_{c'}(\mathbf{x}_6), \tag{2.127}$$

$$K^{AB}_{vc,v'c'}(\omega_S) = i\int d3456\, \psi_v(\mathbf{x}_4)\psi^*_c(\mathbf{x}_3)\Xi(3,5;4,6;\omega_S)\psi_{v'}(\mathbf{x}_6)\psi^*_{c'}(\mathbf{x}_5), \tag{2.128}$$

with similar expressions for K^{BB} and K^{BA} due to the symmetry of the BSE kernel structure.

Within the Tamm-Dancoff approximation (TDA) [7, 90, 25], the coupling between resonant and anti-resonant terms is neglected by setting $K^{AB} = K^{BA} = 0$. This approximation is valid when the band gap is large compared to the exciton binding energy. Under TDA, the eigenvalue problem for the resonant term simplifies to:

$$(\omega_c - \omega_v)A^S_{vc} + \sum_{v'c'} K^{AA}_{vc,v'c'}(\omega_S)A^S_{v'c'} = \omega_S A^S_{vc}, \tag{2.129}$$

where the eigenvalues ω_S represent the resonant exciton energies. The Bethe-Salpeter kernel K^{AA} in the spinor transition space can be expressed as [90]:

$$K^{AA} = \begin{pmatrix} K^d + K^x & & & K^x \\ & K^d & & \\ & & K^d & \\ K^x & & & K^d + K^x \end{pmatrix}, \tag{2.130}$$

where each matrix element corresponds to the spin configurations of the electron-hole (transition) pairs in the following order:

$$v\uparrow c\uparrow, \quad v\uparrow c\downarrow, \quad v\downarrow c\uparrow, \quad v\downarrow c\downarrow.$$

It is important to note that for the hole spin, the actual spin counted is the opposite of

the excited electron's spin. Therefore, the spin triplet (symmetric) states in the transition basis are given by:

$$v\uparrow c\downarrow, \quad v\downarrow c\uparrow, \quad \frac{1}{\sqrt{2}}(v\uparrow c\uparrow + v\downarrow c\downarrow),$$

with the corresponding effective kernel $K = K^d$.

In contrast, the spin singlet (antisymmetric) state is represented as:

$$\frac{1}{\sqrt{2}}(v\uparrow c\uparrow - v\downarrow c\downarrow),$$

for which the effective kernel becomes $K = K^d + 2K^x$. The explicit expression for each term in the kernel can be found in Ref. [99, 59, 12, 70]. Therefore, the effective two-particle Hamiltonian in the transition basis, as given in Eq. 2.129, can be expressed as [4]:

$$\hat{H}^{2p}_{vc,v'c'} = (\omega_c - \omega_v)\,\delta_{cc'}\delta_{vv'} + K_{vc,v'c'}, \tag{2.131}$$

where ω_c and ω_v are the quasiparticle energies of the conduction and valence states, respectively, and K denotes the interaction kernel. Given Eq. 2.131, the resonant part of the non-interacting two-particle correlation function L^0 [from Eq. 2.122] and the full two-particle correlation function L [from Eq. 2.123] can be written in the transition basis as follows:

$$L^0_{vc,v'c'}(\omega) = \frac{1}{\omega - (\omega_c - \omega_v) + i\eta}\,\delta_{vv'}\delta_{cc'}, \tag{2.132}$$

$$L_{vc,v'c'}(\omega) = \sum_S \frac{A^S_{vc}A^{S*}_{v'c'}}{\omega - \omega_S + i\eta}, \tag{2.133}$$

where A^S_{vc} denotes the exciton amplitude associated with state S, and ω_S is the exciton energy. It is also important to note that the two-particle correlation function L becomes diagonal in the excitonic eigenbasis:

$$L_{SS'}(\omega) = \frac{1}{\omega - \omega_S + i\eta}\,\delta_{SS'}. \tag{2.134}$$

2.12 Lattice Vibrations and Electron–Phonon Interaction

We follow the derivations outlined in the review by Giustino [32] (Rev. Mod. Phys. **89**, 015003 (2017)) and the foundational work by Maradudin and Vosko [58] (Rev. Mod. Phys. **40**, 1 (1968)).

2.12.1 Dynamical Matrix and Normal Mode Basis

First, we consider a system composed of M ions per unit cell. The position of ion κ in the primitive unit cell is denoted by $\boldsymbol{u}_\kappa$, and its displacement along the Cartesian direction $\alpha = 1, 2, 3$ is given by $u_{\kappa\alpha}$. Periodic boundary conditions are imposed over a supercell consisting of N_p unit cells, indexed by lattice vectors $\mathbf{R}_p$, where $p = 1, \ldots, N_p$. The full position of the ion κ in the unit cell p is then given by $\boldsymbol{u}_{\kappa p} = \mathbf{R}_p + \boldsymbol{u}_\kappa$. We define a uniform grid of $\mathbf{q}$-points in reciprocal space with N_p total points per Brillouin zone, and denote reciprocal lattice vectors by $\mathbf{G}$.

Under the harmonic approximation, the potential energy Φ is expanded in terms of small displacements $\Delta u_{\kappa\alpha p}$ from equilibrium positions $\boldsymbol{u}^0_{\kappa p}$ as:

$$\Phi = \Phi_0 + \frac{1}{2} \sum_{\substack{\kappa\alpha p \\ \kappa'\alpha' p'}} \frac{\partial^2 \Phi}{\partial u_{\kappa\alpha p} \partial u_{\kappa'\alpha' p'}} \Delta u_{\kappa\alpha p} \Delta u_{\kappa'\alpha' p'}. \tag{2.135}$$

The second derivatives of the total energy with respect to ionic displacements define the interatomic force constants:

$$C_{\kappa\alpha p, \kappa'\alpha' p'} = \frac{\partial^2 \Phi}{\partial u_{\kappa\alpha p} \partial u_{\kappa'\alpha' p'}}. \tag{2.136}$$

The resulting equations of motion for the ionic displacements are given by:

$$M_\kappa \ddot{u}_{\kappa\alpha p} = \frac{\partial \Phi}{\partial u_{\kappa\alpha p}} = -\sum_{\kappa'\alpha' p'} C_{\kappa\alpha p, \kappa'\alpha' p'} u_{\kappa'\alpha' p'}, \tag{2.137}$$

where M_κ is the mass of ion κ.

We assume a trial solution of the form:

$$u_{\kappa\alpha p}(t) = u_{\kappa\alpha} M_\kappa^{-1/2} e^{i\mathbf{q}\cdot\mathbf{R}_p - i\omega t}, \tag{2.138}$$

and substitute this into Eq. (2.137) to obtain:

$$\omega^2 u_{\kappa\alpha} = \sum_{\kappa'\alpha'} D_{\kappa\alpha, \kappa'\alpha'}(\mathbf{q}) u_{\kappa'\alpha'}, \tag{2.139}$$

where the dynamical matrix is defined as:

$$D_{\kappa\alpha, \kappa'\alpha'}(\mathbf{q}) = (M_\kappa M_{\kappa'})^{-1/2} \sum_{p'} C_{\kappa\alpha p, \kappa'\alpha' p'} \exp\left[-i\mathbf{q} \cdot (\mathbf{R}_p - \mathbf{R}_{p'})\right]. \tag{2.140}$$

The dynamical matrix $D(\mathbf{q})$ is Hermitian and thus has real eigenvalues. Its eigenvalue problem reads:

$$\sum_{\kappa'\alpha'} D_{\kappa\alpha,\kappa'\alpha'}(\mathbf{q})\, e_{\kappa'\alpha',\nu}(\mathbf{q}) = \omega_{\mathbf{q}\nu}^2\, e_{\kappa\alpha,\nu}(\mathbf{q}), \tag{2.141}$$

where $\omega_{\mathbf{q}\nu}$ is the frequency of phonon mode ν at wavevector $\mathbf{q}$, and $e_{\kappa\alpha,\nu}(\mathbf{q})$ is the corresponding polarization vector (normal mode).

The eigenvectors are normalized and orthogonal for each $\mathbf{q}$:

$$\sum_{\nu} e^*_{\kappa'\alpha',\nu}(\mathbf{q}) e_{\kappa\alpha,\nu}(\mathbf{q}) = \delta_{\kappa\kappa'}\delta_{\alpha\alpha'}, \tag{2.142}$$

$$\sum_{\kappa\alpha} e^*_{\kappa\alpha,\nu}(\mathbf{q}) e_{\kappa\alpha,\nu'}(\mathbf{q}) = \delta_{\nu\nu'}. \tag{2.143}$$

Here, the mode index ν runs from 1 to $3M$. Each mode ν corresponds to a collective vibrational motion of the lattice, and its associated vector $e_{\kappa\alpha,\nu}(\mathbf{q})$ is referred to as the polarization or normal mode of vibration.

From Eq. (2.140), one can also show the following symmetry relations:

$$\omega^2_{-\mathbf{q}\nu} = \omega^2_{\mathbf{q}\nu}, \qquad e_{\kappa\alpha,\nu}(-\mathbf{q}) = e^*_{\kappa\alpha,\nu}(\mathbf{q}), \tag{2.144}$$

indicating that the phonon frequencies are even functions of $\mathbf{q}$, and the eigenmodes at $-\mathbf{q}$ are complex conjugates of those at $\mathbf{q}$.

2.12.2 Second Quantization of the Phonon Hamiltonian

Starting from Eqs. (2.135) and (2.136), the Hamiltonian describing nuclear motion in the Cartesian basis is given by:

$$\hat{H}_p = \frac{1}{2} \sum_{\substack{\kappa\alpha p \\ \kappa'\alpha' p'}} C_{\kappa\alpha p,\kappa'\alpha' p'} \Delta u_{\kappa\alpha p} \Delta u_{\kappa'\alpha' p'} - \sum_{\kappa\alpha p} \frac{\hbar^2}{2M_\kappa} \frac{\partial^2}{\partial u^2_{\kappa\alpha p}}, \tag{2.145}$$

To evaluate the Hamiltonian, we require an explicit expression for the displacements $\Delta u_{\kappa\alpha p}$. The eigenvectors $e_{\kappa\alpha,\nu}(\mathbf{q})$ from the dynamical matrix do not encode amplitude information. Using Eq. (2.138) and normalization with N_p $\mathbf{q}$-points from Born–von Kármán boundary conditions, the displacements can be written as (here I choose a different definition):

$$\Delta u_{\kappa\alpha p} = \frac{1}{\sqrt{N_p}} \sum_{\mathbf{q}\nu} e^{i\mathbf{q}\cdot\mathbf{R}_p}\, e_{\kappa\alpha,\nu}(\mathbf{q})\, z_{\mathbf{q}\nu}, \tag{2.146}$$

where $z_{\mathbf{q}\nu}$ is referred to as the complex normal coordinate.

Inverting Eq. (2.146) gives:

$$z_{\mathbf{q}\nu} = \frac{1}{\sqrt{N_p}} \sum_{\kappa\alpha p} e^{-i\mathbf{q}\cdot\mathbf{R}_p} e^*_{\kappa\alpha,\nu}(\mathbf{q})\, \Delta u_{\kappa\alpha p}. \tag{2.147}$$

The number of degrees of freedom is $3MN_p$, while $z_{\mathbf{q}\nu}$ encodes $2 \times 3MN_p$ real variables, introducing redundancy. Applying Eqs. (2.144) and (2.147) leads to:

$$z_{-\mathbf{q}\nu} = z^*_{\mathbf{q}\nu}. \tag{2.148}$$

To identify $3MN_p$ independent normal coordinates, we partition the $\mathbf{q}$-grid into three sets. Set $\mathcal{A}$ contains vectors invariant under inversion. Sets $\mathcal{B}$ and $\mathcal{C}$ are paired such that $-\mathbf{q}$ in $\mathcal{C}$ corresponds to $\mathbf{q}$ in $\mathcal{B}$. Let $z_{\mathbf{q}\nu} = x_{\mathbf{q}\nu} + iy_{\mathbf{q}\nu}$. Then Eq. (2.146) becomes:

$$\begin{aligned} \Delta u_{\kappa\alpha p} &= \frac{1}{\sqrt{N_p}} \left[\sum_{\mathbf{q}\in\mathcal{A},\nu} e_{\kappa\alpha,\nu}(\mathbf{q}) x_{\mathbf{q}\nu} \right. \\ &+ \left. 2\,\mathrm{Re} \sum_{\mathbf{q}\in\mathcal{B},\nu} e^{i\mathbf{q}\cdot\mathbf{R}_p} e_{\kappa\alpha,\nu}(\mathbf{q})(x_{\mathbf{q}\nu} + iy_{\mathbf{q}\nu}) \right]. \end{aligned} \tag{2.149}$$

This yields exactly $3MN_p$ real degrees of freedom.

We now express the Hamiltonian in terms of $x_{\mathbf{q}\nu}$ and $y_{\mathbf{q}\nu}$:

$$\hat{H}_p = \frac{1}{2} \sum_{\mathbf{q}\nu} \left(-\frac{\hbar^2}{M_\kappa} \frac{\partial^2}{\partial u^2_{\mathbf{q}\nu}} + M_\kappa \omega^2_{\mathbf{q}\nu} (\Delta u_{\mathbf{q}\nu})^2 \right). \tag{2.150}$$

Introducing scaled variables $\tilde{x}_{\mathbf{q}\nu}$ and $\tilde{y}_{\mathbf{q}\nu}$:

$$\tilde{x}_{\mathbf{q}\nu} = x_{\mathbf{q}\nu}/(2l_{\mathbf{q}\nu}) \quad \text{for } \mathbf{q} \in \mathcal{A}, \tag{2.151}$$

$$\tilde{x}_{\mathbf{q}\nu} = x_{\mathbf{q}\nu}/l_{\mathbf{q}\nu}, \quad \tilde{y}_{\mathbf{q}\nu} = y_{\mathbf{q}\nu}/l_{\mathbf{q}\nu} \quad \text{for } \mathbf{q} \in \mathcal{B}, \tag{2.152}$$

where $l_{\mathbf{q}\nu} = \left(\frac{\hbar}{2M_\kappa \omega_{\mathbf{q}\nu}}\right)^{1/2}$ is the zero-point amplitude.

The Hamiltonian becomes:

$$\hat{H}_p = \frac{1}{2} \sum_{\mathbf{q}\in\mathcal{B},\nu} \hbar\omega_{\mathbf{q}\nu} \left(-\frac{\partial^2}{\partial \tilde{x}^2_{\mathbf{q}\nu}} - \frac{\partial^2}{\partial \tilde{y}^2_{\mathbf{q}\nu}} + \tilde{x}^2_{\mathbf{q}\nu} + \tilde{y}^2_{\mathbf{q}\nu} \right)$$

$$+ \quad \frac{1}{2} \sum_{\mathbf{q}\in\mathcal{A},\nu} \hbar\omega_{\mathbf{q}\nu} \left(-\frac{\partial^2}{\partial \tilde{x}^2_{\mathbf{q}\nu}} + \tilde{x}^2_{\mathbf{q}\nu} \right). \tag{2.153}$$

We define the ladder operators:

$$\hat{a}_{\mathbf{q}\nu,x} = \frac{1}{\sqrt{2}} \left(\tilde{x}_{\mathbf{q}\nu} + \frac{\partial}{\partial \tilde{x}_{\mathbf{q}\nu}} \right), \tag{2.154}$$

and analogously for $\hat{a}_{\mathbf{q}\nu,y}$. Eq. (2.153) becomes:

$$\begin{aligned} \hat{H}_p &= \sum_{\mathbf{q}\in\mathcal{B},\nu} \hbar\omega_{\mathbf{q}\nu} \left(\hat{a}^\dagger_{\mathbf{q}\nu,x} \hat{a}_{\mathbf{q}\nu,x} + \hat{a}^\dagger_{\mathbf{q}\nu,y} \hat{a}_{\mathbf{q}\nu,y} + 1 \right) \\ &+ \sum_{\mathbf{q}\in\mathcal{A},\nu} \hbar\omega_{\mathbf{q}\nu} \left(\hat{a}^\dagger_{\mathbf{q}\nu,x} \hat{a}_{\mathbf{q}\nu,x} + \frac{1}{2} \right). \end{aligned} \tag{2.155}$$

To diagonalize this Hamiltonian more naturally, we define complex ladder operators:

$$\hat{a}^+_{\mathbf{q}\nu} = \frac{1}{\sqrt{2}} (\hat{a}_{\mathbf{q}\nu,x} + i\hat{a}_{\mathbf{q}\nu,y}), \tag{2.156}$$

$$\hat{a}^-_{\mathbf{q}\nu} = \frac{1}{\sqrt{2}} (\hat{a}_{\mathbf{q}\nu,x} - i\hat{a}_{\mathbf{q}\nu,y}), \tag{2.157}$$

which relate $\mathbf{q}$ and $-\mathbf{q}$ as $\hat{a}^-_{\mathbf{q}\nu} = \hat{a}^+_{-\mathbf{q}\nu}$.

The ladder operators are then defined as:

$$\hat{a}_{\mathbf{q}\nu} = \hat{a}_{\mathbf{q}\nu,x} \qquad \text{for } \mathbf{q} \in \mathcal{A}, \tag{2.158}$$

$$\hat{a}_{\mathbf{q}\nu} = \frac{1}{\sqrt{2}} (\hat{a}_{\mathbf{q}\nu,x} + i\hat{a}_{\mathbf{q}\nu,y}) \quad \text{for } \mathbf{q} \in \mathcal{B}, \mathcal{C}. \tag{2.159}$$

From this, we obtain the fundamental identity:

$$z_{\mathbf{q}\nu} = \left(\frac{\hbar}{2M_\kappa \omega_{\mathbf{q}\nu}} \right)^{1/2} \left(\hat{a}_{\mathbf{q}\nu} + \hat{a}^\dagger_{-\mathbf{q}\nu} \right), \tag{2.160}$$

and the phonon Hamiltonian in its final form:

$$\hat{H}_p = \sum_{\mathbf{q}\nu} \hbar\omega_{\mathbf{q}\nu} \left(\hat{a}^\dagger_{\mathbf{q}\nu} \hat{a}_{\mathbf{q}\nu} + \frac{1}{2} \right). \tag{2.161}$$

2.12.3 Second Quantization of the Electron–Phonon Hamiltonian

Within the Kohn–Sham formalism of density functional theory (DFT), the electron–phonon interaction is obtained by expanding the Kohn–Sham potential with respect to the displacements of nuclei $\Delta \boldsymbol{u}_{\kappa p}$ from their equilibrium positions $\boldsymbol{u}^0_{\kappa p}$. To first order in the displacements (the Fan–Migdal term), the expansion is given by:

$$\begin{aligned} V^{KS}(\{\boldsymbol{u}_{\kappa p}\}) &= V^{KS}(\{\boldsymbol{u}^0_{\kappa p}\}) + \sum_{\kappa\alpha p} \frac{\partial V^{KS}}{\partial u_{\kappa\alpha p}} \Delta u_{\kappa\alpha p} \\ &= V^{KS}(\{\boldsymbol{u}^0_{\kappa p}\}) \\ &+ N_p^{-1/2} \sum_{\mathbf{q}\nu} \sum_{\kappa\alpha p} \left(\frac{\hbar}{2M_\kappa \omega_{\mathbf{q}\nu}} \right)^{1/2} e_{\kappa\alpha,\nu}(\mathbf{q})\, e^{i\mathbf{q}\cdot\mathbf{R}_p}\, \frac{\partial V^{KS}}{\partial u_{\kappa\alpha}}\bigg|_{\mathbf{r}-\mathbf{R}_p} (\hat{a}_{\mathbf{q}\nu} + \hat{a}^\dagger_{-\mathbf{q}\nu}). \end{aligned} \tag{2.162}$$

This can be rewritten more compactly in the phonon mode basis:

$$V^{KS} = V^{KS}(\{\boldsymbol{u}^0_{\kappa p}\}) + N_p^{-1/2} \sum_{\mathbf{q}\nu} \Delta_{\mathbf{q}\nu} V^{KS} (\hat{a}_{\mathbf{q}\nu} + \hat{a}^\dagger_{-\mathbf{q}\nu}), \tag{2.163}$$

where we have defined:

$$\Delta_{\mathbf{q}\nu} V^{KS} = e^{i\mathbf{q}\cdot\mathbf{r}} \Delta_{\mathbf{q}\nu} v^{KS}, \tag{2.164}$$

$$\Delta_{\mathbf{q}\nu} v^{KS} = \left(\frac{\hbar}{2M_\kappa \omega_{\mathbf{q}\nu}} \right)^{1/2} \sum_{\kappa\alpha} e_{\kappa\alpha,\nu}(\mathbf{q})\, \partial_{\kappa\alpha,\mathbf{q}} v^{KS}, \tag{2.165}$$

$$\partial_{\kappa\alpha,\mathbf{q}} v^{KS} = \sum_p e^{-i\mathbf{q}\cdot(\mathbf{r}-\mathbf{R}_p)}\, \frac{\partial V^{KS}}{\partial u_{\kappa\alpha}}\bigg|_{\mathbf{r}-\mathbf{R}_p}. \tag{2.166}$$

Here, both $\partial_{\kappa\alpha,\mathbf{q}} v^{KS}$ and $\Delta_{\mathbf{q}\nu} v^{KS}$ are lattice-periodic functions.

The second-quantized electron–phonon interaction Hamiltonian is given by:

$$\hat{H}_{ep} = \sum_{n\mathbf{k},n'\mathbf{k}'} \langle \psi_{n\mathbf{k}} | V^{KS}(\{\boldsymbol{u}_{\kappa p}\}) - V^{KS}(\{\boldsymbol{u}^0_{\kappa p}\}) | \psi_{n'\mathbf{k}'} \rangle\, \hat{c}^\dagger_{n\mathbf{k}} \hat{c}_{n'\mathbf{k}'}, \tag{2.167}$$

where the integral is taken over the supercell volume. The Kohn–Sham wavefunctions are expressed in Bloch form:

$$\psi_{n\mathbf{k}}(\mathbf{r}) = N_p^{-1/2} u_{n\mathbf{k}}(\mathbf{r})\, e^{i\mathbf{k}\cdot\mathbf{r}}, \tag{2.168}$$

with $u_{n\mathbf{k}}(\mathbf{r})$ being lattice-periodic.

After substituting Eqs. (2.163)–(2.168) into the interaction Hamiltonian, and canceling

the phase factors, we obtain:

$$\hat{H}_{ep} = N_p^{-1/2} \sum_{\mathbf{k},\mathbf{q}} \sum_{mn\nu} g_{mn\nu}(\mathbf{k},\mathbf{q})\, \hat{c}^{\dagger}_{m,\mathbf{k}+\mathbf{q}} \hat{c}_{n\mathbf{k}} (\hat{a}_{\mathbf{q}\nu} + \hat{a}^{\dagger}_{-\mathbf{q}\nu}), \tag{2.169}$$

where the electron–phonon matrix element in mode representation is defined as:

$$\begin{aligned} g_{mn\nu}(\mathbf{k},\mathbf{q}) &= \langle u_{m,\mathbf{k}+\mathbf{q}} | \Delta_{\mathbf{q}\nu} v^{KS} | u_{n\mathbf{k}} \rangle & (2.170)\\ &= \left(\frac{\hbar}{2M_\kappa \omega_{\mathbf{q}\nu}} \right)^{1/2} \sum_{\kappa\alpha} e_{\kappa\alpha,\nu}(\mathbf{q})\, \langle u_{m,\mathbf{k}+\mathbf{q}} | \partial_{\kappa\alpha,\mathbf{q}} v^{KS} | u_{n\mathbf{k}} \rangle & (2.171)\\ &= \sum_{\kappa\alpha} \left(\frac{\hbar}{2M_\kappa \omega_{\mathbf{q}\nu}} \right)^{1/2} e_{\kappa\alpha,\nu}(\mathbf{q})\, g^{\kappa\alpha}_{mn\nu}(\mathbf{k},\mathbf{q}), & (2.172) \end{aligned}$$

with $g^{\kappa\alpha}_{mn\nu}(\mathbf{k},\mathbf{q})$ denoting the matrix elements in Cartesian representation.

Chapter 3

Phonon-Assisted Radiative Lifetimes and Exciton Dynamics

3.1 Introduction

Exciton-phonon interactions play a fundamental role in governing the optical and transport properties of semiconductors. In particular, they are essential for describing phonon-assisted radiative processes and exciton dynamics in materials with indirect band gaps, where phonons are required to satisfy momentum conservation during photon emission. These phonon-mediated optical transitions are especially relevant in layered van der Waals (vdW) materials and other quantum systems, where the interplay between electronic many-body effects and lattice vibrations gives rise to rich and unconventional physical behavior [116, 94, 11].

Over the past decades, substantial progress has been made in the theoretical and computational understanding of excitons, which are quasiparticles formed by bound electron-hole pairs. This progress has been enabled by first-principles many-body perturbation theory based on the Bethe-Salpeter equation (BSE) [99, 35, 23, 77]. The BSE, typically built on top of quasiparticle corrections from the GW approximation, has successfully predicted exciton binding energies, finite-momentum dispersion [82], exciton-phonon scattering rates [4, 19], and optical spectra in both bulk and low-dimensional systems [83, 99]. However, most existing BSE applications focus on first-order or direct optical transitions [126, 72, 18] and do not capture phonon-assisted recombination processes, which require a second-order treatment involving both exciton-photon and exciton-phonon couplings.

Phonon-assisted luminescence, such as the indirect photoluminescence (PL) observed in hexagonal boron nitride (hBN) [116, 94], monolayer WSe_2 [11], and silicon [57], cannot

be described using first-order optical processes alone. Instead, a second-order process involving both exciton and phonon interactions must be considered. Despite their significance, a fully *ab initio* many-body framework for computing phonon-assisted radiative lifetimes is still lacking. Earlier efforts have formulated such transitions at the single-particle level [64, 73, 110] or have treated exciton-photon and exciton-phonon interactions separately [11, 19, 54], potentially missing the coupling effects between different scattering pathways [17].

In this work, we present a rigorous many-body formalism to compute phonon-assisted radiative lifetimes and simulate time-resolved exciton dynamics from first principles. Our approach is based on constructing an effective exciton-photon-phonon Hamiltonian in second quantization, combining excitonic states from the finite-momentum BSE [99] with exciton-phonon coupling derived from first-principles electron-phonon matrix elements [32, 4, 71, 19]. Radiative rates are evaluated using time-dependent second-order perturbation theory [98], with both phonon emission and absorption channels treated explicitly.

To capture out-of-equilibrium exciton dynamics in open quantum systems, we derive a quantum master equation in the Lindblad form [92, 91, 128, 131], which governs the evolution of the exciton density matrix under phonon scattering. In the semiclassical limit, this formulation reduces to the Boltzmann transport equation (BTE) [93, 49], enabling real-time simulation of exciton relaxation and thermalization. This framework also provides a foundation for future studies of exciton coherence, dephasing, and spin dynamics in realistic material systems.

This work was published as a preprint in Guo *et al.*, *arXiv* arXiv:2504.18071 (2025) [37].

3.2 Effective Exciton-Photon-Phonon Hamiltonian

We first derive the effective exciton-photon-phonon Hamiltonian, as presented in our work [37], starting from the one-particle light-matter interaction (electron-photon) Hamiltonian and the electron-phonon Hamiltonian. In this framework, the exciton, defined as the eigenstate of the Bethe-Salpeter equation (BSE) Hamiltonian, is treated as a quasiparticle in the electron-hole space [68]. The exciton creation operator can be expressed as

$$\hat{c}^{\dagger}_{S(\mathbf{Q})} = \sum_{vc\mathbf{k}} A^{S(\mathbf{Q})}_{vc\mathbf{k}} \hat{d}^{\dagger}_{c\mathbf{k}+\mathbf{Q}} \hat{d}_{v\mathbf{k}}, \tag{3.1}$$

where $\hat{c}^{\dagger}_{S(\mathbf{Q})}$ creates an exciton in state S with momentum $\mathbf{Q}$, $\hat{d}^{\dagger}_{c\mathbf{k}+\mathbf{Q}}$ and $\hat{d}_{v\mathbf{k}}$ are electron creation and annihilation operators, and $A^{S(\mathbf{Q})}_{vc\mathbf{k}}$ denotes the exciton amplitude. This formalism

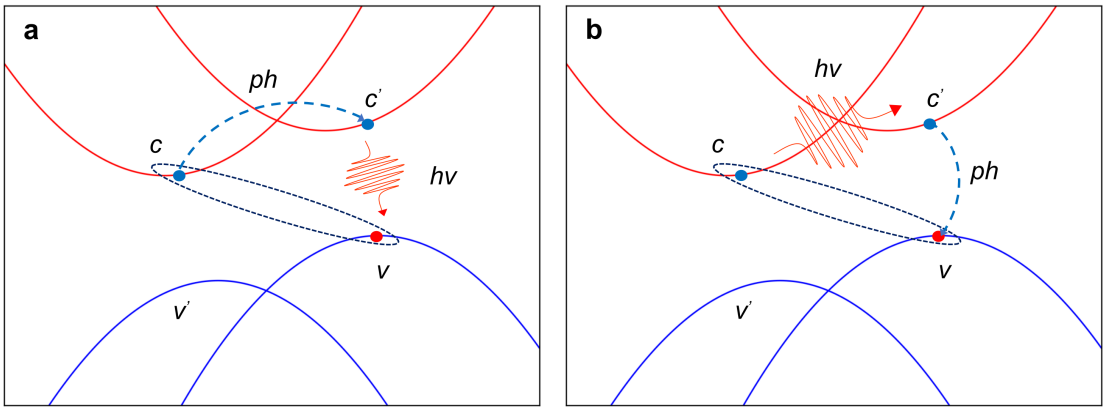

Figure 3.1: Schematic illustration of phonon-assisted radiative processes. (a) Intraband phonon scattering (ph) combined with interband photon emission ($\hbar\nu$), and (b) interband phonon scattering combined with intraband photon emission.

implies that a single exciton corresponds to an interband transition, while describing intraband transitions requires the involvement of two excitons. We start with the non-interacting Hamiltonian of exciton, phonon, and photon fields:

$$\begin{aligned}\hat{H}_0 &= \hat{H}_{ex} + \hat{H}_{ph} + \hat{H}_\gamma \\ &= \sum_{S,\mathbf{Q}} \hbar\omega_{S(\mathbf{Q})} \hat{c}^\dagger_{S(\mathbf{Q})} \hat{c}_{S(\mathbf{Q})} + \sum_{\nu\mathbf{q}} \hbar\omega_{\nu\mathbf{q}} \left(\hat{b}^\dagger_{\nu\mathbf{q}} \hat{b}_{\nu\mathbf{q}} + \frac{1}{2} \right) \\ &+ \sum_{\lambda\bar{\mathbf{k}}} \hbar\omega_{\lambda\bar{\mathbf{k}}} \left(\hat{a}^\dagger_{\lambda\bar{\mathbf{k}}} \hat{a}_{\lambda\bar{\mathbf{k}}} + \frac{1}{2} \right),\end{aligned} \tag{3.2}$$

where ν and λ index the phonon and photon modes, respectively, and $\mathbf{q}$ and $\bar{\mathbf{k}}$ are their corresponding wavevectors. The operators $\hat{b}^{(\dagger)}$ and $\hat{a}^{(\dagger)}$ represent phonon and photon annihilation (creation) operators, respectively.

3.2.1 Exciton-Photon Hamiltonian

The exciton-photon interaction Hamiltonian is obtained by extending the electron-photon interaction Hamiltonian. In the length gauge [29], the substitution reads:

$$\hat{H}^{e-\gamma} = -\frac{e}{m}\hat{\mathbf{A}} \cdot \hat{\mathbf{p}} \quad \rightarrow \quad \hat{H}^{ex-\gamma} = -\frac{e}{m_{ex}}\hat{\mathbf{A}} \cdot \hat{\mathbf{p}}_{ex}, \tag{3.3}$$

where $\hat{\mathbf{A}}$ remains the photon vector potential, while $\hat{\mathbf{p}}_{ex}$ denotes the exciton momentum operator defined as

$$\hat{\mathbf{p}}_{ex} = -\frac{i}{\hbar} m_{ex}[\hat{\mathbf{r}}, \hat{H}_{ex}]. \tag{3.4}$$

Using the plane-wave expansion of the vector potential,

$$\hat{\mathbf{A}}(\mathbf{r}) = \sum_{\lambda\bar{\mathbf{k}}} \sqrt{\frac{\hbar}{2\omega_{\lambda\bar{\mathbf{k}}} V \epsilon_0}} \left(\mathbf{e}_{\lambda\bar{\mathbf{k}}} \hat{a}_{\lambda\bar{\mathbf{k}}} e^{i\bar{\mathbf{k}}\cdot\mathbf{r}} + \mathbf{e}^*_{\lambda\bar{\mathbf{k}}} \hat{a}^\dagger_{\lambda\bar{\mathbf{k}}} e^{-i\bar{\mathbf{k}}\cdot\mathbf{r}} \right), \tag{3.5}$$

the exciton-photon Hamiltonian becomes

$$\hat{H}^{ex-} = i \sum_{\lambda\bar{\mathbf{k}}} \sqrt{\frac{e^2}{2\hbar\omega_{\lambda\bar{\mathbf{k}}} V \epsilon_0}} \left(\mathbf{e}_{\lambda\bar{\mathbf{k}}} \hat{a}_{\lambda\bar{\mathbf{k}}} e^{i\bar{\mathbf{k}}\cdot\mathbf{r}} + \mathbf{e}^*_{\lambda\bar{\mathbf{k}}} \hat{a}^\dagger_{\lambda\bar{\mathbf{k}}} e^{-i\bar{\mathbf{k}}\cdot\mathbf{r}} \right) \cdot [\hat{\mathbf{r}}, \hat{H}_{ex}]. \tag{3.6}$$

Since the excitonic Hamiltonian $\hat{H}_{ex}$ is diagonal in the excitonic basis, we have:

$$\hat{H}_{ex}|S(\mathbf{Q})\rangle = E_{S(\mathbf{Q})}|S(\mathbf{Q})\rangle, \quad \hat{H}_{ex}|GS\rangle = 0, \tag{3.7}$$

where $|GS\rangle$ denotes the ground state (no exciton).

3.2.2 Exciton-Phonon Hamiltonian

Considering the electron-phonon interaction to first order in atomic displacement [32], the Hamiltonian can be written as

$$\hat{H}^{e-ph} = \sum_{\mathbf{k},\mathbf{q}} \sum_{mn\nu} g_{mn\nu}(\mathbf{k}, \mathbf{q}) \hat{d}^\dagger_{m,\mathbf{k}+\mathbf{q}} \hat{d}_{n,\mathbf{k}} (\hat{b}_{\mathbf{q}\nu} + \hat{b}^\dagger_{-\mathbf{q}\nu}), \tag{3.8}$$

where $\hat{d}$ denotes the electron field operator, and m and n label the band indices. The quantity $g_{mn\nu}(\mathbf{k}, \mathbf{q}) = \langle m\mathbf{k}+\mathbf{q}|\Delta_{\mathbf{q}\nu} v^{KS}|n\mathbf{k}\rangle$ represents the electron-phonon coupling matrix element in the phonon-mode representation, with $\Delta_{\mathbf{q}\nu} v^{KS}$ being the derivative of the Kohn-Sham potential obtained from DFPT calculations. The Born–von Karman (BvK) boundary condition is applied to the plane-wave basis [32], restricting the wavevector summations to the first Brillouin zone. For simplicity, the normalization factor $N_p^{-1/2}$ is omitted.

To define the exciton-phonon Hamiltonian, we begin with the electron-phonon interaction at first order in atomic displacement (higher-order effects such as two-phonon

processes would require including the Debye-Waller term) [32]:

$$\hat{H}^{e-ph} = \sum_{\mathbf{k},\mathbf{q}} \sum_{mn\nu} g_{mn\nu}(\mathbf{k},\mathbf{q}) \hat{d}^{\dagger}_{m,\mathbf{k}+\mathbf{q}} \hat{d}_{n,\mathbf{k}} (\hat{b}_{\mathbf{q}\nu} + \hat{b}^{\dagger}_{-\mathbf{q}\nu}), \tag{3.9}$$

where $\hat{d}$ is the electron field operator, and m and n denote conduction or valence band indices. The quantity $g_{mn\nu}(\mathbf{k},\mathbf{q}) = \langle m(\mathbf{k}+\mathbf{q})|\Delta_{\mathbf{q}\nu} v^{KS}|n\mathbf{k}\rangle$ represents the electron-phonon coupling matrix element, with $\Delta_{\mathbf{q}\nu} v^{KS}$ being the derivative of the Kohn-Sham potential obtained from DFPT calculations. For simplicity, we omit a normalization factor $N_p^{-1/2}$ associated with the number of unit cells in the Born–von Karman supercell [32].

The electron-phonon Hamiltonian describes both intraband transitions, where m and n belong to the same band (either valence-valence or conduction-conduction), and interband transitions, where m and n belong to different bands (valence-conduction). The exciton, as the solution of the Bethe-Salpeter Equation (BSE), is a quasiparticle defined in the electron-hole (valence-conduction) space [68]. The exciton creation operator is given by

$$\hat{c}^{\dagger}_{S(\mathbf{Q})} = \sum_{vc\mathbf{k}} A^{S(\mathbf{Q})}_{vc\mathbf{k}} \hat{d}^{\dagger}_{c,\mathbf{k}+\mathbf{Q}} \hat{d}_{v,\mathbf{k}}, \tag{3.10}$$

where $A^{S(\mathbf{Q})}_{vc\mathbf{k}}$ are the exciton amplitudes, and $\mathbf{Q}$ is the center-of-mass momentum.

This formalism implies that a single exciton corresponds to an interband transition. In contrast, describing an intraband transition requires two excitons (since intraband transitions correspond to general valence-valence or conduction-conduction transitions).

Thus, the exciton-phonon Hamiltonian can be categorized as follows:

- It describes intraband transitions if it contains one exciton creation and one exciton annihilation operator.
- It describes interband transitions if it contains only a single excitonic field operator (either creation or annihilation).

To derive the intraband exciton-phonon Hamiltonian, we begin by evaluating the probability amplitude for an exciton-to-exciton transition mediated by the electron-phonon interaction, given in Eq. (3.9). We then promote this amplitude to an operator expression by inserting the corresponding excitonic field operators:

$$\hat{H}^{ex-ph}_{intra} = \sum_{SS'} \sum_{\mathbf{qQ}} \langle S'(\mathbf{Q}+\mathbf{q})|\hat{H}^{e-ph}|S(\mathbf{Q})\rangle \, \hat{c}^{\dagger}_{S'(\mathbf{Q}+\mathbf{q})} \hat{c}_{S(\mathbf{Q})}. \tag{3.11}$$

Note that this amplitude involves only excitonic states; the phonon field remains unaltered in this procedure.

Using the exciton definition in terms of the electron-hole basis,

$$|S(\mathbf{Q})\rangle = \sum_{vc\mathbf{k}} A_{vc\mathbf{k}}^{S(\mathbf{Q})} \hat{d}^{\dagger}_{c,\mathbf{k}+\mathbf{Q}} \hat{d}_{v,\mathbf{k}} |GS\rangle, \tag{3.12}$$

the matrix element becomes

$$\begin{aligned}\langle S'(\mathbf{Q}+\mathbf{q})|\hat{H}^{e-ph}|S(\mathbf{Q})\rangle = \sum_{vc\mathbf{k}} \sum_{v'c'\mathbf{k}'} \sum_{\mathbf{k}''\mathbf{q}'} \sum_{mn\nu} A_{vc\mathbf{k}}^{S'(\mathbf{Q}+\mathbf{q})*} A_{v'c'\mathbf{k}'}^{S(\mathbf{Q})} g_{mn\nu}(\mathbf{k}'', \mathbf{q}')(\hat{b}_{\mathbf{q}'\nu} + \hat{b}^{\dagger}_{-\mathbf{q}'\nu}) \\ \times \langle GS|\hat{d}^{\dagger}_{v,\mathbf{k}} \hat{d}_{c,\mathbf{k}+\mathbf{Q}+\mathbf{q}} \hat{d}^{\dagger}_{m,\mathbf{k}''+\mathbf{q}'} \hat{d}_{n,\mathbf{k}''} \hat{d}^{\dagger}_{c',\mathbf{k}'+\mathbf{Q}} \hat{d}_{v',\mathbf{k}'}|GS\rangle.\end{aligned} \tag{3.13}$$

To evaluate the expectation value, we apply Wick's theorem for six fermionic operators. The non-vanishing contractions give:

$$\begin{aligned}&\langle \hat{d}^{\dagger}_{v,\mathbf{k}} \hat{d}_{c,\mathbf{k}+\mathbf{Q}+\mathbf{q}} \hat{d}^{\dagger}_{m,\mathbf{k}''+\mathbf{q}'} \hat{d}_{n,\mathbf{k}''} \hat{d}^{\dagger}_{c',\mathbf{k}'+\mathbf{Q}} \hat{d}_{v',\mathbf{k}'} \rangle \\ &= \langle \hat{d}_{c,\mathbf{k}+\mathbf{Q}+\mathbf{q}} \hat{d}^{\dagger}_{m,\mathbf{k}''+\mathbf{q}'} \rangle \langle \hat{d}_{n,\mathbf{k}''} \hat{d}^{\dagger}_{c',\mathbf{k}'+\mathbf{Q}} \rangle \langle \hat{d}^{\dagger}_{v,\mathbf{k}} \hat{d}_{v',\mathbf{k}'} \rangle \\ &\quad - \langle \hat{d}^{\dagger}_{v,\mathbf{k}} \hat{d}_{n,\mathbf{k}''} \rangle \langle \hat{d}^{\dagger}_{m,\mathbf{k}''+\mathbf{q}'} \hat{d}_{v',\mathbf{k}'} \rangle \langle \hat{d}_{c,\mathbf{k}+\mathbf{Q}+\mathbf{q}} \hat{d}^{\dagger}_{c',\mathbf{k}'+\mathbf{Q}} \rangle \\ &= \delta_{c,m}\delta_{\mathbf{k}+\mathbf{Q}+\mathbf{q},\mathbf{k}''+\mathbf{q}'}\delta_{n,c'}\delta_{\mathbf{k}'',\mathbf{k}'+\mathbf{Q}}\delta_{v,v'}\delta_{\mathbf{k},\mathbf{k}'} \\ &\quad - \delta_{v,n}\delta_{\mathbf{k},\mathbf{k}''}\delta_{m,v'}\delta_{\mathbf{k}''+\mathbf{q}',\mathbf{k}'}\delta_{c,c'}\delta_{\mathbf{k}+\mathbf{Q}+\mathbf{q},\mathbf{k}'+\mathbf{Q}}.\end{aligned} \tag{3.14}$$

Here we exclude the contraction $\langle \hat{d}^{\dagger}_{m,\mathbf{k}''+\mathbf{q}'} \hat{d}_{n,\mathbf{k}''} \rangle$, as it yields disconnected contributions [4].

By substituting Eqs. (3.13) and (3.14) in Eq. (3.11), we obtain

$$\hat{H}^{ex-ph}_{intra} = \sum_{SS'} \sum_{\mathbf{q}\mathbf{Q}\nu} \mathcal{G}_{S'S\nu}(\mathbf{Q}, \mathbf{q}) \hat{c}^{\dagger}_{S'(\mathbf{Q}+\mathbf{q})} \hat{c}_{S(\mathbf{Q})} (\hat{b}_{\mathbf{q}\nu} + \hat{b}^{\dagger}_{-\mathbf{q}\nu}) \tag{3.15}$$

with

$$\mathcal{G}_{S'S\nu}(\mathbf{Q}, \mathbf{q}) = \sum_{vcc'\mathbf{k}} A_{vc\mathbf{k}}^{S'(\mathbf{Q}+\mathbf{q})*} A_{vc'\mathbf{k}}^{S(\mathbf{Q})} g_{cc'\nu}(\mathbf{k}+\mathbf{Q}, \mathbf{q}) - \sum_{cvv'\mathbf{k}} A_{vc\mathbf{k}}^{S'(\mathbf{Q}+\mathbf{q})*} A_{v'c\mathbf{k}+\mathbf{q}}^{S(\mathbf{Q})} g_{v'v\nu}(\mathbf{k}, \mathbf{q}), \tag{3.16}$$

where we have done a shift $\mathbf{k} = \mathbf{k}' - \mathbf{Q}$ in the first term of the RHS of Eq. (3.22). To derive the interband ex-ph Hamiltonian, we follow the same procedure but for the recombination process (we are interested in photon emission, if we want to consider also

photon absorption the excitation process has to be taken into account), namely

$$\hat{H}^{ex-ph}_{inter} = \sum_{SQ} \langle G|\hat{H}^{e-ph}|S(\mathbf{Q})\rangle \hat{c}_{S(\mathbf{Q})} \tag{3.17}$$

$$= \sum_{SQ}\sum_{mn\nu}\sum_{\nu c\mathbf{k}}\sum_{\mathbf{k}'\mathbf{q}} A^{S(\mathbf{Q})}_{\nu c\mathbf{k}} g_{mn\nu}(\mathbf{k}',\mathbf{q})\langle \hat{d}^{\dagger}_{m,\mathbf{k}'+\mathbf{q}}\hat{d}_{n,\mathbf{k}'}\hat{d}^{\dagger}_{c,\mathbf{k}+\mathbf{Q}}\hat{d}_{\nu,\mathbf{k}}\rangle \hat{c}_{S(\mathbf{Q})}(\hat{b}_{\mathbf{q}\nu}+\hat{b}^{\dagger}_{-\mathbf{q}\nu})$$

$$= \sum_{SQ}\sum_{mn\nu}\sum_{\nu c\mathbf{k}}\sum_{\mathbf{k}'\mathbf{q}} A^{S(\mathbf{Q})}_{\nu c\mathbf{k}} g_{mn\nu}(\mathbf{k}',\mathbf{q})\delta_{m,\nu}\delta_{\mathbf{k}'+\mathbf{q},\mathbf{k}}\delta_{n,c}\delta_{\mathbf{k}',\mathbf{k}+\mathbf{Q}}\hat{c}_{S(\mathbf{Q})}(\hat{b}_{\mathbf{q}\nu}+\hat{b}^{\dagger}_{-\mathbf{q}\nu})$$

$$= \sum_{SQ\nu}\left[\sum_{\nu c\mathbf{k}} A^{S(\mathbf{Q})}_{\nu c\mathbf{k}} g_{\nu c\nu}(\mathbf{k}+\mathbf{Q},-\mathbf{Q})\right]\hat{c}_{S(\mathbf{Q})}(\hat{b}_{-\mathbf{Q}\nu}+\hat{b}^{\dagger}_{\mathbf{Q}\nu}). \tag{3.18}$$

Therefore, we can define

$$\hat{H}^{ex-ph}_{inter} = \sum_{SQ\nu} \mathcal{G}_{S\nu}(\mathbf{Q})\hat{c}_{S(\mathbf{Q})}(\hat{b}_{-\mathbf{Q}\nu}+\hat{b}^{\dagger}_{\mathbf{Q}\nu}), \tag{3.19}$$

with

$$\mathcal{G}_{S\nu}(\mathbf{Q}) = \sum_{\nu c\mathbf{k}} A^{S(\mathbf{Q})}_{\nu c\mathbf{k}} g_{\nu c\nu}(\mathbf{k}+\mathbf{Q},-\mathbf{Q}). \tag{3.20}$$

Therefore, the total Hamiltonian $\hat{H}$ is defined as $\hat{H}_0 + \hat{H}_{int}$, where $\hat{H}_{int}$ represents the interacting Hamiltonian, given by: $\hat{H}_{int} = \hat{H}^{ex-\gamma} + \hat{H}^{ex-ph}_{intra} + \hat{H}^{ex-ph}_{inter}$,

$$\hat{H}^{ex-ph}_{intra} = \sum_{SS'}\sum_{\mathbf{q}\mathbf{Q}\nu} \mathcal{G}_{S'S\nu}(\mathbf{Q},\mathbf{q})\hat{c}^{\dagger}_{S'(\mathbf{Q}+\mathbf{q})}\hat{c}_{S(\mathbf{Q})}(\hat{b}_{\mathbf{q}\nu}+\hat{b}^{\dagger}_{-\mathbf{q}\nu});$$

$$\hat{H}^{ex-ph}_{inter} = \sum_{SQ\nu} \mathcal{G}_{S\nu}(\mathbf{Q})\hat{c}_{S(\mathbf{Q})}(\hat{b}_{-\mathbf{Q}\nu}+\hat{b}^{\dagger}_{\mathbf{Q}\nu}), \tag{3.21}$$

the intraband and interband exciton-phonon interaction Hamiltonians are derived by projecting the electron-phonon coupling from the one-particle basis onto the excitonic basis, where $\mathcal{G}$ is the interband and intraband exciton-phonon matrix element

$$\mathcal{G}_{S'S\nu}(\mathbf{Q},\mathbf{q}) = \sum_{\nu cc'\mathbf{k}} A^{S'(\mathbf{Q}+\mathbf{q})*}_{\nu c\mathbf{k}} A^{S(\mathbf{Q})}_{\nu c'\mathbf{k}} g_{cc'\nu}(\mathbf{k}+\mathbf{Q},\mathbf{q})$$
$$- \sum_{c\nu\nu'\mathbf{k}} A^{S'(\mathbf{Q}+\mathbf{q})*}_{\nu c\mathbf{k}} A^{S(\mathbf{Q})}_{\nu' c\mathbf{k}+\mathbf{q}} g_{\nu'\nu\nu}(\mathbf{k},\mathbf{q});$$

$$\mathcal{G}_{Sv}(\mathbf{Q}) = \sum_{vc\mathbf{k}} A^{S(\mathbf{Q})}_{vc\mathbf{k}} g_{vcv}(\mathbf{k}+\mathbf{Q}, -\mathbf{Q}). \tag{3.22}$$

3.3 Second-Order Time-Dependent Perturbation Theory

The phonon-assisted radiative transition probability is expressed in terms of the time-dependent perturbative coefficients [98] $c^{(n)}_{i\to f}(t)$ as: $P_{i\to f}(t) = \left|c^{(1)}_{i\to f}(t) + c^{(2)}_{i\to f}(t) + \cdots\right|^2$, for the specific $i \to f$ transition under consideration, the first-order coefficient $c^{(1)}_{i\to f}(t)$ vanishes. Contributions from higher-order terms beyond the second order are not included in this analysis.

We are interested in the photon emission rate associated with exciton recombination mediated by phonons, which is described by

$$\begin{aligned} c^{(2)}_{i\to f}(t) = &-\frac{1}{\hbar^2}\int_{-\infty}^{t} dt' \int_{-\infty}^{t'} dt'' \lim_{\eta,\eta'\to 0^+} \sum_{m} e^{it'(\omega_{fm}-i\eta)} e^{it''(\omega_{mi}-i\eta')} \\ &\times \left[\langle f|\, \hat{H}^{ex-ph}_{inter}\, |m\rangle \langle m|\, \hat{H}^{ex-}\, |i\rangle + \langle f|\, \hat{H}^{ex-}\, |m\rangle \langle m|\, \hat{H}^{ex-ph}_{intra}\, |i\rangle\right] \\ = &\, c^{(2)}_{(i\to f),1}(t) + c^{(2)}_{(i\to f),2}(t), \end{aligned} \tag{3.23}$$

where $\omega_{ij} = (E_i - E_j)/\hbar$ and E_i denotes the energy of the non-interacting Hamiltonian. We use only the interband (intraband) exciton-phonon Hamiltonian for the first (second) term because the complementary contributions yield vanishing amplitude.

We consider the initial state as an exciton state

$$|i\rangle = |S(\mathbf{Q})\rangle \otimes |\Omega\rangle \otimes |0\rangle = |S(\mathbf{Q}), \Omega, 0\rangle\,,$$

and the final state as an emitted photon accompanied by the absorption or emission of a phonon in the exciton ground state:

$$|f\rangle = |G, \Omega \pm 1_{v,\mp\mathbf{q}}, 1_{\lambda\bar{\mathbf{k}}}\rangle\,,$$

where $|\Omega\rangle$ represents the phonon bath.

Let us focus on the second term on the right-hand side of Eq. (3.23). The intermediate states that yield non-zero contributions are exciton states plus the absorption or emission of a phonon, i.e.,

$$|m\rangle = |S'(\mathbf{Q}'), \Omega \pm 1_{v',\mp\mathbf{q}'}, 0\rangle\,,$$

leading to the summation $\sum_m = \sum_{S'\mathbf{Q}'} \sum_{\mathbf{q}'v'}$.

Thus, the second-order coefficient becomes

$$
\begin{aligned}
c^{(2)}_{(i\to f),2}(t) = -\frac{1}{\hbar^2}\int_{-\infty}^{t} dt' \int_{-\infty}^{t'} dt'' \lim_{\eta,\eta'\to 0^+} \sum_{S'\mathbf{Q}'} \sum_{\mathbf{q}'\nu'} \\
&\times e^{it'(\pm\omega_{\nu,\mp\mathbf{q}}+\omega_{\lambda\bar{\mathbf{k}}}-\omega_{S'(\mathbf{Q}')}\mp\omega_{\nu',\mp\mathbf{q}'}-i\eta)} e^{it''(\omega_{S'(\mathbf{Q}')}\pm\omega_{\nu',\mp\mathbf{q}'}-\omega_{S(\mathbf{Q})}-i\eta')} \\
&\times \langle G, \Omega \pm 1_{\nu,\mp\mathbf{q}}, 1_{\lambda\bar{\mathbf{k}}} | \hat{H}^{ex-} | S'(\mathbf{Q}'), \Omega \pm 1_{\nu',\mp\mathbf{q}'}, 0\rangle \\
&\times \langle S'(\mathbf{Q}'), \Omega \pm 1_{\nu',\mp\mathbf{q}'}, 0 | \hat{H}^{ex-ph}_{intra} | S(\mathbf{Q}), \Omega, 0\rangle. \qquad (3.24)
\end{aligned}
$$

We now calculate the exciton-phonon probability amplitude:

$$
\begin{aligned}
&\langle S'(\mathbf{Q}'), \Omega \pm 1_{\nu',\mp\mathbf{q}'}, 0 | \hat{H}^{ex-ph}_{intra} | S(\mathbf{Q}), \Omega, 0\rangle \\
&= \sum_{S''S'''} \sum_{\mathbf{q}''\mathbf{Q}''\nu''} \mathcal{G}_{S'''S''\nu''}(\mathbf{Q}'', \mathbf{q}'') \langle S'(\mathbf{Q}') | \hat{c}^{\dagger}_{S'''(\mathbf{Q}''+\mathbf{q}'')} \hat{c}_{S''(\mathbf{Q}'')} | S(\mathbf{Q})\rangle \\
&\quad \times \langle \Omega \pm 1_{\nu',\mp\mathbf{q}'} | \hat{b}_{\mathbf{q}''\nu''} + \hat{b}^{\dagger}_{-\mathbf{q}''\nu''} | \Omega\rangle \\
&= \sum_{S''S'''} \sum_{\mathbf{q}''\mathbf{Q}''\nu''} \mathcal{G}_{S'''S''\nu''}(\mathbf{Q}'', \mathbf{q}'') \delta_{S,S''}\delta_{\mathbf{Q},\mathbf{Q}''}\delta_{S',S'''}\delta_{\mathbf{Q}',\mathbf{Q}''+\mathbf{q}''} \\
&\quad \times \sqrt{n_{\nu''}(\mp\mathbf{q}'') + \frac{1}{2} \pm \frac{1}{2}}\, \delta_{\nu'',\nu'}\delta_{\mathbf{q}'',\mathbf{q}'} \\
&= \mathcal{G}_{S'S\nu'}(\mathbf{Q}, \mathbf{q}') \sqrt{n_{\nu'}(\mp\mathbf{q}') + \frac{1}{2} \pm \frac{1}{2}}\, \delta_{\mathbf{Q}',\mathbf{Q}+\mathbf{q}'}. \qquad (3.25)
\end{aligned}
$$

Next, the exciton-photon probability amplitude, using the Hamiltonian from Eq. (3.6), is nonzero only for photon emission:

$$
\begin{aligned}
&\langle G, \Omega \pm 1_{\nu,\mp\mathbf{q}}, 1_{\lambda\bar{\mathbf{k}}} | \hat{H}^{ex-} | S'(\mathbf{Q}'), \Omega \pm 1_{\nu',\mp\mathbf{q}'}, 0\rangle \\
&= i \sum_{\lambda'\bar{\mathbf{k}}'} \sqrt{\frac{e^2}{2\hbar\omega_{\lambda'\bar{\mathbf{k}}'} V \epsilon_0}}\, \mathbf{e}^*_{\lambda'\bar{\mathbf{k}}'} \cdot \langle G | e^{-i\bar{\mathbf{k}}'\cdot\mathbf{r}} [\hat{\mathbf{r}}, \hat{H}_{ex}] | S'(\mathbf{Q}')\rangle \\
&\quad \times \langle \Omega \pm 1_{\nu,\mp\mathbf{q}} | \Omega \pm 1_{\nu',\mp\mathbf{q}'}\rangle \langle 1_{\lambda\bar{\mathbf{k}}} | \hat{a}^{\dagger}_{\lambda'\bar{\mathbf{k}}'} | 0\rangle \\
&= i \sum_{\lambda'\bar{\mathbf{k}}'} \sqrt{\frac{e^2}{2\hbar\omega_{\lambda'\bar{\mathbf{k}}'} V \epsilon_0}}\, E_{S'(\mathbf{Q}')}\, \mathbf{e}^*_{\lambda'\bar{\mathbf{k}}'} \cdot \langle G | e^{-i\bar{\mathbf{k}}'\cdot\mathbf{r}} \hat{\mathbf{r}} | S'(\mathbf{Q}')\rangle\, \delta_{\nu,\nu'}\delta_{\mathbf{q},\mathbf{q}'}\delta_{\lambda,\lambda'}\delta_{\bar{\mathbf{k}},\bar{\mathbf{k}}'} \\
&\approx i \sqrt{\frac{e^2}{2\hbar\omega_{\lambda\bar{\mathbf{k}}} V \epsilon_0}}\, E_{S'(\mathbf{Q}')}\, \mathbf{e}^*_{\lambda\bar{\mathbf{k}}} \cdot \langle G | \hat{\mathbf{r}} | S'(\mathbf{Q}')\rangle\, \delta_{\mathbf{Q}',-\bar{\mathbf{k}}}\delta_{\nu,\nu'}\delta_{\mathbf{q},\mathbf{q}'}. \qquad (3.26)
\end{aligned}
$$

where in the last line we have used the dipole approximation

$$
\langle G | e^{-i\bar{\mathbf{k}}\cdot\mathbf{r}} \hat{\mathbf{r}} | S(\mathbf{Q})\rangle \approx \langle G | \hat{\mathbf{r}} | S(\mathbf{Q})\rangle\, \delta_{\mathbf{Q},-\bar{\mathbf{k}}}, \qquad (3.27)
$$

and we define the exciton-photon matrix element as

$$\mathcal{M}_{S(\mathbf{Q}),\lambda\bar{\mathbf{k}}} = i\sqrt{\frac{e^2}{2\hbar\omega_{\lambda\bar{\mathbf{k}}}V\epsilon_0}}E_{S(\mathbf{Q})}\,\mathbf{e}^*_{\lambda\bar{\mathbf{k}}}\cdot\langle G|\,\hat{\mathbf{r}}\,|S(\mathbf{Q})\rangle\,. \tag{3.28}$$

By inserting the results of Eqs. (3.25) and (3.26) in Eq. (3.24) we obtain

$$\begin{aligned} c^{(2)}_{(i\to f),2}(t) = &-\frac{1}{\hbar^2}\int_{-\infty}^{t}dt'\int_{-\infty}^{t'}dt''\lim_{\eta,\eta'\to 0^+} \qquad (3.29)\\ &\sum_{S'\mathbf{Q}'}\sum_{\mathbf{q}'\nu'} e^{it'(\pm\omega_{\nu,\mp\mathbf{q}}+\omega_{\lambda\bar{\mathbf{k}}}-\omega_{S'(\mathbf{Q}')}\mp\omega_{\nu',\mp\mathbf{q}'}-i\eta)}e^{it''(\omega_{S'(\mathbf{Q}')}\pm\omega_{\nu',\mp\mathbf{q}'}-\omega_{S(\mathbf{Q})}-i\eta')}\\ &\times\mathcal{G}_{S'S\nu'}(\mathbf{Q},\mathbf{q}')\mathcal{M}_{S'(\mathbf{Q}'),\lambda\bar{\mathbf{k}}}\sqrt{n_{\nu'}(\mp\mathbf{q}')+\frac{1}{2}\pm\frac{1}{2}}\delta_{\mathbf{Q}',\mathbf{Q}+\mathbf{q}'}\delta_{\mathbf{Q}',-\bar{\mathbf{k}}}\delta_{\nu,\nu'}\delta_{\mathbf{q},\mathbf{q}'}\\ &=-\frac{1}{\hbar^2}\int_{-\infty}^{t}dt'\int_{-\infty}^{t'}dt''\lim_{\eta,\eta'\to 0^+}\sum_{S'} e^{it'(\omega_{\lambda\bar{\mathbf{k}}}-\omega_{S'(\mathbf{Q}+\mathbf{q})}-i\eta)}e^{it''(\omega_{S'(\mathbf{Q}+\mathbf{q})}\pm\omega_{\nu,\mp\mathbf{q}}-\omega_{S(\mathbf{Q})}-i\eta')}\\ &\times\mathcal{G}_{S'S\nu}(\mathbf{Q},\mathbf{q})\mathcal{M}_{S'(\mathbf{Q}+\mathbf{q}),\lambda\bar{\mathbf{k}}}\sqrt{n_{\nu'}(\mp\mathbf{q}')+\frac{1}{2}\pm\frac{1}{2}}\delta_{\mathbf{Q}+\mathbf{q},-\bar{\mathbf{k}}}. \qquad (3.30)\end{aligned}$$

The time integrals give

$$\begin{aligned} &\lim_{\eta,\eta'\to 0^+}\int_{-\infty}^{t}dt'\int_{-\infty}^{t'}dt''e^{it'(\omega_{\lambda\bar{\mathbf{k}}}-\omega_{S'(\mathbf{Q}+\mathbf{q})}-i\eta)}e^{it''(\omega_{S'(\mathbf{Q}+\mathbf{q})}\pm\omega_{\nu,\mp\mathbf{q}}-\omega_{S(\mathbf{Q})}-i\eta')}\\ &=-i\lim_{\eta,\eta'\to 0^+}\int_{-\infty}^{t}dt'\frac{e^{it'(\omega_{\lambda\bar{\mathbf{k}}}\pm\omega_{\nu,\mp\mathbf{q}}-\omega_{S(\mathbf{Q})}-i\eta-i\eta')}}{\omega_{S'(\mathbf{Q}+\mathbf{q})}\pm\omega_{\nu,\mp\mathbf{q}}-\omega_{S(\mathbf{Q})}-i\eta'}\\ &=-\lim_{\eta,\eta'\to 0^+}\frac{e^{it(\omega_{\lambda\bar{\mathbf{k}}}\pm\omega_{\nu,\mp\mathbf{q}}-\omega_{S(\mathbf{Q})}-i\eta-i\eta')}}{\omega_{\lambda\bar{\mathbf{k}}}\pm\omega_{\nu,\mp\mathbf{q}}-\omega_{S(\mathbf{Q})}-i\eta-i\eta'}\frac{1}{\omega_{S'(\mathbf{Q}+\mathbf{q})}\pm\omega_{\nu,\mp\mathbf{q}}-\omega_{S(\mathbf{Q})}-i\eta'}. \qquad (3.31)\end{aligned}$$

In the end, we obtain

$$\begin{aligned} c^{(2)}_{(i\to f),2}(t) = &\frac{1}{\hbar^2}\lim_{\eta,\eta'\to 0^+}\frac{e^{it(\omega_{\lambda\bar{\mathbf{k}}}\pm\omega_{\nu,\mp\mathbf{q}}-\omega_{S(\mathbf{Q})}-i\eta-i\eta')}}{\omega_{\lambda\bar{\mathbf{k}}}\pm\omega_{\nu,\mp\mathbf{q}}-\omega_{S(\mathbf{Q})}-i\eta-i\eta'}\sqrt{n_\nu(\mp\mathbf{q})+\frac{1}{2}\pm\frac{1}{2}}\delta_{\mathbf{Q}+\mathbf{q},-\bar{\mathbf{k}}}\\ &\times\sum_{S'}\frac{\mathcal{G}_{S'S\nu}(\mathbf{Q},\mathbf{q})\mathcal{M}_{S'(\mathbf{Q}+\mathbf{q}),\lambda\bar{\mathbf{k}}}}{\omega_{S'(\mathbf{Q}+\mathbf{q})}\pm\omega_{\nu,\mp\mathbf{q}}-\omega_{S(\mathbf{Q})}-i\eta'}. \qquad (3.32)\end{aligned}$$

Let's now calculate the first term on the RHS of Eq. (3.23). The intermediate state that gives non-zero amplitude are now an exciton plus a photon, i.e., $|m\rangle = |S'(\mathbf{Q}'),\Omega,1_{\lambda'\bar{\mathbf{k}}'}\rangle$

and so $\sum_m = \sum_{S'\mathbf{Q}'} \sum_{\lambda'\bar{\mathbf{k}}'}$

$$c^{(2)}_{(i\to f),1}(t) = -\frac{1}{\hbar^2}\int_{-\infty}^{t} dt' \int_{-\infty}^{t'} dt'' \lim_{\eta,\eta'\to 0^+} \tag{3.33}$$

$$\sum_{S'\mathbf{Q}'}\sum_{\lambda'\bar{\mathbf{k}}'} e^{it'(\pm\omega_{\nu,\mp\mathbf{q}}+\omega_{\lambda\bar{\mathbf{k}}}-\omega_{S'(\mathbf{Q}')}-\omega_{\lambda',\bar{\mathbf{k}}'}-i\eta)} e^{it''(\omega_{S'(\mathbf{Q}')}+\omega_{\lambda',\bar{\mathbf{k}}'}-\omega_{S(\mathbf{Q})}-i\eta')}$$

$$\times \langle G, \Omega \pm 1_{\nu,\mp\mathbf{q}}, 1_{\lambda\bar{\mathbf{k}}}|H^{ex-ph}_{inter}|S'(\mathbf{Q}'), \Omega, 1_{\lambda'\bar{\mathbf{k}}'}\rangle\langle S'(\mathbf{Q}'), \Omega, 1_{\lambda'\bar{\mathbf{k}}'}|\hat{H}^{ex-}|S(\mathbf{Q}), \Omega, 0\rangle. \tag{3.34}$$

We then calculate the exciton-photon probability amplitude:

$$\begin{aligned}
&\langle S'(\mathbf{Q}'), \Omega, 1_{\lambda'\bar{\mathbf{k}}'}|\hat{H}^{ex-}|S(\mathbf{Q}), \Omega, 0\rangle \\
&= i\sum_{\lambda''\bar{\mathbf{k}}''}\sqrt{\frac{e^2}{2\hbar\omega_{\lambda''\bar{\mathbf{k}}''}V\epsilon_0}}\,\mathbf{e}^*_{\lambda''\bar{\mathbf{k}}''}\cdot\langle S'(\mathbf{Q}')|e^{-i\bar{\mathbf{k}}''\cdot\mathbf{r}}[\hat{\mathbf{r}}, \hat{H}_{ex}]|S(\mathbf{Q})\rangle\langle 1_{\lambda'\bar{\mathbf{k}}'}|\hat{a}^\dagger_{\lambda''\bar{\mathbf{k}}''}|0\rangle \\
&= i\sum_{\lambda''\bar{\mathbf{k}}''}\sqrt{\frac{e^2}{2\hbar\omega_{\lambda''\bar{\mathbf{k}}''}V\epsilon_0}}(E_{S(\mathbf{Q})}-E_{S'(\mathbf{Q}')})\,\mathbf{e}^*_{\lambda''\bar{\mathbf{k}}''}\cdot\langle S'(\mathbf{Q}')|e^{-i\bar{\mathbf{k}}''\cdot\mathbf{r}}\hat{\mathbf{r}}|S(\mathbf{Q})\rangle\delta_{\lambda',\lambda''}\delta_{\bar{\mathbf{k}}',\bar{\mathbf{k}}''} \\
&\approx i\sqrt{\frac{e^2}{2\hbar\omega_{\lambda'\bar{\mathbf{k}}'}V\epsilon_0}}(E_{S(\mathbf{Q})}-E_{S'(\mathbf{Q}')})\,\mathbf{e}^*_{\lambda'\bar{\mathbf{k}}'}\cdot\langle S'(\mathbf{Q}')|\hat{\mathbf{r}}|S(\mathbf{Q})\rangle\delta_{\mathbf{Q}-\mathbf{Q}',-\bar{\mathbf{k}}'} \\
&= \mathcal{M}_{S'(\mathbf{Q}')S(\mathbf{Q}),\lambda'\bar{\mathbf{k}}'}\,\delta_{\mathbf{Q}-\mathbf{Q}',-\bar{\mathbf{k}}'}.
\end{aligned} \tag{3.35}$$

where we used the dipole approximation

$$\langle S'(\mathbf{Q}')|e^{-i\bar{\mathbf{k}}''\cdot\mathbf{r}}\hat{\mathbf{r}}|S(\mathbf{Q})\rangle \approx \langle S'(\mathbf{Q}')|\hat{\mathbf{r}}|S(\mathbf{Q})\rangle\delta_{\mathbf{Q}-\mathbf{Q}',-\bar{\mathbf{k}}''}, \tag{3.36}$$

and define the exciton-photon matrix element as

$$\mathcal{M}_{S'(\mathbf{Q}')S(\mathbf{Q}),\lambda'\bar{\mathbf{k}}'} = i\sqrt{\frac{e^2}{2\hbar\omega_{\lambda'\bar{\mathbf{k}}'}V\epsilon_0}}(E_{S(\mathbf{Q})}-E_{S'(\mathbf{Q}')})\,\mathbf{e}^*_{\lambda'\bar{\mathbf{k}}'}\cdot\langle S'(\mathbf{Q}')|\hat{\mathbf{r}}|S(\mathbf{Q})\rangle. \tag{3.37}$$

The exciton-phonon probability amplitude is

$$\begin{aligned}
&\langle G, \Omega \pm 1_{\nu,\mp\mathbf{q}}, 1_{\lambda\bar{\mathbf{k}}}|\hat{H}^{ex-ph}_{inter}|S'(\mathbf{Q}'), \Omega, 1_{\lambda'\bar{\mathbf{k}}'}\rangle \\
&= \sum_{S''\mathbf{Q}''\nu'}\mathcal{G}_{S''\nu'}(\mathbf{Q}'')\langle G|\hat{c}_{S''(\mathbf{Q}'')}|S'(\mathbf{Q}')\rangle\langle\Omega \pm 1_{\nu,\mp\mathbf{q}}|\hat{b}_{-\mathbf{Q}''\nu'}+\hat{b}^\dagger_{\mathbf{Q}''\nu'}|\Omega\rangle\langle 1_{\lambda\bar{\mathbf{k}}}|1_{\lambda'\bar{\mathbf{k}}'}\rangle \\
&= \sum_{S''\mathbf{Q}''\nu'}\mathcal{G}_{S''\nu'}(\mathbf{Q}'')\delta_{S'',S'}\delta_{\mathbf{Q}'',\mathbf{Q}'}\delta_{\lambda,\lambda'}\delta_{\bar{\mathbf{k}},\bar{\mathbf{k}}'}\delta_{\nu',\nu}\delta_{-\mathbf{Q}'',\mathbf{q}}\sqrt{n_{\nu'}(\pm\mathbf{Q}'')+\frac{1}{2}\pm\frac{1}{2}}
\end{aligned}$$

$$= \mathcal{G}_{S'\nu}(-\mathbf{q})\sqrt{n_\nu(\mp\mathbf{q}) + \frac{1}{2} \pm \frac{1}{2}}\delta_{\lambda,\lambda'}\delta_{\bar{\mathbf{k}},\bar{\mathbf{k}}'}\delta_{\mathbf{Q}',-\mathbf{q}}. \tag{3.38}$$

By inserting Eqs. (3.35) and (3.38) into Eq. (3.33), we obtain

$$\begin{aligned}
c^{(2)}_{(i\to f),1}(t) = &-\frac{1}{\hbar^2}\int_{-\infty}^{t} dt' \int_{-\infty}^{t'} dt'' \lim_{\eta,\eta'\to 0^+} \sum_{S'\mathbf{Q}'} \sum_{\lambda'\bar{\mathbf{k}}'} e^{it'(\pm\omega_{\nu,\mp\mathbf{q}} + \omega_{\lambda\bar{\mathbf{k}}} - \omega_{S'(\mathbf{Q}')} - \omega_{\lambda'\bar{\mathbf{k}}'} - i\eta)} \\
&\times e^{it''(\omega_{S'(\mathbf{Q}')} + \omega_{\lambda'\bar{\mathbf{k}}'} - \omega_{S(\mathbf{Q})} - i\eta')} \mathcal{G}_{S'\nu}(-\mathbf{q}) \mathcal{M}_{S'(\mathbf{Q}')S(\mathbf{Q}),\lambda'\bar{\mathbf{k}}'} \sqrt{n_\nu(\mp\mathbf{q}) + \frac{1}{2} \pm \frac{1}{2}} \\
&\times \delta_{\mathbf{Q}-\mathbf{Q}',-\bar{\mathbf{k}}'}\delta_{\lambda,\lambda'}\delta_{\bar{\mathbf{k}},\bar{\mathbf{k}}'}\delta_{\mathbf{Q}',-\mathbf{q}} \\
= &-\frac{1}{\hbar^2}\int_{-\infty}^{t} dt' \int_{-\infty}^{t'} dt'' \lim_{\eta,\eta'\to 0^+} \sum_{S'} e^{it'(\pm\omega_{\nu,\mp\mathbf{q}} - \omega_{S'(-\mathbf{q})} - i\eta)} e^{it''(\omega_{S'(-\mathbf{q})} + \omega_{\lambda\bar{\mathbf{k}}} - \omega_{S(\mathbf{Q})} - i\eta')} \\
&\times \mathcal{G}_{S'\nu}(-\mathbf{q}) \mathcal{M}_{S'(-\mathbf{q})S(\mathbf{Q}),\lambda\bar{\mathbf{k}}} \sqrt{n_\nu(\mp\mathbf{q}) + \frac{1}{2} \pm \frac{1}{2}} \delta_{\mathbf{Q}+\mathbf{q},-\bar{\mathbf{k}}}.
\end{aligned} \tag{3.39}$$

The time integrals give

$$\begin{aligned}
&\lim_{\eta,\eta'\to 0^+} \int_{-\infty}^{t} dt' \int_{-\infty}^{t'} dt'' e^{it'(\pm\omega_{\nu,\mp\mathbf{q}} - \omega_{S'(-\mathbf{q})} - i\eta)} e^{it''(\omega_{S'(-\mathbf{q})} + \omega_{\lambda\bar{\mathbf{k}}} - \omega_{S(\mathbf{Q})} - i\eta')} \\
&= -i \lim_{\eta,\eta'\to 0^+} \int_{-\infty}^{t} dt' \frac{e^{it'(\pm\omega_{\nu,\mp\mathbf{q}} + \omega_{\lambda\bar{\mathbf{k}}} - \omega_{S(\mathbf{Q})} - i\eta - i\eta')}}{\omega_{S'(-\mathbf{q})} + \omega_{\lambda\bar{\mathbf{k}}} - \omega_{S(\mathbf{Q})} - i\eta'} \\
&= -\lim_{\eta,\eta'\to 0^+} \frac{e^{it(\pm\omega_{\nu,\mp\mathbf{q}} + \omega_{\lambda\bar{\mathbf{k}}} - \omega_{S(\mathbf{Q})} - i\eta - i\eta')}}{\pm\omega_{\nu,\mp\mathbf{q}} + \omega_{\lambda\bar{\mathbf{k}}} - \omega_{S(\mathbf{Q})} - i\eta - i\eta'} \frac{1}{\omega_{S'(-\mathbf{q})} + \omega_{\lambda\bar{\mathbf{k}}} - \omega_{S(\mathbf{Q})} - i\eta'}.
\end{aligned} \tag{3.40}$$

Finally, we obtain

$$\begin{aligned}
c^{(2)}_{(i\to f),1}(t) = &\frac{1}{\hbar^2} \lim_{\eta,\eta'\to 0^+} \frac{e^{it(\omega_{\lambda,\bar{\mathbf{k}}} \pm \omega_{\nu,\mp\mathbf{q}} - \omega_{S(\mathbf{Q})} - i\eta - i\eta')}}{\omega_{\lambda,\bar{\mathbf{k}}} \pm \omega_{\nu,\mp\mathbf{q}} - \omega_{S(\mathbf{Q})} - i\eta - i\eta'} \sqrt{n_\nu(\mp\mathbf{q}) + \frac{1}{2} \pm \frac{1}{2}}\, \delta_{\mathbf{Q}+\mathbf{q},-\bar{\mathbf{k}}} \\
&\times \sum_{S'} \frac{\mathcal{G}_{S'\nu}(-\mathbf{q}) \mathcal{M}_{S'(-\mathbf{q})S(\mathbf{Q}),\lambda\bar{\mathbf{k}}}}{\omega_{S'(-\mathbf{q})} + \omega_{\lambda,\bar{\mathbf{k}}} - \omega_{S(\mathbf{Q})} - i\eta'}.
\end{aligned} \tag{3.41}$$

By summing Eqs. (3.32) and (3.41), we obtain the total second-order coefficient:

$$\begin{aligned}
c^{(2)}_{(i\to f)}(t) = &\frac{1}{\hbar^2} \lim_{\eta,\eta'\to 0^+} \frac{e^{it(\omega_{\lambda,\bar{\mathbf{k}}} \pm \omega_{\nu,\mp\mathbf{q}} - \omega_{S(\mathbf{Q})} - i\eta - i\eta')}}{\omega_{\lambda,\bar{\mathbf{k}}} \pm \omega_{\nu,\mp\mathbf{q}} - \omega_{S(\mathbf{Q})} - i\eta - i\eta'} \sqrt{n_\nu(\mp\mathbf{q}) + \frac{1}{2} \pm \frac{1}{2}}\, \delta_{\mathbf{Q}+\mathbf{q},-\bar{\mathbf{k}}} \\
&\times \sum_{S'} \left[\frac{\mathcal{G}_{S'\nu}(-\mathbf{q}) \mathcal{M}_{S'(-\mathbf{q})S(\mathbf{Q}),\lambda\bar{\mathbf{k}}}}{\omega_{S'(-\mathbf{q})} + \omega_{\lambda,\bar{\mathbf{k}}} - \omega_{S(\mathbf{Q})} - i\eta'} + \frac{\mathcal{G}_{S'S\nu}(\mathbf{Q},\mathbf{q}) \mathcal{M}_{S'(\mathbf{Q}+\mathbf{q}),\lambda\bar{\mathbf{k}}}}{\omega_{S'(\mathbf{Q}+\mathbf{q})} \pm \omega_{\nu,\mp\mathbf{q}} - \omega_{S(\mathbf{Q})} - i\eta'} \right].
\end{aligned} \tag{3.42}$$

3.4 Transition Probability and Rate

The transition probability is defined as

$$P_{i\to f}(t) = \left| c^{(1)}_{i\to f}(t) + c^{(2)}_{i\to f}(t) + \cdots \right|^2. \tag{3.43}$$

The first-order coefficient $c^{(1)}$ vanishes for the $i \to f$ transition we consider, which is momentum-forbidden at first order, and higher-order terms beyond second order are neglected. Thus, the probability for photon emission due to phonon-mediated exciton recombination is obtained from Eq. (3.42) as

$$\begin{aligned} P_{i\to f_\pm}(t) = \frac{1}{\hbar^4} \lim_{\eta,\eta'\to 0^+} & \frac{e^{2t(\eta+\eta')}}{(\omega_{\lambda,\bar{\mathbf{k}}} \pm \omega_{\nu,\mp\mathbf{q}} - \omega_{S(\mathbf{Q})})^2 + (\eta+\eta')^2} \left(n_\nu(\mp\mathbf{q}) + \frac{1}{2} \pm \frac{1}{2} \right) \\ & \times \left| \sum_{S'} \left[\frac{\mathcal{G}_{S'\nu}(-\mathbf{q}) \mathcal{M}_{S'(-\mathbf{q})S(\mathbf{Q}),\lambda\bar{\mathbf{k}}}}{\omega_{S'(-\mathbf{q})} + \omega_{\lambda,\bar{\mathbf{k}}} - \omega_{S(\mathbf{Q})} - i\eta'} + \frac{\mathcal{G}_{S'S\nu}(\mathbf{Q},\mathbf{q}) \mathcal{M}_{S'(\mathbf{Q}+\mathbf{q}),\lambda\bar{\mathbf{k}}}}{\omega_{S'(\mathbf{Q}+\mathbf{q})} \pm \omega_{\nu,\mp\mathbf{q}} - \omega_{S(\mathbf{Q})} - i\eta'} \right] \delta_{\mathbf{Q}+\mathbf{q},-\bar{\mathbf{k}}} \right|^2. \end{aligned} \tag{3.44}$$

The radiative rate for a fixed initial state (exciton $S(\mathbf{Q})$) is obtained by summing over all possible final states ($\sum_{\lambda,\bar{\mathbf{k}},\mathbf{q},\nu,\pm}$) and taking the time derivative of the transition probability:

$$\begin{aligned} \gamma_{S(\mathbf{Q})} &= \sum_{\lambda,\bar{\mathbf{k}},\mathbf{q},\nu,\pm} \frac{d}{dt} P_{i\to f_\pm}(t) \\ &= \sum_{\lambda,\bar{\mathbf{k}},\mathbf{q},\nu,\pm} \frac{1}{\hbar^4} \lim_{\eta,\eta'\to 0^+} \frac{2(\eta+\eta')e^{2t(\eta+\eta')}}{(\omega_{\lambda,\bar{\mathbf{k}}} \pm \omega_{\nu,\mp\mathbf{q}} - \omega_{S(\mathbf{Q})})^2 + (\eta+\eta')^2} \left(n_\nu(\mp\mathbf{q}) + \frac{1}{2} \pm \frac{1}{2} \right) \\ &\quad \times \left| \sum_{S'} \left[\frac{\mathcal{G}_{S'\nu}(-\mathbf{q}) \mathcal{M}_{S'(-\mathbf{q})S(\mathbf{Q}),\lambda\bar{\mathbf{k}}}}{\omega_{S'(-\mathbf{q})} + \omega_{\lambda,\bar{\mathbf{k}}} - \omega_{S(\mathbf{Q})} - i\eta'} + \frac{\mathcal{G}_{S'S\nu}(\mathbf{Q},\mathbf{q}) \mathcal{M}_{S'(\mathbf{Q}+\mathbf{q}),\lambda\bar{\mathbf{k}}}}{\omega_{S'(\mathbf{Q}+\mathbf{q})} \pm \omega_{\nu,\mp\mathbf{q}} - \omega_{S(\mathbf{Q})} - i\eta'} \right] \delta_{\mathbf{Q}+\mathbf{q},-\bar{\mathbf{k}}} \right|^2. \end{aligned} \tag{3.45}$$

By defining $\eta'' = \eta + \eta'$, we have

$$\lim_{\eta''\to 0^+} \frac{2\eta'' e^{2t\eta''}}{(\omega_{\lambda,\bar{\mathbf{k}}} \pm \omega_{\nu,\mp\mathbf{q}} - \omega_{S(\mathbf{Q})})^2 + (\eta'')^2} = 2\pi\delta(\omega_{\lambda,\bar{\mathbf{k}}} \pm \omega_{\nu,\mp\mathbf{q}} - \omega_{S(\mathbf{Q})}), \tag{3.46}$$

and therefore the phonon-assisted radiative rate becomes

$$\gamma_{S(\mathbf{Q})} = \frac{2\pi}{\hbar^4} \sum_{\lambda,\bar{\mathbf{k}},\mathbf{q},\nu,\pm} \left(n_\nu(\mp\mathbf{q}) + \frac{1}{2} \pm \frac{1}{2} \right) \delta(\omega_{\lambda,\bar{\mathbf{k}}} \pm \omega_{\nu,\mp\mathbf{q}} - \omega_{S(\mathbf{Q})})$$

$$\times \lim_{\eta\to 0^+} \left| \sum_{S'} \left[\frac{\mathcal{G}_{S'\nu}(-\mathbf{q})\mathcal{M}_{S'(-\mathbf{q})S(\mathbf{Q}),\lambda\bar{\mathbf{k}}}}{\omega_{S'(-\mathbf{q})} + \omega_{\lambda,\bar{\mathbf{k}}} - \omega_{S(\mathbf{Q})} - i\eta} + \frac{\mathcal{G}_{S'S\nu}(\mathbf{Q},\mathbf{q})\mathcal{M}_{S'(\mathbf{Q}+\mathbf{q}),\lambda\bar{\mathbf{k}}}}{\omega_{S'(\mathbf{Q}+\mathbf{q})} \pm \omega_{\nu,\mp\mathbf{q}} - \omega_{S(\mathbf{Q})} - i\eta} \right] \delta_{\mathbf{Q}+\mathbf{q},-\bar{\mathbf{k}}} \right|^2 . \tag{3.47}$$

Here, $\gamma_{S(\mathbf{Q})}$ is the state-resolved phonon-assisted radiative rate. If a spin-unpolarized calculation is performed, an additional spin degeneracy factor of 2 should be applied. The expression of interband and intraband exciton-photon matrix elements $\mathcal{M}$, within the dipole approximation, is provided as

$$\begin{aligned} \mathcal{M}_{S'(\mathbf{Q}')S(\mathbf{Q}),\lambda\bar{\mathbf{k}}} = i\hbar\sqrt{\frac{e^2}{2\hbar\omega_{\lambda\bar{\mathbf{k}}}\epsilon_0 V}}(\omega_{S(\mathbf{Q})} - \omega_{S'(\mathbf{Q}')})\mathbf{e}^*_{\lambda\bar{\mathbf{k}}} \\ \cdot \langle S'(\mathbf{Q}')|\hat{\mathbf{r}}|S(\mathbf{Q})\rangle; \end{aligned}$$

$$\mathcal{M}_{S(\mathbf{Q}),\lambda\bar{\mathbf{k}}} = i\hbar\sqrt{\frac{e^2}{2\hbar\omega_{\lambda\bar{\mathbf{k}}}\epsilon_0 V}}\omega_{S(\mathbf{Q})}\mathbf{e}^*_{\lambda,\bar{\mathbf{k}}} \cdot \langle G|\,\hat{\mathbf{r}}\,|S(\mathbf{Q})\rangle\,. \tag{3.48}$$

In the following discussion, we focus on the phonon-assisted radiative process, specifically, intraband exciton-phonon coupling, which is described by the second term in Eq. (3.47) and depicted in Fig. 3.1(a). The interband exciton-photon coupling, which is described by the first term in Eq. (3.47) and depicted in Fig. 3.1(b), corresponding to transitions between the valence and conduction bands induced by phonon excitation, is typically negligible in semiconductors, because of the large energy gap between these bands compared to phonon energies.

3.5 Phonon-Assisted Radiative Rate in Anisotropic Medium

We now consider the propagation of light in anisotropic optical media [46, 134]. The relative dielectric tensor $\overleftrightarrow{\epsilon}$, expressed in the principal frame defined by the Cartesian axes (x, y, z), takes the form:

$$\overleftrightarrow{\epsilon} = \begin{pmatrix} \epsilon_{xx} & 0 & 0 \\ 0 & \epsilon_{yy} & 0 \\ 0 & 0 & \epsilon_{zz} \end{pmatrix}, \tag{3.49}$$

where ϵ_{ii} $(i = x, y, z)$ denotes the dimensionless relative dielectric constant along each principal axis.

The photon dispersion relation is given by $\omega_{\lambda\bar{\mathbf{k}}} = |\bar{\mathbf{k}}|v = |\bar{\mathbf{k}}|c/n_\lambda$, where $n_\lambda = n_1, n_2$ is the refractive index of the medium, and $\lambda = 1, 2$ labels the photon polarization modes.

Starting from Maxwell's equations,

$$\nabla \times (\nabla \times \mathbf{E}) = \nabla(\nabla \cdot \mathbf{E}) - \nabla^2 \mathbf{E} = -\epsilon_0 \mu_0 \overleftrightarrow{\epsilon} \frac{\partial^2 \mathbf{E}}{\partial t^2}, \tag{3.50}$$

we insert a plane-wave ansatz $\mathbf{E} = \mathbf{E}_0 e^{-i(\omega t - \bar{\mathbf{k}} \cdot \mathbf{r})}$, with the photon wavevector expressed as $\bar{\mathbf{k}} = |\bar{\mathbf{k}}| n_\lambda \mathbf{s} = |\bar{\mathbf{k}}| n_\lambda (s_x \hat{\mathbf{x}} + s_y \hat{\mathbf{y}} + s_z \hat{\mathbf{z}})$, where $\mathbf{s}$ is a unit vector in the propagation direction.

Substituting into Eq. (3.50), we obtain the Fresnel equation for anisotropic media:

$$\frac{s_x^2}{n_\lambda^2 - \epsilon_{xx}} + \frac{s_y^2}{n_\lambda^2 - \epsilon_{yy}} + \frac{s_z^2}{n_\lambda^2 - \epsilon_{zz}} = \frac{1}{n_\lambda^2}. \tag{3.51}$$

The corresponding electric field eigenvector for each mode is then given by:

$$\mathbf{E}_\lambda = \begin{pmatrix} s_x \left(n_\lambda^2 - \epsilon_{xx}\right)^{-1} \\ s_y \left(n_\lambda^2 - \epsilon_{yy}\right)^{-1} \\ s_z \left(n_\lambda^2 - \epsilon_{zz}\right)^{-1} \end{pmatrix}. \tag{3.52}$$

We now consider a special case where $\epsilon_{xx} = \epsilon_{yy} = \epsilon_\parallel$ and $\epsilon_{zz} = \epsilon_\perp$, which is sufficient for our discussion of dimensional dependence. The direction of light propagation is represented as

$$\mathbf{s} = \sin\theta \cos\phi \, \hat{\mathbf{x}} + \sin\theta \sin\phi \, \hat{\mathbf{y}} + \cos\theta \, \hat{\mathbf{z}}.$$

Under this symmetry, the Fresnel equation simplifies to

$$\begin{aligned}(n_\lambda^2 - \epsilon_\parallel)^2 (n_\lambda^2 - \epsilon_\perp) = \sin^2\theta \, n_\lambda^2 (n_\lambda^2 - \epsilon_\parallel)(n_\lambda^2 - \epsilon_\perp) \\ + \cos^2\theta \, n_\lambda^2 (n_\lambda^2 - \epsilon_\parallel)^2.\end{aligned} \tag{3.53}$$

Applying the orthonormality condition for the eigenmodes $\mathbf{e}_{\lambda\bar{\mathbf{k}}}$, such that

$$\mathbf{e}_{\lambda\bar{\mathbf{k}}}^\dagger \overleftrightarrow{\epsilon} \mathbf{e}_{\lambda'\bar{\mathbf{k}}} = \delta_{\lambda\lambda'},$$

we obtain the following eigenmode solutions:

$$\mathbf{e}_{1,\bar{\mathbf{k}}} = \begin{pmatrix} -\epsilon_{\parallel}^{-1/2} \sin\phi \\ \epsilon_{\parallel}^{-1/2} \cos\phi \\ 0 \end{pmatrix}, \quad \mathbf{e}_{2,\bar{\mathbf{k}}} = \begin{pmatrix} -\epsilon_{\parallel}^{-1/2} \cos\phi \cos\bar{\theta} \\ -\epsilon_{\parallel}^{-1/2} \sin\phi \cos\bar{\theta} \\ \epsilon_{\perp}^{-1/2} \sin\bar{\theta} \end{pmatrix}, \tag{3.54}$$

where $\cos\bar{\theta}$ and $\sin\bar{\theta}$ are defined as

$$\begin{aligned} \cos\bar{\theta} &= \frac{\cos\theta\, \epsilon_{\perp}^{1/2}}{\sqrt{\epsilon_{\parallel} \sin^2\theta + \epsilon_{\perp} \cos^2\theta}}, \\ \sin\bar{\theta} &= \frac{\sin\theta\, \epsilon_{\parallel}^{1/2}}{\sqrt{\epsilon_{\parallel} \sin^2\theta + \epsilon_{\perp} \cos^2\theta}}. \end{aligned} \tag{3.55}$$

In the isotropic limit where $\epsilon_{\parallel} = \epsilon_{\perp}$, these reduce to the standard isotropic eigenmodes [18]. To avoid confusion between the refractive index and the Bose-Einstein occupation number, we define the inverse squared refractive index as $\Theta_{\lambda} = 1/n_{\lambda}^2$, yielding:

$$\Theta_{+} = \frac{1}{\epsilon_{\parallel}}, \quad \Theta_{-} = \frac{\sin^2\theta}{\epsilon_{\perp}} + \frac{\cos^2\theta}{\epsilon_{\parallel}}. \tag{3.56}$$

The photon energy dispersion relation is thus written as $\omega_{\lambda\bar{\mathbf{k}}} = c|\bar{\mathbf{k}}|\sqrt{\Theta_{\lambda}}$. The phonon-assisted radiative rate takes the form:

$$\begin{aligned} \gamma_{S(\mathbf{Q})} = \frac{2\pi}{\hbar^4} \sum_{\lambda,\mathbf{q},\nu,\pm} \left(n_{\nu}(\mp\mathbf{q}) + \frac{1}{2} \pm \frac{1}{2} \right) \frac{V}{(2\pi)^3} \int d\bar{\mathbf{k}} \left| \sum_{S'} \frac{\mathcal{G}_{S'S\nu}(\mathbf{Q},\mathbf{q}) \mathcal{M}_{S'(\mathbf{Q}+\mathbf{q}),\lambda\bar{\mathbf{k}}}}{\omega_{S'(\mathbf{Q}+\mathbf{q})} \pm \omega_{\nu,\mp\mathbf{q}} - \omega_{S(\mathbf{Q})} - i\eta} \delta_{\mathbf{Q}+\mathbf{q},-\bar{\mathbf{k}}} \right|^2 \\ \times \delta(\omega_{\lambda,\bar{\mathbf{k}}} \pm \omega_{\nu,\mp\mathbf{q}} - \omega_{S(\mathbf{Q})}). \end{aligned} \tag{3.57}$$

Changing integration variables and inserting the dipole matrix element $\boldsymbol{\mu}_S$, we obtain:

$$\begin{aligned} \gamma_{S(\mathbf{Q})} &= \sum_{\lambda,\mathbf{q},\nu,\pm} \left(n_{\nu}(\mp\mathbf{q}) + \frac{1}{2} \pm \frac{1}{2} \right) \frac{e^2}{8\pi^2 \epsilon_0 \hbar^3 c^3} \iint d\phi\, d\theta\, \sin\theta\, \frac{1}{\Theta_{\lambda}^{3/2}} \\ &\quad \times \int d\omega_{\lambda\bar{\mathbf{k}}}\, \omega_{\lambda\bar{\mathbf{k}}} \left| \sum_{S'} \omega_{S'(\mathbf{Q}+\mathbf{q})} \frac{\mathcal{G}_{S'S\nu}(\mathbf{Q},\mathbf{q})\, \mathbf{e}_{\lambda\bar{\mathbf{k}}} \cdot \boldsymbol{\mu}_{S'(\mathbf{Q}+\mathbf{q})}}{\omega_{S'(\mathbf{Q}+\mathbf{q})} \pm \omega_{\nu,\mp\mathbf{q}} - \omega_{S(\mathbf{Q})} - i\eta} \delta_{\mathbf{Q}+\mathbf{q},-\bar{\mathbf{k}}} \right|^2 \\ &= \sum_{\lambda,\mathbf{q},\nu,\pm} \left(n_{\nu}(\mp\mathbf{q}) + \frac{1}{2} \pm \frac{1}{2} \right) \frac{e^2}{8\pi^2 \epsilon_0 \hbar^3 c^3} (\omega_{S(\mathbf{Q})} \mp \omega_{\nu,\mp\mathbf{q}}) \end{aligned}$$

$$\times \iint \mathrm{d}\phi\, \mathrm{d}\theta\, \sin\theta\, \frac{1}{\Theta_\lambda^{3/2}} \left| \sum_{S'} \omega_{S'(\mathbf{0})} \frac{\mathcal{G}_{S'S\nu}(\mathbf{Q},\mathbf{q})\, \mathbf{e}_{\lambda\mathbf{0}} \cdot \boldsymbol{\mu}_{S'(\mathbf{0})}}{\omega_{S'(\mathbf{0})} \pm \omega_{\nu,\mp\mathbf{q}} - \omega_{S(\mathbf{Q})} - i\eta} \delta_{\mathbf{Q},-\mathbf{q}} \right|^2 . \tag{3.58}$$

We define the angular integral

$$\mathrm{I}_{S\nu\pm}(\mathbf{Q},\mathbf{q}) = \frac{1}{\hbar^2 c^2} \sum_\lambda \iint \mathrm{d}\phi\, \mathrm{d}\theta\, \sin\theta\, \frac{1}{\Theta_\lambda^{3/2}} \left| \sum_{S'} \omega_{S'(\mathbf{0})} \frac{\mathcal{G}_{S'S\nu}(\mathbf{Q},\mathbf{q})\, \mathbf{e}_{\lambda\mathbf{0}} \cdot \boldsymbol{\mu}_{S'(\mathbf{0})}}{\omega_{S'(\mathbf{0})} \pm \omega_{\nu,\mp\mathbf{q}} - \omega_{S(\mathbf{Q})} - i\eta} \delta_{\mathbf{Q},-\mathbf{q}} \right|^2 . \tag{3.59}$$

Finally, we define the dimensionless vector $\boldsymbol{\Lambda}$ as

$$\boldsymbol{\Lambda}_{S'S\nu\pm}(\mathbf{Q},\mathbf{q}) = \frac{1}{\hbar c}\, \omega_{S'(\mathbf{0})} \frac{\boldsymbol{\mu}_{S'(\mathbf{0})} \mathcal{G}_{S'S\nu}(\mathbf{Q},\mathbf{q})}{\omega_{S'(\mathbf{0})} - \omega_{S(\mathbf{Q})} \pm \omega_{\nu,\mp\mathbf{q}} - i\eta} \delta_{\mathbf{Q},-\mathbf{q}'} \tag{3.60}$$

so that

$$\mathrm{I}_{S\nu\pm}(\mathbf{Q},\mathbf{q}) = \sum_\lambda \iint \mathrm{d}\phi\, \mathrm{d}\theta\, \sin\theta\, \frac{1}{\Theta_\lambda^{3/2}} \left| \sum_{S'} \mathbf{e}_{\lambda\mathbf{0}} \cdot \boldsymbol{\Lambda}_{S'S\nu\pm}(\mathbf{Q},\mathbf{q}) \right|^2 . \tag{3.61}$$

Let $\cos\theta = z$, and for brevity, we omit the universal subscript ${}_{S\nu\pm}(\mathbf{Q},\mathbf{q})$ in $\boldsymbol{\Lambda}_{S\nu\pm}(\mathbf{Q},\mathbf{q}) = \sum_{S'} \boldsymbol{\Lambda}_{S'S\nu\pm}(\mathbf{Q},\mathbf{q})$ in the following derivation. Odd functions such as $\sin(\cdots)$ and $\sin(\cdots)\cos(\cdots)$ cancel upon angular integration. The integral $\mathrm{I}_{S\nu\pm}(\mathbf{Q},\mathbf{q})$ becomes:

$$\begin{aligned}
\mathrm{I}_{S\nu\pm}(\mathbf{Q},\mathbf{q}) &= \int \mathrm{d}\phi \int \mathrm{d}(\cos\theta) \qquad (3.62)\\
&\left\{ \begin{array}{r} \epsilon_\parallel^{3/2} \left| -\boldsymbol{\Lambda}_x \epsilon_\parallel^{-1/2} \sin\phi + \boldsymbol{\Lambda}_y \epsilon_\parallel^{-1/2} \cos\phi \right|^2 \\ + \left(\frac{\sin^2\theta}{\epsilon_\perp} + \frac{\cos^2\theta}{\epsilon_\parallel} \right)^{-3/2} \left| -\boldsymbol{\Lambda}_x \epsilon_\parallel^{-1/2} \cos\bar{\theta}\cos\phi - \boldsymbol{\Lambda}_y \epsilon_\parallel^{-1/2} \cos\bar{\theta}\sin\phi + \boldsymbol{\Lambda}_z \epsilon_\perp^{-1/2} \sin\bar{\theta} \right|^2 \end{array} \right\} \\
&= 2\pi \int_{-1}^{1} \mathrm{d}z \left[\frac{1}{2}(|\boldsymbol{\Lambda}_x|^2 + |\boldsymbol{\Lambda}_y|^2) \epsilon_\parallel^{1/2} \right. \\
&\quad \left. + \frac{(\epsilon_\parallel \epsilon_\perp)^{3/2}}{\left[(\epsilon_\perp - \epsilon_\parallel) z^2 + \epsilon_\parallel\right]^{3/2}} \left(\frac{1}{2}(|\boldsymbol{\Lambda}_x|^2 + |\boldsymbol{\Lambda}_y|^2) \frac{\cos^2\bar{\theta}}{\epsilon_\parallel} + |\boldsymbol{\Lambda}_z|^2 \frac{\sin^2\bar{\theta}}{\epsilon_\perp} \right) \right] \\
&= \frac{8\pi}{3} \left[(|\boldsymbol{\Lambda}_x|^2 + |\boldsymbol{\Lambda}_y|^2) \frac{\epsilon_\parallel^{-1/2} \epsilon_\perp + 3\epsilon_\parallel^{1/2}}{4} + |\boldsymbol{\Lambda}_z|^2 \epsilon_\parallel^{1/2} \right], \qquad (3.63)
\end{aligned}$$

where

$$\cos^2\bar{\theta} = \frac{\epsilon_\perp z^2}{(\epsilon_\perp - \epsilon_\parallel) z^2 + \epsilon_\parallel}, \quad \sin^2\bar{\theta} = \frac{\epsilon_\parallel (1 - z^2)}{(\epsilon_\perp - \epsilon_\parallel) z^2 + \epsilon_\parallel}.$$

Note that although the macroscopic dielectric environment is assumed in-plane isotropic ($\epsilon_{xx} = \epsilon_{yy} = \epsilon_{\parallel}$), the microscopic in-plane components of the effective dipole amplitude, $\boldsymbol{\Lambda}_x$ and $\boldsymbol{\Lambda}_y$, may still differ.

To obtain the final result, we use the following integral identities for $u > 0$:

$$\int_{-1}^{1} \frac{dz}{(z^2+u)^{3/2}} = \frac{2}{u(1+u)^{1/2}}, \quad \int_{-1}^{1} \frac{dz}{(z^2+u)^{5/2}} = \frac{2}{3u^2(1+u)^{3/2}}.$$

We now define the dimensionless effective amplitude and an effective tensor $\overleftrightarrow{\mathcal{E}}$ to simplify Eq. (3.62):

$$\begin{aligned}\boldsymbol{\Lambda}_{S\nu\pm}(\mathbf{Q},\mathbf{q}) &= \sum_{S'} \boldsymbol{\Lambda}_{S'S\nu\pm}(\mathbf{Q},\mathbf{q}) \\ &= \frac{1}{\hbar c}\sum_{S'} \omega_{S'(\mathbf{0})} \frac{\boldsymbol{\mu}_{S'(\mathbf{0})}\mathcal{G}_{S'S\nu}(\mathbf{Q},\mathbf{q})}{\omega_{S'(\mathbf{0})} - \omega_{S(\mathbf{Q})} \pm \omega_{\nu,\mp\mathbf{q}} - i\eta}\delta_{\mathbf{Q},-\mathbf{q}'} \end{aligned} \tag{3.64}$$

$$\overleftrightarrow{\mathcal{E}} = \begin{pmatrix} \frac{\epsilon_{\parallel}^{-1/2}\epsilon_{\perp}+3\epsilon_{\parallel}^{1/2}}{4} & 0 & 0 \\ 0 & \frac{\epsilon_{\parallel}^{-1/2}\epsilon_{\perp}+3\epsilon_{\parallel}^{1/2}}{4} & 0 \\ 0 & 0 & \epsilon_{\parallel}^{1/2} \end{pmatrix}. \tag{3.65}$$

The effective tensor $\overleftrightarrow{\mathcal{E}}$ is positive semidefinite. Thus, Eq. (3.62) can be written compactly as

$$I_{S\nu\pm}(\mathbf{Q},\mathbf{q}) = \frac{8\pi}{3}\boldsymbol{\Lambda}^{\dagger}_{S\nu\pm}(\mathbf{Q},\mathbf{q})\overleftrightarrow{\mathcal{E}}\boldsymbol{\Lambda}_{S\nu\pm}(\mathbf{Q},\mathbf{q}) = \frac{8\pi}{3}\left|\overleftrightarrow{\mathcal{E}}^{1/2}\boldsymbol{\Lambda}_{S\nu\pm}(\mathbf{Q},\mathbf{q})\right|^2. \tag{3.66}$$

The exciton-state-resolved phonon-assisted radiative rate becomes

$$\begin{aligned}\gamma_{S(\mathbf{Q})} &= \frac{e^2}{8\pi^2\epsilon_0\hbar c}\sum_{\mathbf{q},\nu,\pm}\left(n_\nu(\mp\mathbf{q}) + \frac{1}{2} \pm \frac{1}{2}\right)(\omega_{S(\mathbf{Q})} \mp \omega_{\nu,\mp\mathbf{q}})I_{S\nu\pm}(\mathbf{Q},\mathbf{q}) \\ &= \frac{e^2}{3\pi\epsilon_0\hbar c}\sum_{\mathbf{q},\nu,\pm}\left(n_\nu(\mp\mathbf{q}) + \frac{1}{2} \pm \frac{1}{2}\right)(\omega_{S(\mathbf{Q})} \mp \omega_{\nu,\mp\mathbf{q}})\left|\overleftrightarrow{\mathcal{E}}^{1/2}\boldsymbol{\Lambda}_{S\nu\pm}(\mathbf{Q},\mathbf{q})\right|^2. \end{aligned} \tag{3.67}$$

Using the dimensionless fine-structure constant $\alpha = \frac{e^2}{4\pi\epsilon_0\hbar c}$, the final expression is

$$\gamma_{S(\mathbf{Q})} = \frac{4}{3}\alpha \sum_{\mathbf{q},\nu,\pm} \left(\omega_{S(\mathbf{Q})} \mp \omega_{\nu,\mp\mathbf{q}}\right) \left| \overset{\leftrightarrow 1/2}{\mathcal{E}} \boldsymbol{\Lambda}_{S\nu\pm}(\mathbf{Q},\mathbf{q}) \right|^2 \left(n_{\nu,\mp\mathbf{q}} + \frac{1}{2} \pm \frac{1}{2}\right). \tag{3.68}$$

The observable, finite-temperature phonon-assisted radiative rate γ is computed as a thermal average [125] of $\gamma_{S(\mathbf{Q})}$ in the dilute limit:

$$\gamma = \langle \gamma_{S(\mathbf{Q})} \rangle = \frac{1}{\mathcal{Z}} \sum_{S,\mathbf{Q}} e^{-\beta\hbar\omega_{S(\mathbf{Q})}} \gamma_{S(\mathbf{Q})}, \tag{3.69}$$

with the partition function

$$\mathcal{Z} = \sum_{S,\mathbf{Q}} e^{-\beta\hbar\omega_{S(\mathbf{Q})}}. \tag{3.70}$$

The finite-temperature phonon-assisted radiative lifetime τ is defined as the inverse of the phonon-assisted radiative rate.

3.6 Real-Time Exciton Dynamics and Master Equation

To study the exciton dynamics and thermalization, we derived the quantum master equation in the Lindblad form [131] for exciton-phonon dynamics. The scattering Hamiltonian for exciton-phonon interaction can be symmetrically expressed [92, 91] as

$$\hat{\mathcal{H}}^s = \sum_{12\nu\mathbf{q}} \left(\mathcal{G}_{12}^{\mathbf{q}\nu} \hat{c}_1^\dagger \hat{c}_2 \hat{b}_{\nu\mathbf{q}}^\dagger + \mathcal{G}_{21}^{\mathbf{q}\nu,*} \hat{c}_2^\dagger \hat{c}_1 \hat{b}_{\nu\mathbf{q}} \right) = \sum_{12\nu\mathbf{q}} \mathcal{G}_{12}^{\mathbf{q}\nu} \hat{c}_1^\dagger \hat{c}_2 \hat{b}_{\nu\mathbf{q}}^\dagger + \text{H.c.}, \tag{3.71}$$

where the exciton-phonon matrix element $\mathcal{G}_{S'S\nu}(\mathbf{Q},\mathbf{q})$ is denoted by $\mathcal{G}_{12}^{\mathbf{q}\nu}$, with $1 \coloneqq S'(\mathbf{Q}+\mathbf{q})$ and $2 \coloneqq S(\mathbf{Q})$.

The time evolution of the density matrix due to this scattering process follows the Lindblad-type equation [92, 91]:

$$\frac{d\hat{\boldsymbol{\rho}}}{dt} = \hat{\mathcal{A}}\hat{\boldsymbol{\rho}}\hat{\mathcal{A}}^\dagger - \frac{1}{2}\left\{\hat{\mathcal{A}}^\dagger\hat{\mathcal{A}}, \hat{\boldsymbol{\rho}}\right\},$$

where the operator $\hat{\mathcal{A}}$ is defined by

$$\hat{\mathcal{A}} = \frac{1}{\hbar}\left(\frac{1}{2\pi\bar{t}^2}\right)^{1/4} \int dt' \, e^{-\frac{\hat{\mathcal{H}}_0 t'}{i\hbar}} \hat{\mathcal{H}}^s e^{\frac{\hat{\mathcal{H}}_0 t'}{i\hbar}} e^{-\frac{t'^2}{4\bar{t}^2}}, \tag{3.72}$$

with $\bar{t}$ representing the scattering time scale.

To obtain the time evolution of the density matrix elements $\boldsymbol{\rho}_{12} = \langle \hat{c}_2^\dagger \hat{c}_1 \rangle$, we compute:

$$\begin{aligned}\frac{d\boldsymbol{\rho}_{12}}{dt} &= \mathrm{Tr}\left(\hat{c}_2^\dagger \hat{c}_1 \frac{d\hat{\boldsymbol{\rho}}}{dt}\right) \\ &= \frac{1}{2}\mathrm{Tr}\left([\hat{\mathcal{A}}^\dagger, \hat{c}_2^\dagger \hat{c}_1]\hat{\mathcal{A}}\hat{\boldsymbol{\rho}} + \hat{\boldsymbol{\rho}}\hat{\mathcal{A}}^\dagger[\hat{c}_2^\dagger \hat{c}_1, \hat{\mathcal{A}}]\right) = \frac{1}{2}\mathrm{Tr}\left([\hat{\mathcal{A}}^\dagger, \hat{c}_2^\dagger \hat{c}_1]\hat{\mathcal{A}}\hat{\boldsymbol{\rho}}\right) + \mathrm{H.c.}\end{aligned} \tag{3.73}$$

We now insert Eqs. (3.71) and (3.72) into Eq. (3.73) and define:

$$\begin{aligned}\hat{\mathcal{A}} &= \sum_{\mathbf{q}\nu}\left(\hat{\mathcal{D}}^{\mathbf{q}\nu+}\hat{b}_{\mathbf{q}\nu}^\dagger + \hat{\mathcal{D}}^{\mathbf{q}\nu-}\hat{b}_{\mathbf{q}\nu}\right), \\ \hat{\mathcal{D}}^{\mathbf{q}\nu\pm} &= \sum_{12}\mathcal{D}_{12}^{\mathbf{q}\nu\pm}\hat{c}_1^\dagger \hat{c}_2, \\ \mathcal{D}_{12}^{\mathbf{q}\nu\pm} &= \frac{1}{\hbar}\left(\frac{1}{2\pi\bar{t}^2}\right)^{1/4}\mathcal{G}_{12}^{\mathbf{q}\nu}\int dt'\, e^{-\frac{(\epsilon_1-\epsilon_2\pm\omega_{\mathbf{q}\nu})t'}{i\hbar}}e^{-\frac{t'^2}{4\bar{t}^2}} \\ &= \sqrt{\frac{2\pi}{\hbar^2}}\mathcal{G}_{12}^{\mathbf{q}\nu}\left(\frac{1}{2\pi\bar{\epsilon}^2}\right)^{1/4}e^{-\left(\frac{\epsilon_1-\epsilon_2\pm\omega_{\mathbf{q}\nu}}{2\bar{\epsilon}}\right)^2},\end{aligned} \tag{3.74}$$

where the energy broadening is defined as $\bar{\epsilon} = \hbar/(2\bar{t}) \to 0^+$.

The commutators become:

$$\left[\hat{\mathcal{D}}^{\mathbf{q}\nu\pm,\dagger}, \hat{c}_2^\dagger \hat{c}_1\right] = \sum_3\left(\mathcal{D}_{32}^{\mathbf{q}\nu\mp}\hat{c}_3^\dagger \hat{c}_1 - \mathcal{D}_{13}^{\mathbf{q}\nu\mp}\hat{c}_2^\dagger \hat{c}_3\right). \tag{3.75}$$

We assume the total density matrix is: $\hat{\boldsymbol{\rho}} = \hat{\boldsymbol{\rho}}^S \otimes \hat{\boldsymbol{\rho}}^B$, where $\hat{\boldsymbol{\rho}}^S$ describes excitons (system) and $\hat{\boldsymbol{\rho}}^B$ describes phonons (bath). For phonons:

$$\begin{aligned}&\mathrm{Tr}_B(\hat{b}_{\mathbf{q}\nu}\hat{b}_{\mathbf{q}'\nu'}\hat{\boldsymbol{\rho}}^B) = \mathrm{Tr}_B(\hat{b}_{\mathbf{q}\nu}^\dagger \hat{b}_{\mathbf{q}'\nu'}^\dagger \hat{\boldsymbol{\rho}}^B) = 0, \\ &\mathrm{Tr}_B(\hat{b}_{\mathbf{q}\nu}\hat{b}_{\mathbf{q}'\nu'}^\dagger \hat{\boldsymbol{\rho}}^B) = \delta_{\mathbf{q}\mathbf{q}'}\delta_{\nu\nu'}n_{\mathbf{q}\nu}, \\ &\mathrm{Tr}_B(\hat{b}_{\mathbf{q}\nu}^\dagger \hat{b}_{\mathbf{q}'\nu'}\hat{\boldsymbol{\rho}}^B) = \delta_{\mathbf{q}\mathbf{q}'}\delta_{\nu\nu'}(n_{\mathbf{q}\nu}+1).\end{aligned} \tag{3.76}$$

Substituting Eqs. (3.75) and the above into Eq. (3.73), and tracing over the phonon bath, we obtain:

$$\frac{d\boldsymbol{\rho}_{12}^S}{dt} = \frac{1}{2}\sum_{345\mathbf{q}\nu\pm}\left(\mathcal{D}_{32}^{\mathbf{q}\nu\mp}h_{3145} - \mathcal{D}_{13}^{\mathbf{q}\nu\mp}h_{2345}\right)\mathcal{D}_{45}^{\mathbf{q}\nu\pm}n_{\mathbf{q}\nu}^\pm + \mathrm{H.c.}, \tag{3.77}$$

where the two-particle correlation function is

$$h_{1234} = \mathrm{Tr}\left(\hat{c}_1^\dagger \hat{c}_2 \hat{c}_3^\dagger \hat{c}_4 \hat{\rho}^S\right). \tag{3.78}$$

To close the system, we apply the mean-field approximation, neglecting the disconnected exchange terms:

$$h_{1234} \approx \delta_{23}\rho^S_{41} + \rho^S_{41}\rho^S_{23} = (\mathbb{1} + \rho^S)_{23}\rho^S_{41}. \tag{3.79}$$

This yields the final master equation for the exciton density matrix:

$$\frac{d\rho^S_{12}}{dt} = \frac{1}{2}\sum_{345\mathbf{q}\nu\pm}\left((\mathbb{1}+\rho^S)_{14}\mathcal{D}^{\mathbf{q}\nu\pm}_{45}\rho^S_{53}\mathcal{D}^{\mathbf{q}\nu\mp}_{32} - \mathcal{D}^{\mathbf{q}\nu\mp}_{13}(\mathbb{1}+\rho^S)_{34}\mathcal{D}^{\mathbf{q}\nu\pm}_{45}\rho^S_{52}\right)n^{\pm}_{\mathbf{q}\nu} + \mathrm{H.c.}, \tag{3.80}$$

where $n^{\pm}_{\mathbf{q}\nu} = n_{\mathbf{q}\nu} + \frac{1}{2} \pm \frac{1}{2}$ denotes the phonon occupation for emission $(+)$ and absorption $(-)$.

We define:

$$\mathcal{P}_{1234} = \sum_{\mathbf{q}\nu\pm}\mathcal{A}^{\mathbf{q}\nu\pm}_{13}\mathcal{A}^{\mathbf{q}\nu\pm,*}_{24},$$
$$\mathcal{A}^{\mathbf{q}\nu\pm}_{13} = \mathcal{D}^{\mathbf{q}\nu\pm}_{13}\sqrt{n^{\pm}_{\mathbf{q}\nu}}, \quad \mathcal{D}^{\mathbf{q}\nu\pm}_{12} = \sqrt{\frac{2\pi}{\hbar^2}}\mathcal{G}^{\mathbf{q}\nu}_{12}\delta_G^{1/2}\left(\omega_1 - \omega_2 \pm \omega_{\mp\mathbf{q}\nu}\right),$$

where δ_G is a Gaussian-broadened delta function ensuring approximate energy conservation.

Thus, the final compact master equation becomes:

$$\frac{d\rho^S_{12}}{dt} = \frac{1}{2}\sum_{345}\left((\mathbb{1}+\rho^S)_{14}\mathcal{P}_{4253}\rho^S_{53} - (\mathbb{1}+\rho^S)_{34}\mathcal{P}^*_{3415}\rho^S_{52}\right) + \mathrm{H.c.}$$

In the following text, we drop the superscript S in ρ for simplicity.

$$\begin{aligned}\frac{d\rho_{12}}{dt} =& \frac{1}{2}\sum_{345}\left((\mathbb{1}+\rho)_{14}\,\mathcal{P}_{4253}\rho_{53} - (\mathbb{1}+\rho)_{34}\,\mathcal{P}^*_{3415}\rho_{52}\right)\\ &+ \mathrm{H.c.}\,,\end{aligned} \tag{3.81}$$

where the scattering terms are defined as: $\mathcal{P}_{1234} = \sum_{\mathbf{q}\nu\pm}\mathcal{A}^{\mathbf{q}\nu\pm}_{13}\mathcal{A}^{\mathbf{q}\nu\pm,*}_{24}$ with $\mathcal{A}^{\mathbf{q}\nu\pm}_{13} = \mathcal{D}^{\mathbf{q}\nu\pm}_{13}\sqrt{n_{\nu,\mp\mathbf{q}} + \frac{1}{2} \pm \frac{1}{2}}$. The exciton-phonon coupling term $\mathcal{D}^{\mathbf{q}\nu\pm}_{12}$ is expressed

as: $\mathcal{D}_{12}^{\mathbf{q}\nu\pm} = \sqrt{\frac{2\pi}{\hbar^2}}\mathcal{G}_{12}^{\mathbf{q}\nu}\delta_G^{\frac{1}{2}}\left(\omega_1 - \omega_2 \pm \omega_{\mp\mathbf{q}\nu}\right)$, where δ_G represents an energy-conserving Dirac delta function broadened to a Gaussian. Here, the exciton-phonon matrix element $\mathcal{G}_{S'S\nu}(\mathbf{Q},\mathbf{q})$ is denoted for simplicity as $\mathcal{G}_{12}^{\mathbf{q}\nu}$, where the indices are defined as $1 \coloneqq S'(\mathbf{Q}+\mathbf{q})$ and $2 \coloneqq S(\mathbf{Q})$. $\boldsymbol{\rho}$ represents the exciton density matrix. Notably, the primary distinction between the Lindblad equation for the exciton dynamics and that for the electron dynamics[128, 131, 129] lies in the term $\mathbb{1} - \boldsymbol{\rho}$ being replaced by $\mathbb{1} + \boldsymbol{\rho}$. This difference arises due to the distinct (anti)commutation relations governing fermionic and bosonic operators. In this study, we focus on exciton occupation changes due to exciton-phonon scatterings, where the phase coherence information between different exciton states (corresponding to the off-diagonal elements of exciton density matrices) is not important, which will leave for our future studies. Therefore, by applying the diagonal (semiclassical) approximation to exciton density matrices and Lindbladian operators, we obtain the (semiclassical) quantum master equation

$$\frac{\mathrm{d}}{\mathrm{d}t}\mathcal{N}_2 = \sum_1 \Gamma_{21}\mathcal{N}_1\left(1+\mathcal{N}_2\right) - \sum_1 \Gamma_{12}\mathcal{N}_2\left(1+\mathcal{N}_1\right), \tag{3.82}$$

where the scattering rate Γ_{12} describes the transition rate between exciton states $1, 2$. This rate is expressed as

$$\begin{aligned}\Gamma_{12} =& \mathcal{P}_{1122} = \sum_{\mathbf{q}\nu\pm} \mathcal{A}_{12}^{\mathbf{q}\nu\pm}\mathcal{A}_{12}^{\mathbf{q}\nu\pm,*} \\ =& \frac{2\pi}{\hbar^2}\sum_{\mathbf{q}\nu\pm}\left|\mathcal{G}_{12}^{\mathbf{q}\nu}\right|^2\left(n_{\nu,\mp\mathbf{q}} + \frac{1}{2} \pm \frac{1}{2}\right)\delta_G(\omega_1 - \omega_2 \pm \omega_{\mp\mathbf{q}\nu}),\end{aligned} \tag{3.83}$$

which aligns with the transition rate derived from the Fermi's golden rule.

3.7 Results and Discussion

Next, we present the temperature-dependent phonon-assisted radiative lifetime in Fig. 3.2(a). The black curve shows the total radiative lifetime, which consists of both phonon emission (red curve) and phonon absorption (blue curve) contributions. Below 150 K, the total lifetime exhibits a non-monotonic behavior, which can be qualitatively understood using a two-valley model. We approximate the exciton energy landscape with two valleys—valley 1 and valley 2—where valley 1 dominates the radiative process. Neglecting exciton dispersion, we model the radiative rate from valley 1 as $\gamma_1(T) = \tilde{\gamma}_1(n_{ph}+1)$, with $n_{ph} = (e^{\beta\hbar\tilde{\omega}}-1)^{-1}$ representing the Bose-Einstein occupation of a single effective phonon

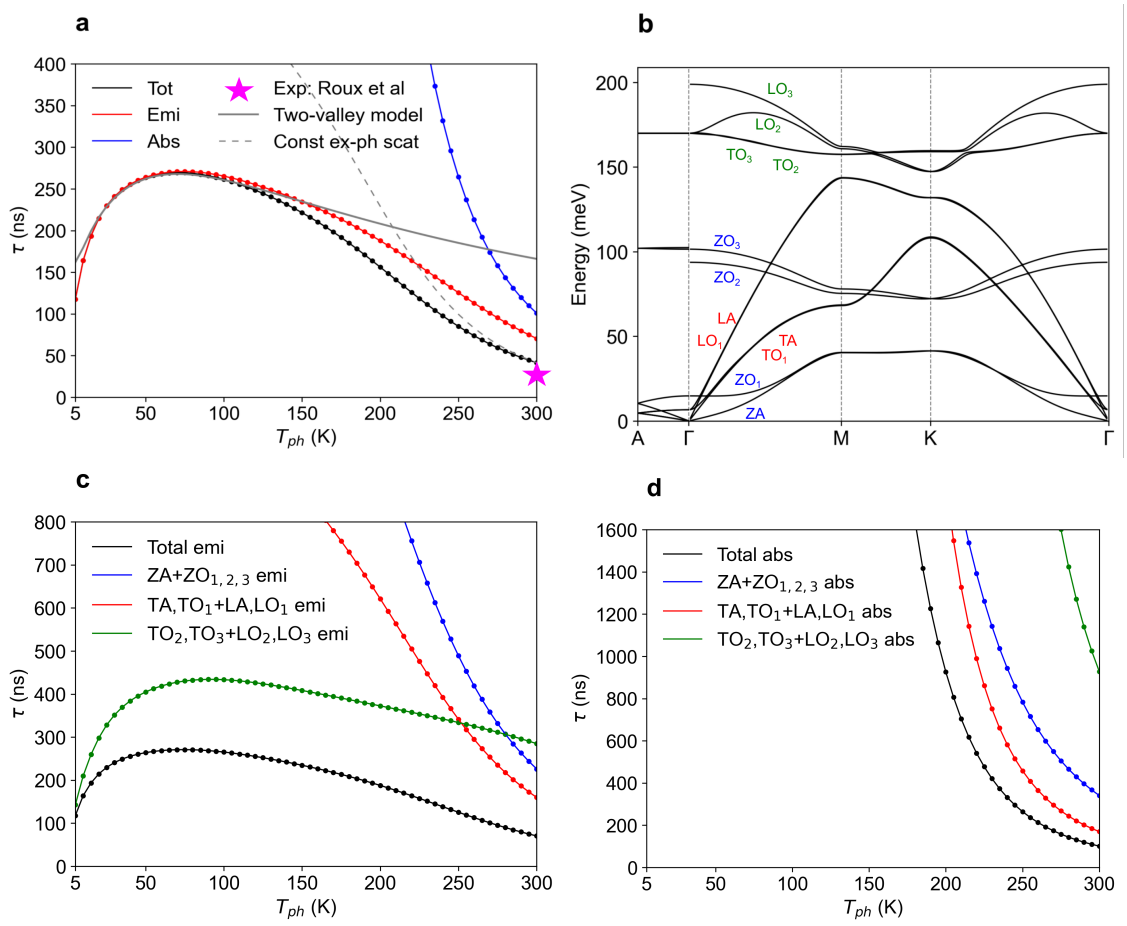

Figure 3.2: Temperature dependence of phonon-assisted radiative lifetime in bulk hBN. (a) Total radiative lifetime (black), with contributions from phonon emission (red) and phonon absorption (blue) shown separately. The magenta star marks the experimental radiative lifetime of 27 ns at room temperature, reported by S. Roux et al. [94]. The gray solid line represents a fit using a two-valley model, capturing the non-monotonic behavior at low temperatures. The gray dashed line corresponds to Eq. 3.68 using constant exciton-phonon coupling $\mathcal{G}$. (b) Labeling of phonon branches in the phonon band structure of bulk hBN. (c) Phonon mode contributions to the radiative lifetime from phonon emission processes. (d) Phonon mode contributions to the radiative lifetime from phonon absorption processes.

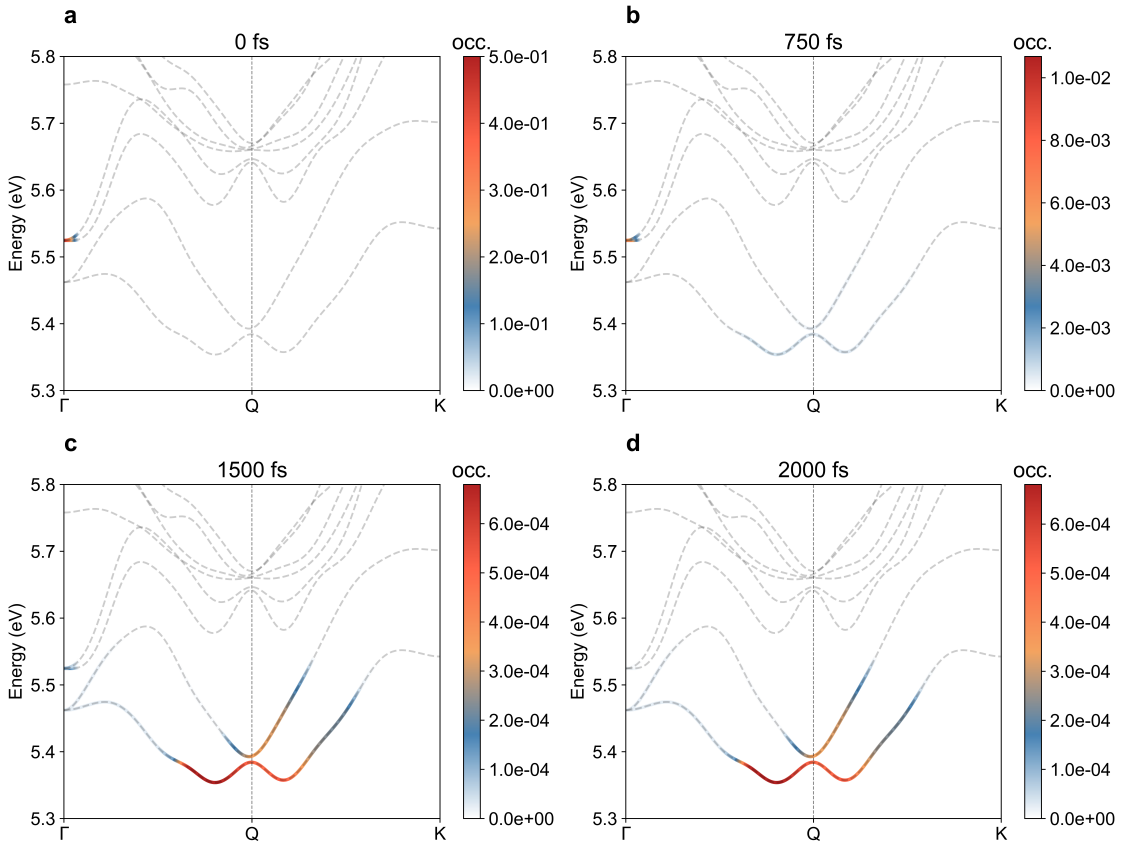

Figure 3.3: Real-time exciton occupation of bulk hBN at room temperature simulated using the real-time semi-classical quantum master equation Eq. (3.82) at different time steps: (a) 0 fs (initial step), (b) 750 fs, (c) 1500 fs, and (d) 2000 fs (final step). Exciton occupation is projected onto the exciton band structure and plotted as a colormap along $\Gamma \to Q \to K$.

mode of frequency $\tilde{\omega}$.

At low temperatures, the phonon emission process dominates. The corresponding thermal-averaged radiative rate is approximately

$$\gamma(T) \sim \tilde{\gamma}_1 \left(\frac{1}{1 + e^{-\beta \Delta E}} \right) \left(\frac{1}{e^{\beta \hbar \tilde{\omega}} - 1} + 1 \right), \tag{3.84}$$

where the first bracket accounts for thermal occupation of the dominant valley and decreases with increasing temperature, while the second bracket describes the phonon emission contribution, which increases with temperature. Their competition leads to the observed non-monotonic behavior of the total and phonon-emission lifetimes in the low-temperature regime. The fitted two-valley model, shown as the gray solid line in Fig. 3.2(a), agrees well with the first-principles results in this regime.

Above 150 K, the radiative lifetime decreases monotonically with temperature, driven by the rapid increase in phonon population as $k_B T$ becomes comparable to the phonon energy. To isolate this effect, we set the exciton-phonon matrix elements in Eq. 3.68 to a constant chosen to match the calculated radiative rate at room temperature. The resulting gray dashed curve in Fig. 3.2(a) reproduces the overall trend, confirming that high-temperature behavior is primarily governed by phonon population, rather than valley-dependent scattering details.

We further analyze the mode-resolved phonon contributions to the radiative lifetime, distinguishing between phonon emission and absorption processes, as shown in Figs. 3.2(b-d). In the phonon emission case [Fig. 3.2(c)], high-energy optical modes (green) dominate at low temperature due to their strong coupling with excitons. Their contribution remains relatively stable with increasing temperature due to much higher phonon energies compared to thermal energy $k_B T$. As temperature rises, low-energy optical and acoustic modes (red and blue) contribute more significantly due to increased phonon occupations. In contrast, phonon absorption contributions [Fig. 3.2(d)] are negligible at low temperature due to the lack of thermally populated phonons. At higher temperatures, low-energy optical and acoustic modes dominate absorption-assisted radiative transitions, as their occupation numbers increase rapidly.

Finally, we investigate real-time exciton dynamics using Eq. (3.82). The initial exciton population is fully assigned to the first bright exciton state, with total occupation $f = 1$, consistent with the dilute limit. As shown in Figs. 3.3(a–d), the exciton distribution relaxes toward low-energy valleys near $\mathbf{Q}$ due to exciton-phonon scattering. The population evolves exponentially toward thermal equilibrium, with a fitted valley relaxation time of approximately 114 fs at room temperature. This timescale agrees with experimental PL linewidth measurements [116], where a linewidth of ~ 30 meV implies a relaxation time of ~ 60 fs via the optical theorem: $\tau^{-1} = \frac{2\Delta}{\hbar}$. This framework provides a direct pathway for studying exciton dephasing and exciton spin dynamics, capturing quantum coherence effects [130, 85] that are absent in the semiclassical limits.

3.8 Computaional Details

Our first-principles implementation is based on Density Functional Theory (DFT) to determine ground-state electronic properties. Phonon dispersions and electron-phonon coupling matrix elements are computed using Density-Functional Perturbation Theory (DFPT), as implemented in the `Quantum ESPRESSO` (QE) [31, 30] and `EPW` [55] packages. Ground-state calculations employ the Pseudo Dojo [115] LDA pseudopotentials.

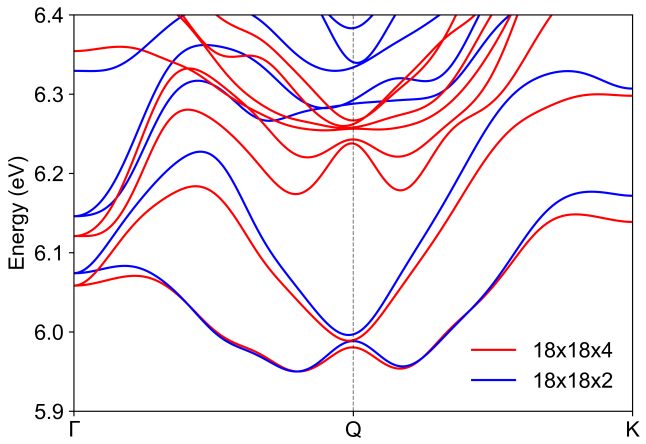

Figure 3.4: Exciton band structure using $18 \times 18 \times 4$ (red line) and $18 \times 18 \times 2$ (blue line) uniform sampling of $\mathbf{Q}$ and $\mathbf{k}$ grid, with the energy minimum shift to the 5.95 eV according to the experiment value of indirect optical gap of bulk hBN.

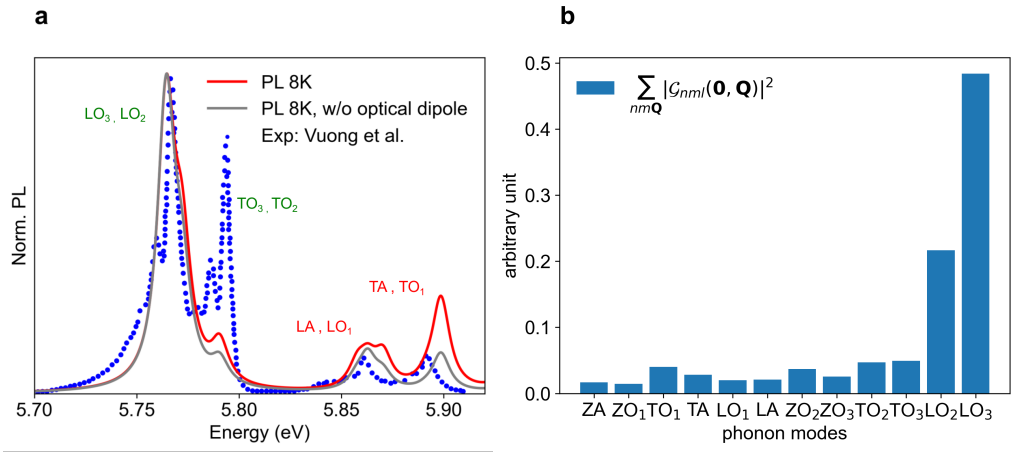

Figure 3.5: a) Calculated normalized photoluminescence (PL) spectrum of bulk hBN at 8 K (red line), compared with the result obtained without including the complex optical dipole matrix element $\boldsymbol{\mu}$ (gray line), and experimental data from Vuong et al. [116] (blue dots). b) Histogram of phonon mode dependence of the sum of exciton-phonon matrix element module square $|\mathcal{G}_{\mathrm{nml}}(\mathbf{0},\mathbf{Q})|^2$.

Exciton eigenvalues and amplitudes are obtained by solving the finite-momentum Bethe-Salpeter equation (BSE) using the `Yambo` code [59, 99]. To evaluate the exciton-phonon matrix elements at finite momenta, we interface electron-phonon coupling data from `EPW` with exciton states from `Yambo`, ensuring consistency by disabling all symmetry operations. Both exciton and electron-phonon calculations are performed on a uniform $\mathbf{k}$- and $\mathbf{q}$-point grid of $18 \times 18 \times 4$, using the same set of ground-state wavefunctions with no symmetry reduction.

A 10 Ry energy cutoff is used for the dielectric screening, GW self-energy, and the BSE kernel. GW calculations include 200 bands, with convergence accelerated via the efficient algorithm introduced in Ref. [8]. To match experimental optical properties, we align the computed exciton energies with the measured indirect optical gap of 5.95 eV for bulk hBN [116, 15], as shown in Fig. 3.4. For dielectric screening, we adopt static experimental values $\epsilon_{xx} = \epsilon_{yy} = \epsilon_{\parallel} = 6.9$ and $\epsilon_{zz} = \epsilon_{\perp} = 3.5$ [101, 66, 76, 53]. The BSE kernel includes two valence and two conduction bands, which we verify to be sufficient to converge the optical observables in this work.

We show the calculated normalized PL spectrum and phonon-mode-resolved exciton-phonon coupling strength in Fig. 3.5. A comparison of PL spectra with and without explicitly including the optical dipole matrix element $\boldsymbol{\mu}$ shows good agreement within the phonon sideband energy window [Fig. 3.5(a)], due to its narrow range. However, for broader optical spectra, such as absorption, it is essential to retain the full dipole matrix element to account for multiple bright exciton states with different optical strengths. The phonon mode-resolved coupling strength shown in Fig. 3.5(b) confirms that high-energy optical modes dominate exciton-phonon interactions. The squared exciton-phonon matrix elements $|\mathcal{G}|^2$ and the exciton/phonon energies are linearly interpolated onto a fine $36 \times 36 \times 8$ grid to compute the radiative properties.

Real-time Boltzmann transport equation (rt-BTE) simulations are also performed on the same fine grid for both $\mathbf{Q}$ and $\mathbf{q}$ points. The squared exciton-phonon matrix elements and exciton/phonon energies are interpolated consistently. Phonon populations are assumed to follow the Bose-Einstein distribution. A Gaussian broadening of 5 meV is used for the energy-conserving Dirac delta function δ_G. To initialize the simulation, the first bright optical exciton is assigned an occupation number of 1, consistent with the dilute exciton limit. The time evolution of the exciton distribution is simulated with a 10 fs time step over 200 steps, allowing the system to relax toward thermal equilibrium. The resulting time-resolved exciton occupations and thermalized exciton population distributions are shown in Fig. 3.6 and Fig. 3.7.

We present the exciton energy landscape and state-resolved phonon-assisted radiative

lifetimes at low temperature (5 K) for the lowest exciton band near the Q $= (\frac{1}{6}, \frac{1}{6}, 0)$ point (in crystal units), based on direct calculations using an $18 \times 18 \times 4$ **Q**-grid in reciprocal space, as summarized in Table 3.1. Exciton energies are aligned to the experimental indirect optical gap of 5.95 eV [116, 15] for computing optical properties. Multiple valleys are identified in the vicinity of the Q point, with corresponding state-resolved lifetimes τ symmetrized for energy-degenerate states.

Exciton **Q**	Energy (eV)	$\tau_{\mathbf{Q}}$ (ns)
$(\frac{3}{18}, \frac{2}{18}, 0)$	5.950	217.8
$(\frac{2}{18}, \frac{3}{18}, 0)$	5.950	217.8
$(\frac{4}{18}, \frac{2}{18}, 0)$	5.953	602.9
$(\frac{2}{18}, \frac{4}{18}, 0)$	5.953	602.9
$(\frac{4}{18}, \frac{3}{18}, 0)$	5.954	312.6
$(\frac{3}{18}, \frac{4}{18}, 0)$	5.954	312.6
$(\frac{2}{18}, \frac{2}{18}, 0)$	5.977	183.4
$(\frac{3}{18}, \frac{3}{18}, 0)$	5.986	143.6
$(\frac{4}{18}, \frac{4}{18}, 0)$	6.004	139.4

Table 3.1: Exciton energy and state-resolved phonon-assisted radiative lifetime of the lowest exciton band around Q $= (\frac{1}{6}, \frac{1}{6}, 0)$ point. The exciton wave vector **Q** is chosen to be in-plane.

Within the irreducible Brillouin zone, the lowest-energy exciton valley (denoted "valley 1") is located at $\mathbf{Q}_1 = (\frac{3}{18}, \frac{2}{18}, 0)$, with an energy of 5.950 eV and a radiative lifetime $\tau_{\mathbf{Q}_1} =$ 217.8 ns. The next-lowest valley ("valley 2") appears at $\mathbf{Q}_2 = (\frac{4}{18}, \frac{2}{18}, 0)$, with an energy of 5.953 eV and a substantially longer lifetime of 602.9 ns. These values are consistent with the two-valley model described in the main text: the fitted effective lifetime for valley 1 is $\tau_1 = \tilde{\gamma}_1^{-1} \approx 160$ ns, and the fitted energy separation ΔE ≈ 2 meV agrees well with the computed difference of 3 meV between $\mathbf{Q}_1$ and $\mathbf{Q}_2$. These results validate the two-valley

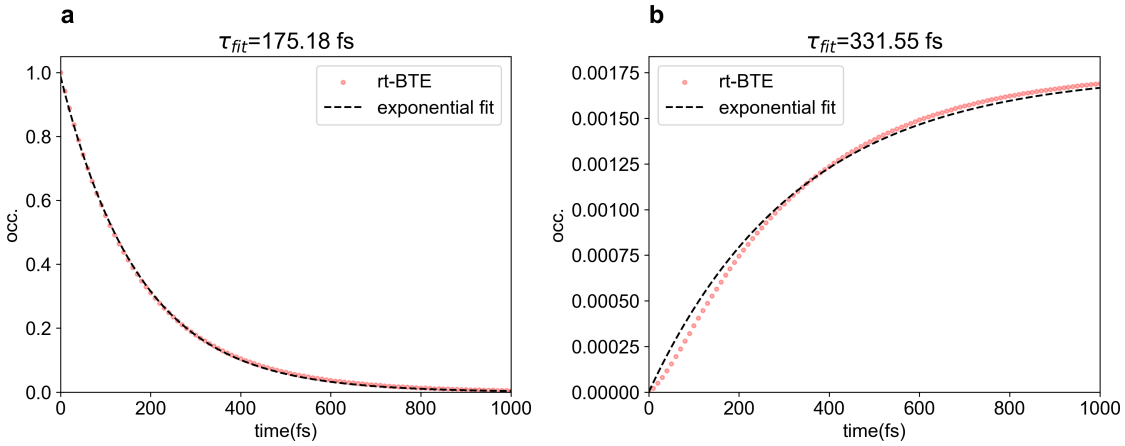

Figure 3.6: Real-time exciton occupation dynamics of bulk hBN at room temperature. a) Relaxation dynamics starting from the initial bright exciton at the Γ point. b) Relaxation dynamics at the lowest energy valley $\mathbf{Q} = \mathbf{Q}_1$ of the lowest band. The data points (red dots) are obtained from real-time Boltzmann transport equation (rt-BTE) simulations. The black dashed lines show exponential fits to the data, from which the relaxation time τ_{fit} is extracted.

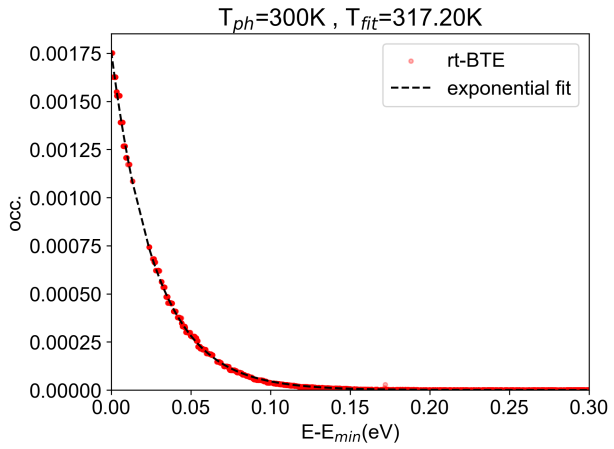

Figure 3.7: The calculated exciton occupation number (red dots) as a function of exciton energy in the final step (2000 fs) of rt-BTE simulation. The phonon temperature (lattice temperature) is set to room temperature (300 K). The fitted effective exciton temperature is 317.2 K using an exponential fit of Boltzmann distribution (black dashed line). The results show that at the final step, the simulated exciton distribution approaches the steady-state regime, with an effective exciton temperature close to the lattice temperature.

model as a qualitatively description of the exciton band-edge properties and its impact on the phonon-assisted radiative recombination process at low temperatures.

The associated exciton relaxation dynamics are illustrated in Fig. 3.6. The phonon population is assumed to follow the Bose-Einstein distribution at room temperature. From the time evolution of exciton occupations, we extract valley-specific relaxation times. The fitted decay time for the initial bright exciton at Γ is $\tau_{\text{fit}}(\Gamma) \approx 175$ fs, while the relaxation time at the lowest valley $\mathbf{Q}_1$ is $\tau_{\text{fit}}(\mathbf{Q}_1) \approx 331$ fs. The effective overall relaxation time between these two states, is estimated as

$$\tau_{\text{relax}} = \left[\tau^{-1}(\mathbf{Q} = \Gamma) + \tau^{-1}(\mathbf{Q}_1)\right]^{-1} \approx 114 \text{ fs}.$$

This estimate provides a direct quantification of the ultrafast exciton relaxation timescale governed by exciton-phonon scattering.

The final exciton distribution after 2000 fs of evolution is shown in Fig. 3.7. A Boltzmann fit of the steady-state distribution yields an effective exciton temperature of $T_{\text{ex}}^{\text{eff}} \approx 317$ K, closely matching the lattice temperature of 300 K, indicating that the system has reached thermal equilibrium.

3.9 Conclusion

In summary, we developed a comprehensive *ab-initio* framework for evaluating phonon-assisted radiative processes and exciton dynamics in semiconductors, based on time-dependent second-order perturbation theory and many-body perturbation theory, starting with an effective exciton-photon-phonon Hamiltonian. By applying this formalism to a prototypical indirect materials bulk hBN, we computed the phonon-assisted radiative lifetime in a wide range of temperatures and found good agreement with the available experimental data. The resulting temperature dependence of the radiative lifetime is non-monotonic at low temperatures and monotonically decreases at higher temperatures above 150 K. This trend contrasts with the conventional $T^{3/2}$ increase observed for direct exciton radiative lifetime [52, 18, 45]. We explain the non-monotonic behavior at low temperatures with a simplified two-valley model, where a large difference in scattering rates between different valleys plays a critical role. At higher temperatures, the decrease in radiative lifetime is shown to be governed by the thermal occupation factors. To capture the out-of-equilibrium dynamics of excitons, we derived and implemented a real-time quantum master equation in the Lindblad formalism. In the semiclassical limit, this reduces to the Boltzmann transport equation (BTE) with exciton-phonon scattering dynamics. Our simulations reveal ultrafast

relaxation of excitons into finite-momentum valleys with information of relaxation and thermalization dynamics. This framework lays the groundwork for future extensions to study exciton coherence, dephasing, and exciton spin dynamics in realistic materials.

Chapter 4

Substrate Screening Approach for Quasiparticle Energies

4.1 Introduction

Two-dimensional (2D) materials and their heterostructures have emerged as a platform for exploring novel physical phenomena and enabling technological applications in diverse areas such as opto-spintronics [123, 138], quantum information science [41, 111], and biomedical engineering [119, 109]. Unique quantum effects including unconventional superconductivity [14, 13] and topologically protected states [105, 3, 81, 80] which can emerge through layer stacking and interface engineering in these systems. Experimentally, 2D materials are typically supported on substrates during growth via epitaxial techniques or chemical vapor deposition (CVD) [65]. The presence of a substrate can significantly modify the electrical and optical properties of the 2D layer by influencing its dielectric environment. For instance, substrate screening can reduce the fundamental quasiparticle gap [122, 114]. Therefore, accurate prediction of substrate-induced screening effects is essential for interpreting experimental measurements and guiding materials design. Although hybrid functionals such as HSE06 [50] perform well for bulk materials, they become incompatible for low-dimensional systems with strongly inhomogeneous dielectric screening. More sophisticated approaches, such as Koopmans-compliant [107, 63, 120] or dielectric-dependent hybrid functionals [137], are necessary to describe 2D materials. In such cases, the fraction of Fock exchange must be determined individually for each system, depending on layer thickness and dimensionality [104].

Alternatively, many-body perturbation theory (MBPT) provides a parameter-free and accurate description of both quasiparticle and excitonic properties [77, 44, 99]. Charged

excitations and neutral excitations can be computed using the GW approximation [35, 124, 75] and the Bethe-Salpeter equation (BSE) [90, 125, 78, 89], respectively. However, direct application of GW/BSE to full interface supercells is computationally expensive and often impractical for exploring a wide range of substrate materials. To address this, approximate methods have been developed to compute the quasiparticle properties of interfaces by combining primitive-cell calculations of individual layers [112, 133, 114]. For weakly bonded van der Waals (vdW) heterostructures, the dominant interfacial effect is the modification of dielectric screening, rather than wavefunction hybridization [133]. Within the GW framework, this can be described by approximating the dielectric matrix of the full interface from the dielectric responses of its individual constituents [114, 112]. Despite their success, these methods often involve uncontrolled approximations such as neglecting local-field effects or off-diagonal components of the dielectric matrix [10, 84] which have not been systematically evaluated. We examine the validity of such approximations by explicitly testing their impact on both in-plane and out-of-plane dielectric components across a range of systems. Furthermore, these methods are limited to commensurate interfaces, where an integer relation between lattice constants must be satisfied ($L \cdot N = \tilde{L} \cdot \tilde{N}$). Artificially straining one or both layers to enforce lattice matching may distort the electronic structure. To overcome this limitation, we introduce a reciprocal-space linear interpolation scheme over the full $\mathbf{q} + \mathbf{G}$ space that enables dielectric matrix construction for arbitrarily mismatched interfaces without the need for supercell strain or commensurability. To demonstrate the accuracy and versatility of our approach, we study hexagonal boron nitride (hBN) interfaces. hBN is a wide-bandgap material with applications in deep-UV optoelectronics [51] and quantum information, serving as a host for single-photon emitters and spin qubits [126, 5]. Accurate treatment of substrate screening is crucial for interpreting its optical and defect properties [1, 118], particularly since most measurements are performed with hBN supported on substrates. In this work, we investigate hBN/SnS_2 heterostructures and bilayer hBN with different stacking conformations as prototypical examples.

This work was published as an Editors' Suggestion in Guo *et al.*, *Phys. Rev. B* **102**, 205113 (2020) [39].

4.2 Methodology

In this section, we will discuss the different methods and concepts used in this paper, which are summarized in the Table 4.1.

Table 4.1: Overview of methodology in this work.

Methods	**Assumption**
χ_{eff}-sum (Eq. 4.3)	Coulomb interaction between layers
χ_{eff}^{GSC}-sum	Uses interface eigenvalue in χ_{eff}-sum
χ_{eff}^{FWF}-sum	Uses interface eigenvalue and wavefunctions in GW with χ_{eff}-sum
χ_0-sum (Eq. 4.4)	Coulomb interaction between layers, equiv. to χ_{eff}-sum at RPA
χ-sum (Eq. 4.6)	No interaction between layers
Approximations	**Definition**
ϵ^{-1}-diag	Neglects χ^s off-diagonal elements
ϵ-diag	Neglects χ_0^s off-diagonal elements
Interface structure	**Solution**
Lattice match	Direct summation
Special match	$\mathbf{q}+\mathbf{G}$ mapping
Arbitrary mismatch	$\mathbf{q}+\mathbf{G}$ bilinear interpolation

4.2.1 Methods for interface polarizability

The interactions among quasi-particles within the GW approximation is described by the screened Coulomb potential $W = \epsilon^{-1}v_C$, where v_C is the bare Coulomb interaction and ϵ is the dielectric matrix. The inverse dielectric matrix is defined by $\epsilon^{-1} = \mathbb{1} + v_C\chi$ within the random phase approximation (RPA) [44]. The reducible polarizability χ can be obtained from the irreducible polarizability χ_0 (also known as independent-particle polarizability) through the equation $\chi = \chi_0 + \chi_0 v_C \chi$.

For the purpose of our discussion we first partition the total ("tot") vdW interface systems into material ("m") and substrate ("s") subsystems [133]. Considering density response of external field, we obtain:

$$\begin{aligned} \delta n^m &= \chi^m(\delta V_{\text{ext}} + v_C \delta n^s), \\ \delta n^s &= \chi^s(\delta V_{\text{ext}} + v_C \delta n^m), \end{aligned} \tag{4.1}$$

where δn is the density response, and the reducible polarizability χ is defined as the density-density response function to an applied potential. If we consider the material subsystem ("m") as the probe, the total external potential includes the external applied potential (δV_{ext}) and the Coulomb potential from the charge response δn^s in the substrate

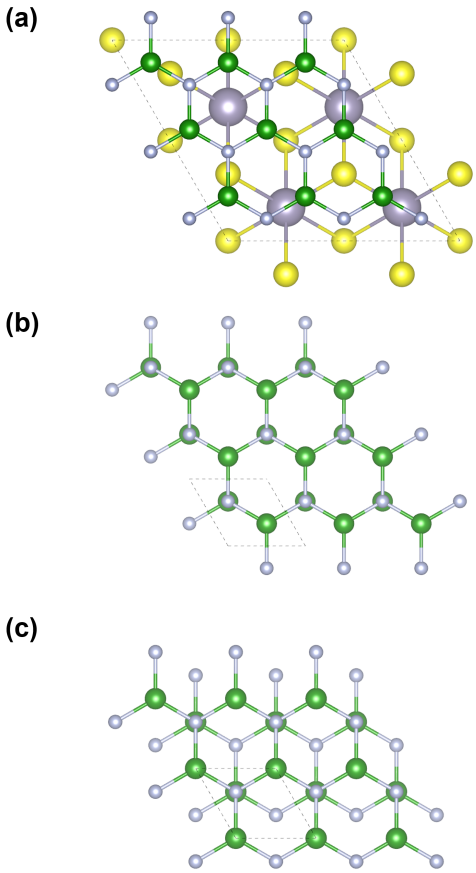

Figure 4.1: Atomic structure of 2D interfaces a) hBN/SnS_2, b) bilayer hBN with AB stacking, c) bilayer hBN with AA′ stacking. The green balls denote boron atoms; the white balls denote N atoms; the yellow balls denote sulfur atoms; the silver balls denote Sn atoms.

$(v_C \delta n^s)$. (We assume the material and substrate are connected only through interlayer Coulomb interactions, with minimum wavefunction overlap between material and substrates, i.e. interlayer hybridization.) Then we define an effective polarizability χ_{eff} as a density response function of one subsystem to only the external applied potential (δV_{ext}), i.e. $\chi_{eff}^{m/s} = \delta n^{m/s}/\delta V_{ext}$. More precisely, $\chi_{eff}^{m/s}$ can be given in terms of $\chi^{m/s}$ through Eq. 4.1:

$$\begin{aligned} \chi_{eff}^{m/s} &= \frac{\delta n^{m/s}}{\delta V_{ext}} \\ &= (\mathbb{1} - \chi^{m/s} v_C \chi^{s/m} v_C)^{-1} (\chi^{m/s} + \chi^{m/s} v_C \chi^{s/m}). \end{aligned} \tag{4.2}$$

When subsystems have negligible interlayer wavefunction overlap (i.e. hybridization), the total density response (δn^{tot}) can be written as $\delta n^{tot} = \delta n^m + \delta n^s$ and then the total

polarizability χ^{tot} of entire interface systems is

$$\chi^{tot} = \frac{\delta n^{tot}}{\delta V_{ext}} = \frac{\delta n^{m}}{\delta V_{ext}} + \frac{\delta n^{s}}{\delta V_{ext}} = \chi^{m}_{eff} + \chi^{s}_{eff}. \tag{4.3}$$

In summary, this approach uses the reducible polarizabilty of each subsystem ($\chi^{m/s}$) where the Coulomb potential from the other subsystem is considered part of external potential in Eq. 4.1, to construct the effective reducible polarizability $\chi^{m/s}_{eff}$ of each subsystem where such potential is excluded from external potential in Eq. 4.2. Then we sum up χ^{m}_{eff} and χ^{s}_{eff} to obtain total reducible polarizability of interface systems χ^{tot} in Eq. 4.3, which will be denoted as "χ_{eff}-sum".

As we noted above, interlayer wavefunction overlap or hybridization effect is not taken into account in the method described above. The hybridization effect can change the eigenvalues and eigenfunctions at the DFT level which then change the Green's function (G) and dielectric matrix (in W) in the GW calculations. Therefore, for systems with strong interlayer hybridization, we can add the hybridization effect step-by-step. We can add corrections from ground state eigenvalues of interfaces to the χ_{eff}-sum methods, namely "χ^{GSC}_{eff}-sum" method, which partially take into account the effect of interlayer hybridization on eigenvalues at the DFT level. Furthermore, we can also include interface ground state wavefunction ("FWF") and eigenvalues as inputs for Green's function (G), denoted as "χ^{FWF}_{eff}-sum" method. This method is close to GW calculations of an explicit interface except with approximate dielectric matrix by Eq. 4.3.

From another perspective, if the interlayer hybridization or wavefunction overlap is negligible (similar to the condition required above for δn^{tot}) [56, 132], the total irreducible polarizability χ^{tot}_0 of the interfaces can be expressed approximately as the sum of each subsystem contribution [10, 114, 84, 62, 132, 56]

$$\chi^{tot}_0 = \chi^{m}_0 + \chi^{s}_0, \tag{4.4}$$

which we denote as "χ_0-sum" method. To further understand the theoretical connection between different methods, we rewrite Eq. 4.1 with χ_0 through relation $\chi = \chi_0 + \chi_0 v_C \chi$ as:

$$\begin{aligned} \delta n^{m} &= \chi^{m}_0(\delta V_{ext} + v_C \delta n^{s} + v_C \delta n^{m}), \\ \delta n^{s} &= \chi^{s}_0(\delta V_{ext} + v_C \delta n^{m} + v_C \delta n^{s}). \end{aligned} \tag{4.5}$$

Here χ_0 as the irreducible polarizability is the density response function to total field

δV_{tot}, which includes the applied field and bare Coulomb potential of the total interface system, namely $\delta V_{tot} \equiv \delta V_{ext} + v_C \delta n^{tot}$. Using the above condition $\delta n^{tot} = \delta n^m + \delta n^s$ for the interface, summation of the two equations of subsystems in Eq. 4.5 results in $\delta n^{tot} = \chi_0^{tot} \delta V_{tot} = (\chi_0^m + \chi_0^s)\delta V_{tot}$, which gives Eq. 4.4. This indicate that the χ_{eff}-sum method and χ_0-sum method are equivalent under RPA. However, χ_{eff}-sum method and χ_0-sum method are not equivalent when the diagonal approximation is applied, i.e. neglecting off-diagonal elements of χ in the former or χ_0 in the latter, as we will discuss in the Sec. II.B. Therefore we primarily used χ_{eff}-sum method in this paper.

If we further neglect the interlayer Coulomb interaction, this will set $v_C \delta n^{m/s}$ to zero in Eq. 4.1 and lead $\chi_{eff} \to \chi$. This is at the non-interacting limit between two layers, where

$$\chi^{tot} = \chi^m + \chi^s, \tag{4.6}$$

and we name it as "χ-sum" method. In Sec. 4.3.1, we will compare the quasiparticle energies of interfaces with the above approximated dielectric matrices with explicit interface GW calculations.

4.2.2 Diagonal approximation of dielectric screening

For simple metals which may be treated as "jellium", the nearly translational invariance justifies the dielectric matrix ϵ may be diagonal in reciprocal space [44]. However, semiconductors and insulators have strong in-homogeneity at interaction length scale requires non-zero off-diagonal elements of ϵ [87, 44]. The effect from off-diagonal elements of dielectric matrix ϵ is often referred to the "local field effect" [16, 87, 44].

While the effect of off-diagonal terms in intrinsic dielectric screening has been systematically studied [16, 87, 44], the off-diagonal terms' effect from environmental dielectric screening has not been studied in detail. Here we will investigate the off-diagonal effect of environmental dielectric screening through two different approaches, i.e. by applying the diagonal approximation of dielectric matrix ϵ ("ϵ-diag", which directly relates to diagonal approximation of χ_0) or inverse dielectric matrix ϵ^{-1} ("ϵ^{-1}-diag", which directly relates to diagonal approximation of χ and χ_{eff}).

The ϵ-diag approximation has been used for substrate dielectric screening in the past work [10, 114, 84, 62] when applying the χ_0-sum method, specifically, by removing the in-plane off-diagonal components of substrate dielectric matrices. The ϵ^{-1}-diag approximation has not been employed before, but is more convenient in the χ_{eff}-sum approach. Since the off-diagonal elements of χ_0 will contribute to the diagonal elements of χ and ϵ^{-1} through

the matrix inverse operation, this is a weaker approaximation than ϵ-diag. We will compare these two approximations considering specific numerical examples in Sec. 4.3.2.

4.2.3 Reciprocal-space linear-interpolation approach

The construction of interface structure models is often complicated by the problem of lattice matching between two subsystems. One of the main objectives of this work is to propose a general approach that can be applied to subsystems with rather different periodicity and crystal symmetry, and does not require the application of strain to force the lattice matching at the interface.

In general, in order to directly sum the subsystem contributions to obtain the polarizability (and dielectric matrix) of the full interface, one needs an exact correspondence of the $\mathbf{q}+\mathbf{G}$ vectors between the material and the substrate. This requires finding two integer numbers N and $\tilde{N}$ such that the lattice constants L (substrate) and $\tilde{L}$ (material) satisfy the relation $L \cdot N = \tilde{L} \cdot \tilde{N}$. If N and $\tilde{N}$ can be chosen to be reasonably small, calculations can be directly performed for supercells containing N and $\tilde{N}$ repetitions, although this approach often requires the application of a small percentage of strain. However, if the required N or $\tilde{N}$ are large, several methods have been proposed to make this type of calculations practical [10, 114, 84, 62, 132, 56]. The central idea is to consider unit cells only and to perform a one to one mapping between the reciprocal space $\mathbf{q}+\mathbf{G}$ vectors of the material and substrate [56] (see Figure 4.2(a)). This approach still requires the relation $L \cdot N = \tilde{L} \cdot \tilde{N}$ to be satisfied (possibly by applying a small strain to modify L or $\tilde{L}$) but avoids supercell calculations. We note that even if one applies the diagonal approximation for χ_0 or χ, the diagonal elements still contain both $\mathbf{q}$ and $\mathbf{G}$ vectors, which requires this relation to be satisfied. While this is a clear numerical improvement, a large number of $\mathbf{q}$ vectors in the first Brillouin zone might still be required. Indeed, one needs to sample $\mathbf{q}$ and/or $\tilde{\mathbf{q}}$ point meshes fine enough to ensure that the number of $\mathbf{q}$ points ($N_{\mathbf{q}}$) satisfy the relation $L \cdot N_{\mathbf{q}} = \tilde{L} \cdot N_{\tilde{\mathbf{q}}}$ or equivalently $N_{\mathbf{q}}/N_{\tilde{\mathbf{q}}} = N/\tilde{N}$. Accordingly, this approach becomes computationally demanding for large N and/or $\tilde{N}$. A more serious issue is that this mapping scheme is not possible for interfaces with two systems with very different crystal symmetry, e.g. a hexagonal and a lattice.

In this work we propose a general method for arbitrarily lattice-mismatched interfaces where it is not possible to map the $\mathbf{q}+\mathbf{G}$ vectors between the two subsystems. This approach applies a linear interpolation of the matrix elements on the substrate grid ($\mathbf{q}+\mathbf{G}$, $\mathbf{q}'+\mathbf{G}'$) to obtain their representation on the material grid ($\tilde{\mathbf{q}}+\tilde{\mathbf{G}}$, $\tilde{\mathbf{q}}'+\tilde{\mathbf{G}}'$), as shown in Figure 4.2(b) and (c). We note that we need to interpolate $\mathbf{q}+\mathbf{G}$ together between materials

and substrates, which can completely remove the symmetry constrain. Interpolation of $\mathbf{q}$ only as done in the past work [24, 48] will improve $\mathbf{q}$-sampling convergence speed but does not solve the periodicity or symmetry mismatch problem at interfaces. As this procedure requires a sampling of the $\mathbf{q}$ vectors over the full first Brillouin zone (FBZ), whenever necessary, the symmetry operators are used to reconstruct the grid in the FBZ from the grid in the irreducible Brillouin zone (IBZ). Without loss of generality we choose the same size for vacuum in the z-direction for both subsystems; in this way the same out-of-plane reciprocal lattice G_z components are obtained. In order to simplify the implementation, we neglect the in-plane off-diagonal elements of the substrate, i.e. we consider $v_C\chi^s_{\mathbf{G},\mathbf{G}'}(\mathbf{q}) \approx v_C\chi^s_{\mathbf{G}\mathbf{G}'}(\mathbf{q})\delta_{G_x,G'_x}\delta_{G_y,G'_y}$. As shown later for specific numerical examples (see Sec. 4.3.3), this approximation works well in practice for mismatched 2D interfaces. For each set of matrix elements at fixed $\{G_z, G'_z\}$, the standard bilinear interpolation technique [79] is used to obtain the corresponding in-plane matrix elements $v_C\chi_{G_z,G'_z}(\tilde{\mathbf{q}}_{x,y} + \tilde{\mathbf{G}}_{x,y})$ in the material subspace, interpolated from $v_C\chi_{G_z,G'_z}(\mathbf{q}_{x,y} + \mathbf{G}_{x,y})$ in the substrate subspace. As shown in Figure 4.2(b), the value of the response function $\epsilon^{-1} - \mathbb{1} = v_C\chi$ at each $\tilde{\mathbf{q}} + \tilde{\mathbf{G}}$ point (denoted by the black cross overlaying the blue dots) is obtained by interpolating the values at the four nearest $\mathbf{q} + \mathbf{G}$ points (denoted by the red cross overlaying the orange dots). We note that the bilinear interpolation method can be applied only if all four nearest neighbours exist within the boundaries of $\mathbf{q} + \mathbf{G}$ space; otherwise the standard proximal interpolation method is applied, which considers only the nearest point on the grid (most likely at the boundary), as shown in Figure 4.2(c). However, the values close to the boundary of $\mathbf{q} + \mathbf{G}$ space are very close to zero as shown in Figure 4.3(a).The bilinear interpolation method is fully general regardless of crystal symmetry, which can be applied to arbitrary interfaces.

By applying the interpolation method, we can obtain substrate $v_C\chi$ matrix elements at the material's $\tilde{\mathbf{q}} + \tilde{\mathbf{G}}$ grids, without any artificial strain [56, 114, 132]. As shown in Figure 4.3(a), the orange points are the $v_C\chi_{G_z,G'_z}(\mathbf{q}_{x,y} + \mathbf{G}_{x,y})$ values computed at the substrate momentum space with full BZ, then we interpolate them to the blue points on the grids of material momentum space $v_C\chi_{G_z,G'_z}(\tilde{\mathbf{q}}_{x,y} + \tilde{\mathbf{G}}_{x,y})$ (only elements in IBZ are shown here). The blue points fall smoothly on the surface of orange points which show a good interpolation quality. A zoomed-in picture is also shown in Figure 4.3(b). To show the generality of our method, we applied this interpolation method for hBN/phosphorene(BP) interface, where BP has a rectangle lattice, sharply different from the hexgonal lattice hBN has. We show again with our interpolation method, one can obtain the matrix elements of substrates at the material $\tilde{\mathbf{q}} + \tilde{\mathbf{G}}$ grids. Then we can compute the quasiparticle energies of this interface, at two systems' natural lattice constants, with the χ_{eff}-sum method.

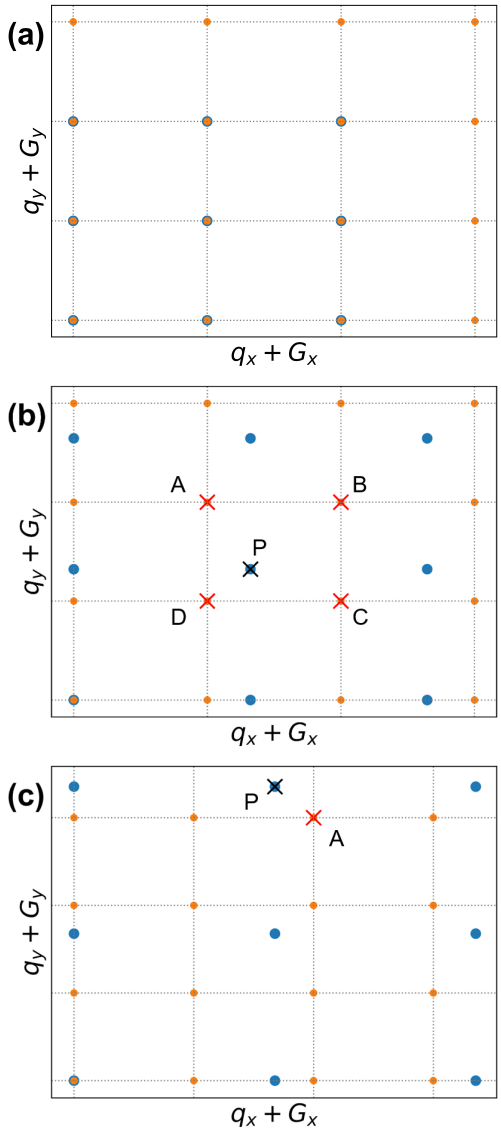

Figure 4.2: Schematic diagram of a) mapping between computed data points of substrate (orange dots) and computed data points of material (blue dots), where the reciprocal space $\mathbf{q} + \mathbf{G}$ grid from the substrate and $\tilde{\mathbf{q}} + \tilde{\mathbf{G}}$ grid from the material are overlapping; b) bilinear interpolation of the black cross point at P (from $\tilde{\mathbf{q}} + \tilde{\mathbf{G}}$ grid) from the four nearest data points A, B, C, D (red cross) when P is inside the boundary of the $\mathbf{q} + \mathbf{G}$ grid (orange dots); c) proximal interpolation with the only nearest one point A when the interpolation point is P at the boundary.

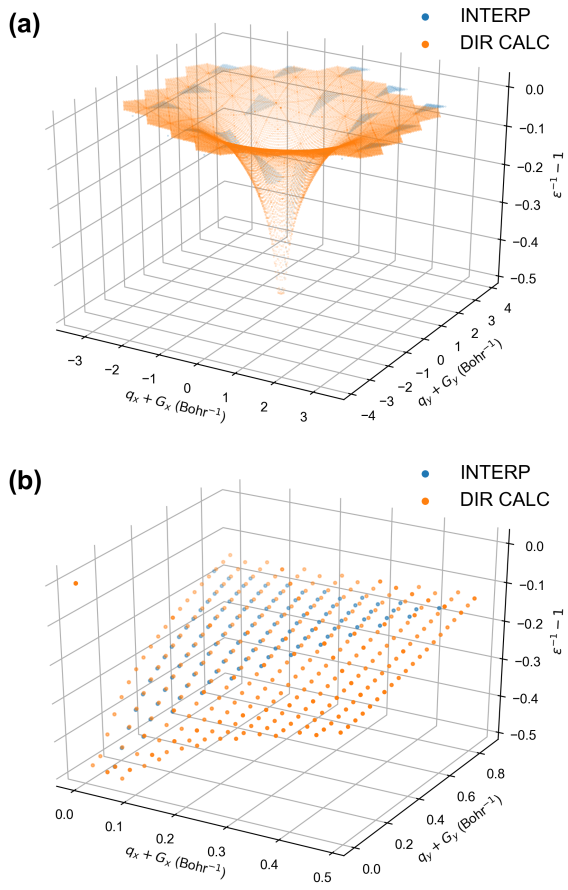

Figure 4.3: 3D plot of in-plane diagonal elements of function $\epsilon^{-1} - \mathbb{1}$ of SnS_2 substrate, with $\mathbf{G}$ vector subset $(G_z, G'_z) = (0, 0)$ in a) full reciprocal space; b) a zoomed-in portion of a) that contains the irreducible Brillouin zone of the interpolated points (blue) in hBN $\tilde{\mathbf{q}} + \tilde{\mathbf{G}}$ subspace. The $q_i + G_i, i = x, y$ are in-plane reciprocal space Cartesian coordinate in atomic unit (Bohr^{-1}). The orange points are directly computed data points ("DIR CALC") in SnS_2 substrate $\mathbf{q} + \mathbf{G}$ subspace, while the blue points are interpolated points ("INTERP") to (hBN) material $\tilde{\mathbf{q}} + \tilde{\mathbf{G}}$ subspace. Note that the orange points used for interpolating blue points in b) are beyond the first Brillouin zone of the substrate $\mathbf{q} + \mathbf{G}$ subspace. The single point at zero is the head element of $\epsilon^{-1} - \mathbb{1}$, which is exactly zero for both material and substrate.

4.3 Results and discussions

4.3.1 Numerical comparison of different methods for substrate screening

After presenting in Sec. 4.2 with different approaches to approximate the total dielectric screening of an interface between two weakly interacting subsystems, in this section we discuss their accuracy in practical GW calculations. Results for explicit interfaces will be used as a reference. Specifically, we computed the GW quasiparticle bandgaps of three interfaces: hBN/SnS_2, 2L-AB stacking hBN with two layers' atoms misaligned, and 2L-AA′ stacking hBN interface with two layers' atoms aligned (the corresponding atomic structures are shown in Figure 4.1). In order to keep the comparison of different methodologies as simple as possible, the calculations in this section are performed with fully commensurate interfaces, for both explicit and approximate interface calculations, as the results shown in Figure 4.4.

From the explicit interface results in Figure 4.4 we see that the direct band gap of hBN at the hBN/SnS_2 interface (black cross in the third column) is reduced by 0.8 eV compared with the isolated ML hBN (dashed line). This value is about four times of the band gap reduction for the bilayer hBN with respect to the isolated ML hBN (black cross in the first and second columns). This is because ML SnS_2 has a much stronger dielectric screening ($\epsilon_\infty \approx 17$) and a smaller electronic band gap (≈ 2 eV) compared to ML hBN, which has $\epsilon_\infty \approx 5$ and an electronic band gap of ≈ 7 eV. This indicates the positive correlation between electronic band gap reduction and substrate dielectric screening, similar to previous discussions [21, 67, 47].

Secondly, we find that the effective polarizability approach results ("χ_{eff}-sum" method, blue circle) are consistently in good agreement with the ones from explicit interface GW calculations ("Direct", black cross), i.e. within 0.2 eV. We improve the agreement by 50 meV with additional corrections from ground state eigenvalues of interfaces ("$\chi_{\text{eff}}^{\text{GSC}}$-sum" method, red triangle), which partially take into account the effect of interlayer couplings on eigenvalues at the DFT level. Moreover, by using interface ground state wavefunctions and eigenvalues ("FWF") as inputs for Green's function calculations, the results of the effective polarizability approximation ("$\chi_{\text{eff}}^{\text{FWF}}$-sum" method, green square) are further improved, i.e. with only 10 meV difference from the explicit interface GW calculations. While a similar approach was used in Ref. 132, the $\chi_{\text{eff}}^{\text{FWF}}$-sum method has a computational cost similar to that of the full interface GW calculation (although the evaluation of the dielectric matrix is more efficient) and is much more demanding than the other methods

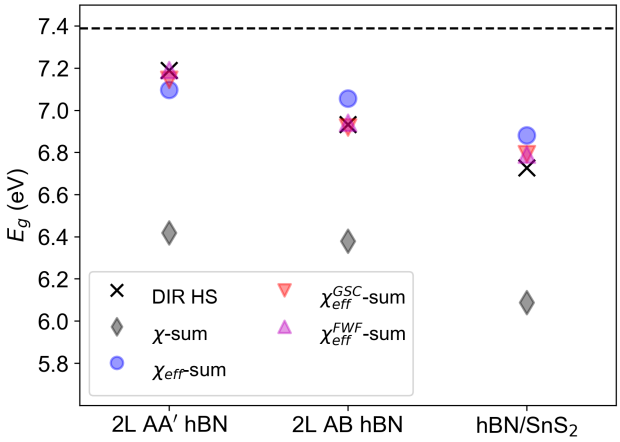

Figure 4.4: hBN direct band gap at K from several interfaces with different approximations of substrate screening, compared with explicit interface calculations. The black dashed line is the direct band gap at K of free-standing ML hBN. For each symbol in the figure, "DIR HS" with black cross denotes direct GW calculation of explicit heterostructure; "χ_{eff}-sum" with blue circle denotes sum of effective polarizability approach by Eq. 4.3 with ground state inputs from free-standing ML hBN; "$\chi_{\text{eff}}^{\text{GSC}}$-sum" method with red down triangle denotes "χ_{eff}-sum" method with additional eigenvalue corrections from ground state interface eigenvalues ("GSC"); "$\chi_{\text{eff}}^{\text{FWF}}$-sum" with magenta up triangle denotes "χ_{eff}-sum" method with both ground state eigenvalues and wavefunctions from interfaces; "χ-sum" denotes non-interacting "χ-sum" method by Eq. 4.6.

in Figure 4.4 and Table 4.1. Therefore χ_{eff}-sum and $\chi_{\text{eff}}^{\text{GSC}}$-sum provide the best compromise between accuracy and computational cost. We note that for explicit hBN/SnS_2 interface, we had to apply 1.5% strain to obtain commensurate supercells which may explain why this interface has slightly larger difference between χ_{eff}-sum and explicit calculation than bilayer hBN.

In sharp contrast to the methods discussed above, the non-interacting interlayer method based on Eq. 4.6 ("χ-sum" method, black diamond) gives results far from the explicit interface reference (e.g. with an error of about 0.6 eV). This indicates that the interlayer Coulomb interaction plays a dominant role in the electronic bandgap reduction by substrate screening.

4.3.2 Diagonal approximation of substrate dielectric screening

In this section we will compare different diagonal approximations for the screening considering different numerical examples. With "in-plane ϵ^{-1}-diag" we will denote an approximation that discards the in-plane off-diagonal elements of reducible polarizability χ in reciprocal space, i.e. $\chi_{\mathbf{GG'}}(\mathbf{q},\omega)\delta_{G_x,G'_x}\delta_{G_y,G'_y}$. Similarly, "out-of-plane ϵ^{-1}-diag" will denote

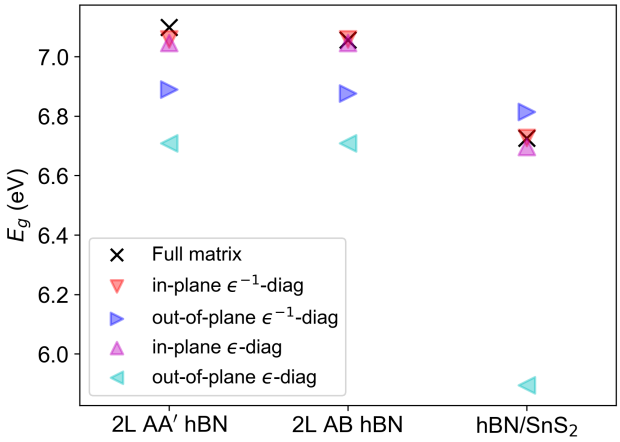

Figure 4.5: GW results for hBN direct band gap at K using "χ_{eff}-sum" or equivalently "χ_0-sum" method to examine the effect of diagonal approximations."Full matrix" in black cross denotes full dielectric matrices without any diagonal approximation as reference; "in-plane ϵ^{-1}-diag" in red down triangle denotes diagonal approximation to in-plane elements of ϵ^{-1}; "out-of-plane ϵ^{-1}-diag" in dark blue right triangle denotes diagonal approximation to out-of-plane elements for ϵ^{-1}; "in-plane ϵ-diag" in magenta up triangle denotes diagonal approximation to in-plane elements of ϵ; "out-of-plane ϵ-diag" in light blue left triangle denotes diagonal approximation to out-of-plane elements of ϵ.

an approach that does not include the out-of-plane off-diagonal elements of polarizability in reciprocal space, i.e. $\chi_{GG'}(\mathbf{q},\omega)\delta_{G_z,G'_z}$. Analogous definitions will be used for ϵ-diag.

The GW quasiparticle gaps with different diagonal approximations for the hBN bilayer in two different confomations (AA′/ AB) and the hBN/SnS_2 interface are shown in Figure 4.5. We find that for both the ϵ^{-1} and ϵ diagonal approximations, neglecting out-of-plane off-diagonal elements of the substrate ("out-of-plane ϵ^{-1}-diag" and "out-of-plane ϵ-diag", dennoted by dark blue right triangle and light blue left triangle, respectively) causes a large discrepancy of the bandgaps (i.e. from 0.2 to 0.8 eV) with respect to the "exact" result obtained from the full screening matrix ("Full matrix", black cross). In contrast, the results obtained by neglecting in-plane off diagonal elements (in-plane ϵ^{-1}/ in-plane ϵ-diag, red down triangle/ magenta up triangle) are similar to those with the full screening matrix with deviations within 50 meV. This means the inhomogeneity effect of out-of-plane substrate screening on quasiparticle energies is much stronger than the one of in-plane substrate screening, because the out-of-plane direction is along the non-periodic (vacuum) direction with dramatically inhomogeneous charge distribution, compared to the in-plane periodic direction.

Besides the overall difference of diagonal approximation along different directions, we also distinguish the difference between ϵ^{-1}-diag and ϵ-diag approach in each case. 1)

Along the in-plane direction, the difference between different approaches is negligible, i.e. less than 10 meV. 2) Along the out-of-plane direction, the out-of-plane ϵ^{-1}-diag results (dark blue right triangle) are much closer to the full dielectric matrix results (black cross) than the out-of-plane ϵ-diag results (light blue left triangle) in Figure 4.5. This is consistent with our earlier speculation that the ϵ^{-1}-diag may be a better (weaker) approximation, because the off-diagonal elements of irreducible polarizability χ_0 contribute to χ or ϵ^{-1} during its matrix inversion, which is completely missing in the ϵ-diag approximation.

Moreover, the in-plane inhomogeneity is relatively larger when there is stronger interlayer coupling with atoms aligned perfectly for chemical bonding. For example, the in-plane inhomogeneity of bilayer hBN with atoms aligned (e.g. 2L AA′ hBN in Figure 4.1 (b); both in-plane ϵ^{-1}-diag (red down triangle) and in-plane ϵ-diag (magenta up triangle) results have 40 meV difference from the "Full matrix" results in the first column of Figure 4.5), is larger than the interfaces with atoms misaligned (e.g. 2L AB hBN and hBN/SnS_2 hectorstructure in Figure 4.1 (a) and (c); both in-plane ϵ^{-1}-diag and in-plane ϵ-diag results have no difference from "Full matrix" results in the second and third columns of Figure 4.5).

4.3.3 Lattice mismatched hBN/SnS_2 interface

In order to benchmark the reciprocal-space linear-interpolation method introduced in Sec. 4.2.3 and Table 4.1, we consider the hBN/SnS_2 interface. A strain of 1.5% was applied to SnS_2 to match the hBN lattice constant with a 2:3 ratio in each direction of the plane (namely $2L^{SnS_2} = 3L^{hBN}$). By using a commensurate $\mathbf{q}$-point sampling for the two subsystems with a 2:3 ratio, a mapping of the $\mathbf{q}+\mathbf{G}$ vectors is possible and traditional methods for the substrate effect can be applied to produce a reference results for our new interpolation method (which, instead, will be used with an incommensurate $\mathbf{q}$-point sampling). We computed the GW band edges near the high symmetry point K of hBN on the SnS_2 substrate with the χ_{eff}-sum method at different $\mathbf{k}$-point samplings, as shown in Figure 4.6. The mesh for $\mathbf{q}$-point sampling was chosen to be identical to the $\mathbf{k}$-point sampling. Specifically, the reference calculations were performed with the hBN unit cell calculation with $20 \times 20 \times 1$ and $30 \times 30 \times 1$ $\mathbf{k}$-point sampling for the units cells of SnS_2 and hBN, respectively (this choice satisfies the 2:3 ratio for each inplane direction). The reference result obtained from the $\mathbf{q}+\mathbf{G}$ mapping is shown in Figure 4.6 (blue curve labelled by "$N_{\mathbf{k}}$ 20 mapping"). To apply our interpolation technique, it is not necessary to use commensurate grids and we compare instead the results for two different choices of the $\mathbf{q}$-point sampling for SnS_2. Specifically, in Figure 4.6 we show the results for the $22 \times 22 \times 1$ (red dashed line, "$N_{\mathbf{k}}$

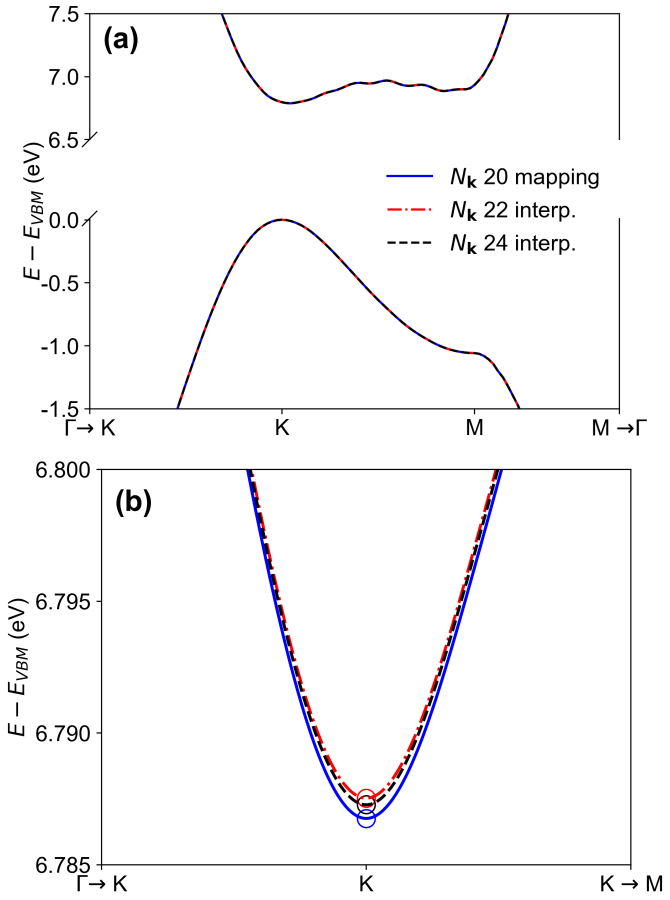

Figure 4.6: GW band structure of hBN at hBN/ stretched SnS_2 interface, referenced to valence band maximum (VBM) by using "χ_{eff}-sum" method. The blue solid line is computed with commensurate **q**-point sampling with the reciprocal space mapping approach, while the red/black dash line results are computed with incommensurate **q**-point sampling with the reciprocal-space linear-interpolation approach. a) shows both valence and conduction band edges; b) shows only the conduction band edge close to K.

22 interp.") and $24 \times 24 \times 1$ (black dashed line, "$N_{\mathbf{k}}$ 24 interp.") **q**-point grids, which do not allow for a mapping of the reciprocal space vectors and would be impossible to treat without our interpolation method. The results in Figure 4.6(a) show that the GW band structure with interpolation (red and black dashed lines) is nearly identical to the one based on the mapping (blue solid line), with differences smaller than 1 meV (as can be seen by zooming-in the conduction band edge in Figure 4.6(b)). This comparison demonstrates the excellent numerical accuracy of our linear interpolation method, which could have also been expected from the high quality of the interpolation in Figure 4.3.

Finally, we use our new interpolation method to better understand the effect of the strain on quasiparticle energies. In Figure 4.7, the blue curve corresponds to the the hBN

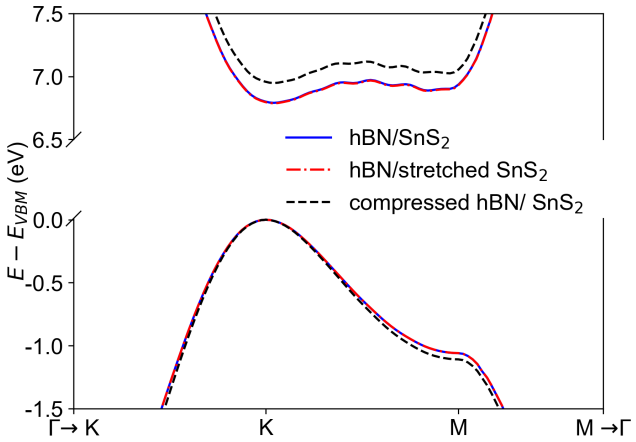

Figure 4.7: GW band structures of hBN with stretched SnS_2 substrate ("hBN/stretched SnS_2", red dash-dotted line), hBN with SnS_2 substrate with no strain ("hBN/SnS_2", blue solid line), compressed hBN with SnS_2 substrate ("compressed hBN/SnS_2", black dashed line), respectively.

bandstructure on the SnS_2 substrate without strain for either system as obtained from the interpolation scheme described above. These results are compared with those obtained for the interface by applying strain either to compress the hBN lattice parameter or to stretch SnS_2. We found that even a 1.5% compressive strain for hBN (black dashed line), the conduction band edge changes by 0.2 eV. Since we are focusing on the band structure of hBN states, the application of the strain to the SnS_2 substrate leads to negligible changes (red dash-dotted line). This result highlights the high sensitivity of quasiparticle band structures to strain.

We note that for a proof of principle and benchmark purpose, we chose systems with similar crystal symmetry, i.e. hexagonal lattice, in this work. However, our interpolation method can be applied to general interfaces with very different crystal symmetry, e.g. interface between hexagonal and rectangle lattices, as the example of hBN/phosphorene interface. This is not possible by using the previous $\mathbf{q} + \mathbf{G}$ mapping approach. Our reciprocal-space linear-interpolation method makes possible the GW calculations of interfaces composed by two materials with very different lattice parameters and symmetry, at the cost of primitive cell calculations only.

4.4 Computational details

4.4.1 Computational workflow

The workflow of GW calculations for the interface is structured as follows. We first compute the reducible polarizabilities (χ) for each subsystem separately and then we use them to obtain the effective polarizabilities ($\chi_{\text{eff}}^{m/s}$) using Eq. 4.2. In case of lattice mismatch between the two subsystems, the matrix elements of the polarizability χ of the substrates are obtained on the same reciprocal space grid of the material (ML hBN in the practical applications of this work) by using the linear interpolation method described above. Next we sum them to obtain χ^{tot} (i.e. the χ_{eff}-sum method).

Finally, in order to include the screening effect of the substrate on the material, the GW calculations are performed for the standalone hBN ML with the χ^{tot} obtained in the previous step. As we will discuss later, one can achieve further improvement for interfaces with strong hybridization by including corrections from ground state eigenvalues and wavefunctions of explicit interfaces.

4.4.2 Numerical parameters

In this work, we mainly focus on the quasiparticle energies of monolayer hBN/substrate interfaces as prototypical systems (where as substrates we will consider monolayer hBN itself and monolayer SnS_2). Density functional theory (DFT) ground state calculations based on the Perdew-Burke-Ernzerhof (PBE) exchange-correlation functional [74] have been performed using the open source plane-wave code Quantum ESPRESSO [30] with Optimized Norm-Conserving Vanderbilt (ONCV) pseudopotentials [40] and a 80 Ry wave function cutoff. From structural relaxation we obtained lattice constants of 2.51 (Å) and 3.70 (Å) for the free-standing monolayer (ML) hBN and SnS_2, respectively.

GW calculations with the Godby-Needs plasmon-pole approximation [33, 69] (PPA) were then performed using the Yambo [59] code. We chose PPA as a showcase for lower computational cost, but we can apply the same χ_{eff}-sum and reciprocal-space interpolation method with full frequency integration as well without technical difficulty, with more computational cost. Importantly, to the best of our knowledge, only PPA models or static COHSEX approximation were used in past calculations for the dielectric screening of substrates [133, 114, 10, 84, 132, 56, 62] and the obtained results were reasonably accurate. We used the same plasmon frequency for all calculations ω_p=27.2 eV and found little variation of the results (i.e. within 20 meV, with ω_p from 24.5 to 30 eV).

The distance between the nearest periodic repetitions along the vacuum direction was

set to be 20 Å. In order to speed up convergence with respect to vacuum sizes, a 2D Coulomb truncation technique was applied to dielectric matrices and GW self-energies [96]. For bilayer hBN systems, we set the interlayer distance to the bulk value of 3.33(Å) for both of the two different stacking configurations considered here (AA' and AB). The hBN/SnS_2 interlayer distance was set to 3.31 (Å) as obtained from structural relaxation with vdW-corrected functionals [36, 6].

For each free-standing monolayer ("ML") unit cell, the GW self-energy cutoff is set to 15 Ry. The number of bands is set to 1000 (1500) for hBN (SnS_2) unit cell calculations. The exchange self-energy cutoff is set to 40 Ry. We use a $30 \times 30 \times 1$ ($20 \times 20 \times 1$) $\mathbf{k}$-points sampling for ML-hBN (ML-SnS_2) unit cell calculations, unless specified.

GW calculations for the full explicit heterointerfaces have also been performed to obtain "exact" reference results to benchmark the different methods for the substrate screening effects (see Sec. 4.3.1). The computational parameters for the full interface are set to keep consistency between supercells and unit cell calculations.

4.4.3 Example of Reciprocal-space Linear interpolation method for arbitrarily mismatched interface

As we mentioned in the main text, our $\mathbf{q} + \mathbf{G}$ linear interpolation method works for arbitrarily mismatched interfaces. For example, hBN has a hexagonal Brillouin zone while phosphorene(BP) has a rectangle Brillouin zone, making it difficult to construct commensurate interfaces without large artificial strain. However, since $\mathbf{q} + \mathbf{G}$ interpolation does not require specific symmetry or periodicity between two systems at interfaces, we can still apply this method to this interface and compute their quasiparticle energies at GW approximation without any strain. For the test purpose, we use $36 \times 36 \times 1$ $\mathbf{q}$ point sampling for hBN and $15 \times 12 \times 1$ $\mathbf{q}$ point sampling for BP. The interlayer distance was set to 3.42 Å same as Ref. 9.

As shown in Figure 4.8 (a), we can see the different Brillouin zone (BZ) symmetry between hBN and BP, where the hBN irreducible Brillouin zone is triangle while the BP irreducible Brillouin zone is rectangle. Typically, constructing interface supercell with different symmetry requires relatively large artificial strain and large supercell sizes, which make GW calculations difficult and inaccurate. Since our interpolation method can be applied to general interfaces independent on the symmetry of two systems, we applied it to obtain the dielectric matrix of substrate BP at material hBN reciprocal space grids as shown in Figure 4.8 (a) in irreducible BZ and (b) full BZ. The dimension of the $\mathbf{q} + \mathbf{G}$ mesh is determined by the plane-wave cutoff of dielectric matrix. Although in (a) the

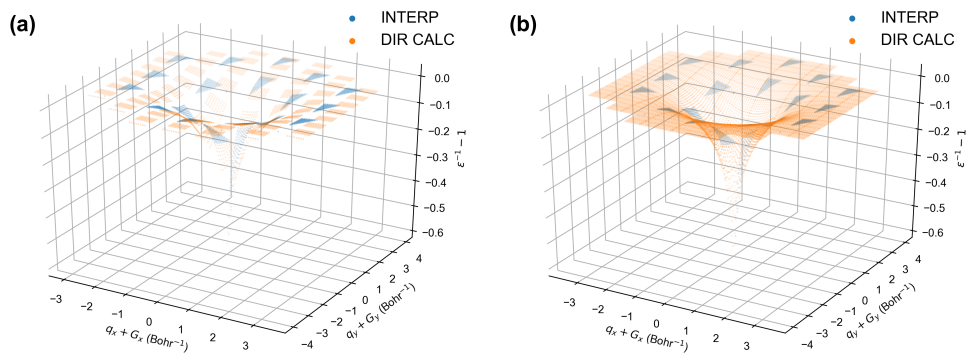

Figure 4.8: 3D plot of in-plane diagonal elements of $\epsilon^{-1} - \mathbb{1}$ of BP substrate, with $\mathbf{G}$ vector subset $(G_z, G'_z) = (0, 0)$ in a) $\mathbf{q}$ points sampling in irreducible Brillouin zone; b) $\mathbf{q}$ points sampling in full Brillouin zone. The $q_i + G_i, i = x, y$ are in-plane reciprocal space Cartesian coordinate in atomic unit (Bohr^{-1}). The orange points are directly computed data points ("DIR CALC") in BP substrate $\mathbf{q} + \mathbf{G}$ subspace, while the blue points are interpolated points ("INTERP") to (hBN) material $\tilde{\mathbf{q}} + \tilde{\mathbf{G}}$ subspace. Note that the orange points used for interpolating blue points in b) are beyond the first Brillouin zone of the substrate $\mathbf{q} + \mathbf{G}$ subspace.

interpolated points (blue) barely overlap with the direct calculated points (orange) due to their disparate symmetry, after extending the orange points to the full BZ by symmetry operations, the interpolated points fall exactly on the surface of the calculated points in Figure 4.8 (b). This validates our accurate interpolation method from substrate BP $\mathbf{q} + \mathbf{G}$ grids to material hBN $\tilde{\mathbf{q}} + \tilde{\mathbf{G}}$ grids. Following the same steps as proposed in main text by using χ_{eff}-sum method for substrate dielectric screening, we predict the direct band gap of hBN reduce by 0.90 eV due to substrate screening effects from BP.

4.4.4 Computational Details for GW Calculations of Explicit Interfaces

As we discussed in the main text, we used explicit interfaces' GW calculations as references to benchmark our methods for substrate dielectric screening, which only require unit cell calculations. For the hBN/SnS_2 interface, we used a (3×3) hBN/(2×2) SnS_2 supercell, by straining SnS_2 by 1.5% for the interface lattice matching. As we discussed in Section IV.C of the main text, we do not need to apply strain at this interface if we apply our reciprocal-space linear-interpolation method.

Figure 4.9 shows convergence tests of GW quasi-particle band edges and band gaps of the hBN/SnS_2 interface with respect to number of bands and cutoff energy for dielectric matrices and GW self-energy. Note that the conduction band minimum (CBM) and the valence band maximum (VBM) of the interface are from SnS_2 and hBN, respectively.

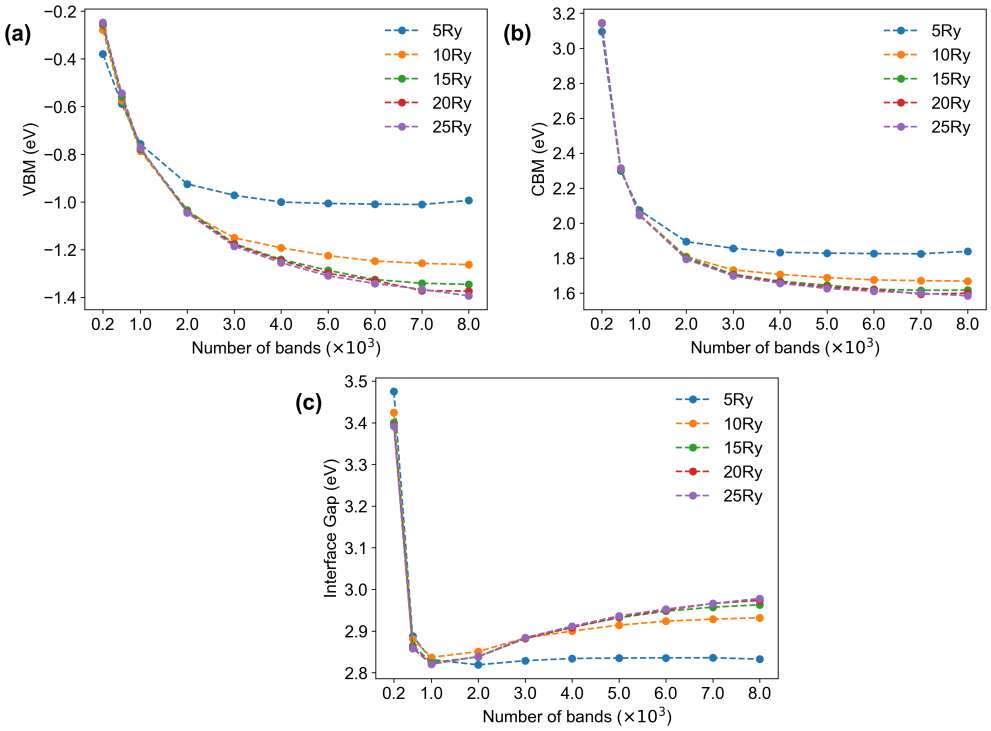

Figure 4.9: The convergence of energy cutoff and number of bands for GW self-energies and dielectric matrices, for a) VBM at (3×3)hBN/$(2\times2)SnS_2$ interfaces, referenced to the VBM at the ground state; b) CBM at the interface; c) the band gap at the interface.

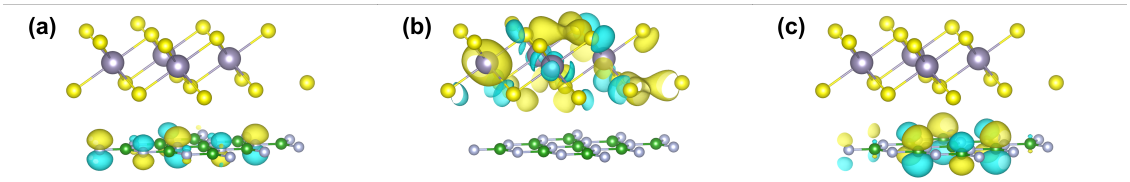

Figure 4.10: Charge density distribution with an isosurface value of 1.7×10^{-3} e/Bohr^3 of a) VBM at hBN/SnS_2 interface b) CBM at hBN/SnS_2 interface c) CBM belongs to hBN subsystem at hBN/SnS_2 interface.

Their corresponding electronic wavefunctions are shown in Figure 4.10a and Figure 4.10b. However, in order to compare with the substrate screening methods where we focus on the change of hBN band gaps due to substrates, we identify the CBM at K of hBN at the interface (its electronic wavefunction is shown in Figure 4.10c) and use the direct band gap at K of hBN at the interface as a reference.

When testing the convergence of energy cutoff and band number in GW calculations, we choose relative coarse **k**-point grids, since their convergence is uncorrelated with **k**-point convergence [27]. We tested 5 to 25 Ry energy cutoff for the interface band edge

convergence. For each energy cutoff, we tested 200 to 8000 bands included in the GW self-energy for the interface calculations.

Based on the convergence of interface band edge in Figure 4.9a and b and direct band gap in Figure 4.9c, we choose 15 Ry energy cutoff and 6000 bands ($\approx$ 200 eV above the CBM) as converged parameters.

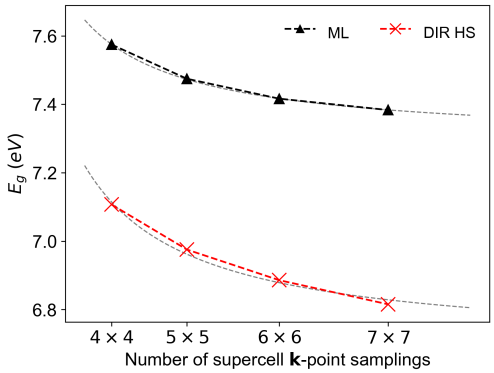

Figure 4.11: GW **k**-point convergence of direct band gap of hBN at monolayer and interface with SnS_2. "ML" with the black triangle denotes the direct band gap of free-standing ML hBN at K. "DIR HS" with red cross denotes direct GW calculations of explicit (3×3)hBN/$(2\times2)SnS_2$ interfaces. The dashed line represents the fitting with $E_g = A/N_k^2 + B$, where N_k is number of k points. The fitted value of B has less than 0.1 eV difference from the computed results at 7×7.

Finally, using the converged energy cutoff and bands above, we further test the convergence of **k**-point samplings for a) free-standing ML hBN direct gap ("ML") and b) direct gap of hBN at hBN/SnS_2 interface in Figure 4.11. At fixed bands and cutoff, we performed k-point convergence tests from 4×4 to 7×7 for (3×3)hBN/$(2 \times 2)SnS_2$ interface supercell in Figure 4.11. The **q**-point samplings are set to be identical to **k**-point samplings. Compared with fitted curve [124] marked as gray dashed line, the result obtained at 7×7 for 3×3 hBN supercell or (3×3)hBN/$(2 \times 2)SnS_2$ interface is within 0.1 eV difference from the extrapolated results from fitting. And the band gap of hBN by 30×30 **k**-point sampling for the unit cell is only 10 meV difference from 7×7 for 3×3 supercell.Therefore we choose the 7×7 **k**-point for the 3×3 hBN supercell (i.e. 21×21 for hBN unit cells) as the converged parameter for the interfaces. The error bar for the monolayer calculation is around 10 meV but for the interface, it is within 0.1 eV.

Note that we applied 2D Coulomb truncation [96] along the vacuum direction to avoid spurious periodic interactions and speed up the vacuum convergence. In order to keep consistency between free-standing monolayer ("ML") and direct heterostructure ("DIR HS") interface calculations, we set the GW energy cutoff to be the same as interface i.e.

15Ry. The bands included in the ML calculations are set to a similar energy range (about 200 eV above the CBM), consistent with the DIR HS calculations above.

4.5 Conclusion

In this work, we theoretically and numerically examined the existing methods to approximate substrate dielectric screening effect on quasiparticle energies, through hBN heterostructures as prototypical examples. We clarified the theoretical equivalence between the sum of effective reducible polarizability approach (χ_{eff}-sum) and sum of irreducible polarizability of interface systems (χ_0-sum), at the RPA level. We numerically compared the GW calculations of 2D interfaces with several approximations, and found excellent agreements between χ_{eff}-sum and the explicit interface calculations. Further improvement can be achieved by including the ground state corrections of eigenvalues (and wavefunctions) from explicit interfaces. We further evaluated the importance of non-diagonal elements of ϵ and ϵ^{-1} from substrates on quasiparticle energies of 2D interface. Most importantly, we developed an accurate reciprocal-space linear-interpolation technique for arbitrarily lattice-mismatched interfaces, which can be used to compute the interface polarizability for GW quasiparticle energies without any artificial strain, at the cost of only primitive cell calculations.

Chapter 5

Substrate Effect on Excitonic Shift and Radiative Lifetime

5.1 Introduction

Due to reduced dimensionality, two-dimensional (2D) materials and their heterostructures have shown emerging optical properties, such as strong light-matter interaction and giant excitonic binding energy [20], distinct from the three-dimensional counterparts. Promising applications have been demonstrated in many areas, such as opto-spintronic devices [123, 138] and quantum information technologies [41, 111]. Experimentally, growth of 2D materials, achieved through physical epitaxy or chemical vapor deposition (CVD), is typically supported on a substrate [65]. Similarly, the optical measurements, such as photoluminescence and absorption spectra, are often performed on top of substrates or sandwiched by supporting substrates. In general, the optoelectronic properties of 2D materials can be strongly modified by environmental dielectric screening. For example, their fundamental electronic gap and exciton binding energy can be significantly reduced at presence of substrates when forming heterostructures [122, 114].

An interesting experimental observation is that in the presence of environmental dielectric screening (including increasing the number of layers of 2D materials), the 2s (second) exciton peaks shift strongly, but the 1s (first) exciton peaks stay relatively unchanged [20, 114, 117, 86]. Yet, the physical origin of such non-rigid shift of excitonic peaks due to substrate screening has not been revealed and requires careful investigation. Its quantitative prediction is also crucial for correct interpretation and utilization of experimental measurement data. For example, the energy difference between 1s and 2s absorption peaks Δ_{12} in the presence of different substrate screening has been used to estimate electronic

band gaps in optical measurements [86, 117], although its underlying assumption still requires careful justification.

Physically, the exciton peak shift due to substrate screening is determined by changes both from the electronic gap and exciton binding energy, which compete with each other. Therefore, theoretical methods such as many-body perturbation theory (MBPT, GW approximation and solving Bethe-Salpeter equation (BSE)) including electron correlation and electron-hole interactions are necessary to accurately describe both electronic gaps and exciton binding energies [77]. In order to study the effect of various substrates at such level of theory, our recent development on substrate dielectric screening from MBPT [39] will make these calculations computationally tractable. There we developed a reciprocal linear-interpolation method, which interpolates the dielectric matrix elements from substrates to materials at the entire $\vec{q} + \vec{G}$ space, thus completely removes the constraint on symmetry and lattice parameters of two interface systems. In this work we will further apply this method to study the substrate effects on excitonic excitation energies and radiative lifetime.

Previous theoretical studies described the exciton energy spectrum of free-standing 2D materials with relative simple models, e.g. 2D Wannier exciton Rydberg series [67] or linear scaling between exciton binding energy and electronic band gap [22, 47]. The environmental screening induced exciton peak shifts have been discussed with semi-infinite dielectric models [21]. The applicability of these models to explain the excitonic physics of 2D heterostructures or multilayer systems is unclear and requires examination. On the other hand, past first-principle work mostly focused on the substrate effects on first exciton peak position (optical gap) and electronic band gaps [114]. The question of the origin of nonrigid shift of excitonic peaks due to substrate screening and whether there is any universal scaling relation have not been answered to our best knowledge. Furthermore, how the substrates affect exciton radiative lifetime, a critical parameter determining quantum efficiency in optoelectronic applications, has rarely been studied before. Understanding how radiative lifetime changes in the presence of substrate screening will provide important insights to experimental design of optimal 2D interfaces.

This work was published in the Emerging Leaders issue of *J. Phys.: Condens. Matter* as Guo *et al.*, *J. Phys.: Condens. Matter* **33**, 234001 (2021) [38].

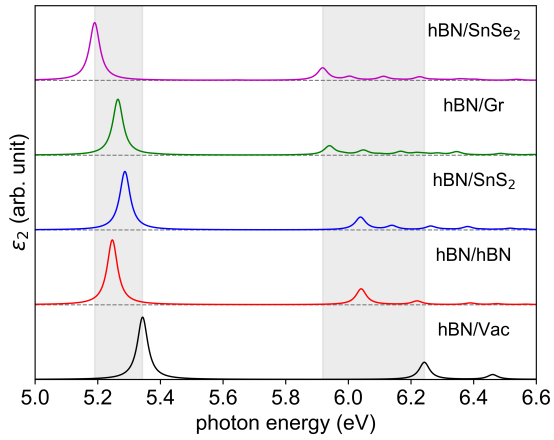

Figure 5.1: Absorption spectra obtained by solving BSE (with e-h interaction) for monolayer hBN interfacing with various substrates. The curves from the bottom to the top are for 1) free-standing hBN (hBN/Vac) 2) hBN/hBN 3) hBN/SnS_2 4) hBN/Graphene(Gr) 5) hBN/$SnSe_2$ heterostructures. Curves are vertically displaced for clarity.

5.2 Results and discussions

5.2.1 Substrate screening effect on optical excitation energy of hBN

Hexagonal boron nitride (hBN) has drawn significant attentions recently due to its potentials as host materials for single photon emitters [61, 111] and spin qubits [34, 113] for quantum information science applications. Rapid progress has been made both experimentally and theoretically [127, 104, 124, 103, 97]. The related optical measurements are often performed on top of substrates, whose effects have not been carefully examined. We use hBN as a prototypical example to examine how optical excitation energies are changed in the presence of substrates. We obtain the optical excitation energies and absorption spectra by solving the BSE (with electron-hole) and Random Phase approximation (RPA) calculations (without electron-hole interactions), with GW quasiparticle energies as input.

Figure 5.1 shows the BSE calculations of monolayer hBN with various substrates, including $SnSe_2$, graphene, SnS_2, hBN as well as without substrate (interfacing with vacuum). The 1s absorption peak shifted little referenced to the free-standing hBN (black curve) i.e. < 0.2 eV but the 2s absorption peak shifts nearly twice compared to the first peak. This trend obtained from our BSE calculations is fully consistent with the experimental observations mentioned in the introduction [20].

In contrast, Figure 5.2 shows the RPA spectra of hBN with various substrates using GW quasiparticle energies exhibit a nearly-rigid shift to a lower energy (compared to free-standing hBN). The red shift is mainly due to the reduction of electronic band gap in

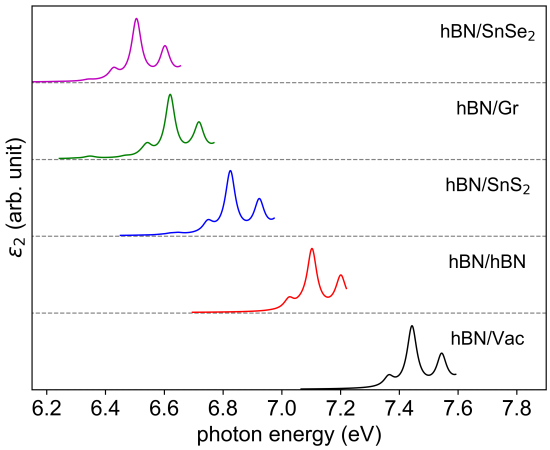

Figure 5.2: Absorption spectra at RPA with GW quasiparticle energies (without e-h interaction). The curves from the bottom to the top are for 1) free-standing hBN (hBN/Vac) 2) hBN/hBN 3) hBN/SnS_2 4) hBN/Graphene(Gr) 5) hBN/$SnSe_2$ heterostructures. Curves are vertically displaced for clarity.

the presence of substrate screening. This rigid shift may be qualitatively explained by the independence of k-point for electronic band structure under Born approximation [21, 117], which has been reported for 2D semiconductors (e.g. WS_2) [117].

In general, we find the reduction of quasiparticle band gaps due to substrates increases with stronger substrate dielectric screening. However, a simple dielectric constant picture is insufficient to describe low dimensional systems. Specifically, we show the in-plane diagonal elements of dielectric matrices in Figure 5.3. For example, comparing with the $SnSe_2$ substrate (purple dots), the graphene substrate (green dots) has a stronger dielectric screening at a small momentum transfer region close to zero, and a weaker dielectric screening at a larger momentum transfer region. As a result, the reduction of band gap with the $SnSe_2$ substrate is larger than the one with the graphene substrate although graphene is closer to a metallic system at the Dirac cone than $SnSe_2$. Therefore, fully first principle calculations are required to get reliable prediction of screening effects by various substrates.

5.2.2 1s and 2s exciton binding energy change with substrate screening

The difference between BSE excitation energies (E_S) and electronic band gaps E_g defines exciton binding energy E_b for excitonic state S:

$$E_b(S) = E_g - E_S. \tag{5.1}$$

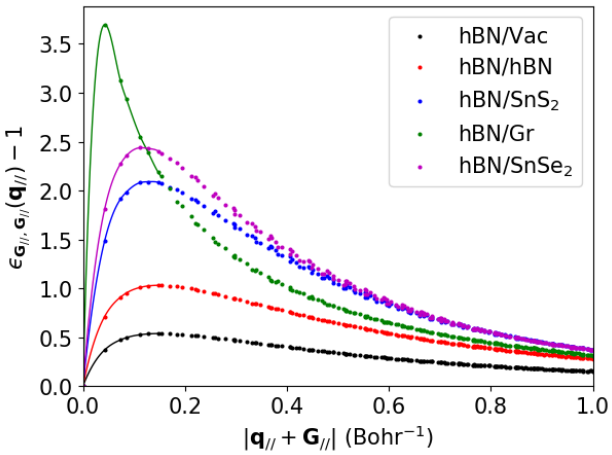

Figure 5.3: The in-plane diagonal elements of RPA dielectric matrix $\epsilon_{\mathbf{G}_{||},\mathbf{G}_{||}}(\mathbf{q}_{||})$-1 as a function of absolute values of in-plane momentum transfer $\mathbf{q}_{||} + \mathbf{G}_{||}$ for different hBN/substrate interfaces.

We found the proportionality between 1s and 2s exciton binding energies across different substrates falls into a linear relation (i.e. with a slope of 0.73 for $E_b(2s)/E_b(1s)$), as shown in Figure 5.4.

To understand the physical meaning of this linear scaling obtained by solving BSE, we compare our results with the previous 2D hydrogen model of excitons [20, 67], which has been used to interpret the exciton energies of free-standing 2D materials. Here we will test the applicability of this model for substrate screening effect on 2D excitons. In this model, we express the 2D dielectric function $\epsilon(\mathbf{q})$ as $\epsilon(\mathbf{q}) = 1 + 2\pi\alpha\mathbf{q}$, where α is the 2D polarizability. The exciton binding energies of nth 2D Rydberg-like excitonic state [135] ($E_b^{\text{Model}}(n)$) can be expressed as:

$$E_b^{\text{Model}}(n) = \frac{\mu}{2(n-\frac{1}{2})^2\epsilon_n^2}, \tag{5.2}$$

where μ is the exciton reduced mass and ϵ_n is the effective dielectric constant for nth excitonic state, defined as [67]:

$$\epsilon_n = \frac{1}{2}(1 + \sqrt{1 + \frac{32\pi\alpha\mu}{9n(n-1)+3}}). \tag{5.3}$$

Further simplification [67, 47] of Eq. 5.2 with Eq. 5.3 gives 2D exciton binding energy E_b^{Model} independent of exciton reduced mass μ as follows:

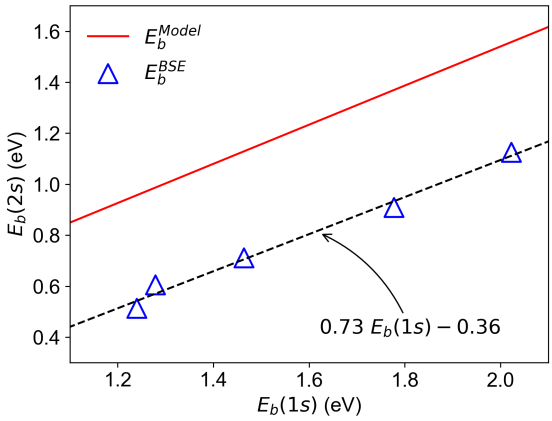

Figure 5.4: Linear scaling between exciton binding energy of 1s state $E_b(1s)$ and 2s state $E_b(2s)$. The blue triangles are first-principles results by solving BSE. The dashed black line is the linear fit to the blue triangles. The red line is computed from the 2D hydrogen model for exciton binding energies [67] based on Eq. 5.4. The blue triangle points from right to left are 1) free-standing hBN (hBN/Vac) 2) hBN/hBN 3) hBN/SnS_2 4) hBN/Graphene(Gr) 5) hBN/$SnSe_2$ heterostructures.

$$E_b^{Model}(n) \approx \frac{9n(n-1)+3}{16\pi(n-\frac{1}{2})^2} \cdot \frac{1}{\alpha}. \tag{5.4}$$

From Eq. 5.4, we have $E_b^{Model}(1s) \approx 3/(4\pi\alpha)$ and $E_b^{Model}(2s) \approx 7/(12\pi\alpha)$. The ratio between $E_b(2s)$ and $E_b(1s)$ is a constant 0.78 from this simplified model. Figure 5.4 shows the linear scaling between 1s and 2s exciton binding energies of monolayer hBN when changing its substrates. The scaling behavior by the model in Eq. 5.4 (red curve) is in qualitative agreement with our GW/BSE results (blue triangles), i.e. both of which have a linear relation between 2s and 1s exciton binding energies, with a ratio of less than one (Model: 0.78; GW/BSE: 0.73), corresponding to the slope. This implies the change of 1s E_b is larger than the change of 2s E_b due to substrate screening, with a constant ratio while varying the substrate materials. Figure 5.4 also shows a constant shift between the first-principles scaling and the model one. This discrepancy independent of specific screening environment may come from the limitation of 2D hydrogen model, i.e. either the strict 2D limit of $\epsilon(\mathbf{q})$ is unrealistic considering the finite thickness of materials, or hBN has tighter-bounded excitons [26], deviated from 2D Wannier excitons assumed in previous 2D hydrogen model. Note that the explicit form of Eq. 5.4 and related linear scaling behavior is based on strict 2D limit of Eq. 5.2, which is better to describe the interface with relatively small thickness, e.g. heterostructures formed by atomically thin materials. We anticipate that this simplified model may become inappropriate for interface systems with large

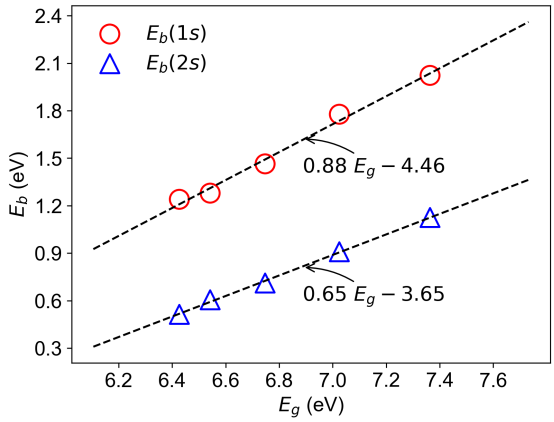

Figure 5.5: Linear scaling between 1s and 2s exciton binding energy E_b and quasiparticle direct band gaps E_g computed from GW and BSE. The data points from right to left are (1) free-standing hBN, (2)(2L-AA′) hBN/hBN (3) hBN/SnS_2, (4) hBN/Graphene(Gr), (5) hBN/$SnSe_2$ results with effective polarizability approach ('χ_{eff}-sum' method).

thickness, especially for systems with high dielectric semi-infinite substrates [88].

5.2.3 Substrate induced linear scaling relation between E_b and E_g

The exciton peak positions are determined by both the exciton binding energies and electronic band gaps, which have opposite trends while increasing substrate screenings. The relationship between these two quantities was studied for free-standing 2D systems [22, 47], where $E_b \approx \frac{1}{4}E_g$ across a wide range of 2D materials.Yet, no investigation on their relationship when varying substrates has been carried out.

In Figure 5.5, we show the calculated electronic gap (E_g) and exciton binding energy of 1s (red circle) and 2s (blue triangle) (E_b) for monolayer hBN at various substrates. Our first-principle results show a linear scaling between exciton binding energy E_b (1s peak position) and quasiparticle electronic band gap E_g due to substrate screening, with a slope nearly close to one (0.88 in Figure 5.5, linear fitting the computed data (red circles) with a black dashed line). This indicates that the changes of 1s exciton binding energy ΔE_b and electronic gaps ΔE_g due to substrate screening are largely canceled out. Therefore, the first exciton peak (1s) is at a relatively stable position, insensitive to the environmental screening. This explains the experimental and theoretical results in Figures 5.1 and 5.6, where the first excitonic peak has rather small shifts with changing environmental screening.

This linear scaling is significantly different from the 1/4 scaling across different monolayer 2D materials [47, 22]. Physically, the scaling between E_b and E_g due to substrate screening has very different nature from the one of free-standing monolayer semiconductor.

The environmental screening can be approximately described by classical electrostatic potential of dielectric interface [21, 117], which gives a similar reduction on quasi-particle band gaps and exciton binding energies by 2D hydrogen model (linear scaling slope ≈ 1).

On the other hand, the scaling between 2s binding energy and electronic gap is significantly smaller (0.65) than unity, which indicates the change of 2s exciton binding energy is a lot smaller than the electronic gap with increasing substrate screening. Therefore, the 2s exciton peak position is dominated by the change of electronic gap, which red shifts the spectra with increasing substrate screening (i.e. from vacuum to interfacing with $SnSe_2$ in Figure 5.6). This stronger red shift of 2s exciton peak than 1s is also expected from the smaller reduction of 2s binding energy with increasing substrate screening in Figure 5.4.

5.2.4 Layer dependence of WS_2 optical spectra

To further validate our method for substrate screenings on optical properties, we calculate the optical spectra from one to three-layer WS_2 with the GW/BSE method, then compare with recent experimental results [20]. The multi-layer calculations are performed with "χ_{eff}-sum" method introduced earlier [39], which is computationally efficient and properly includes interlayer Coulomb interactions from first-principles.

As shown in Figure 5.6, we find the position of the first peak (1s, blue dot) is nearly unchanged (shifted within 20 meV) when increasing the number of layers, while the position of the second peak (2s, red dot) shifts over 100 meV. The calculated results with blue (1s) and red dots (2s) are compared with the experimental results (1s, blue triangle) and (2s, purple triangle). From 1L to 4L, the agreements between experiments and theory are nearly perfect, which validate the accuracy of our methods. Meanwhile, the calculated electronic gaps (black cross) are also shown in Figure 5.6b, with a strong reduction as increasing the number of layers, in sharp contrast to the nearly unchanged optical gaps (1s exciton energies, red dots).

5.2.5 Exciton lifetime in the presence of substrates

Zero temperature exciton lifetime

Environmental screening due to substrates can also significantly modify the exciton lifetime τ, which is a critical parameter that determines quantum efficiency. The radiative rate γ (inverse of lifetime $1/\tau$) based on the Fermi's Golden rule can be defined as follows [125, 72]:

$$\gamma(\boldsymbol{Q}_{\text{ex}}, \boldsymbol{q}_{\text{L}}, \lambda) = \frac{2\pi}{\hbar} \left| \left\langle G, 1_{\boldsymbol{q}_{\text{L}}\lambda} \middle| H^{\text{int}} \middle| S(\boldsymbol{Q}_{\text{ex}}), 0 \right\rangle \right|^2$$

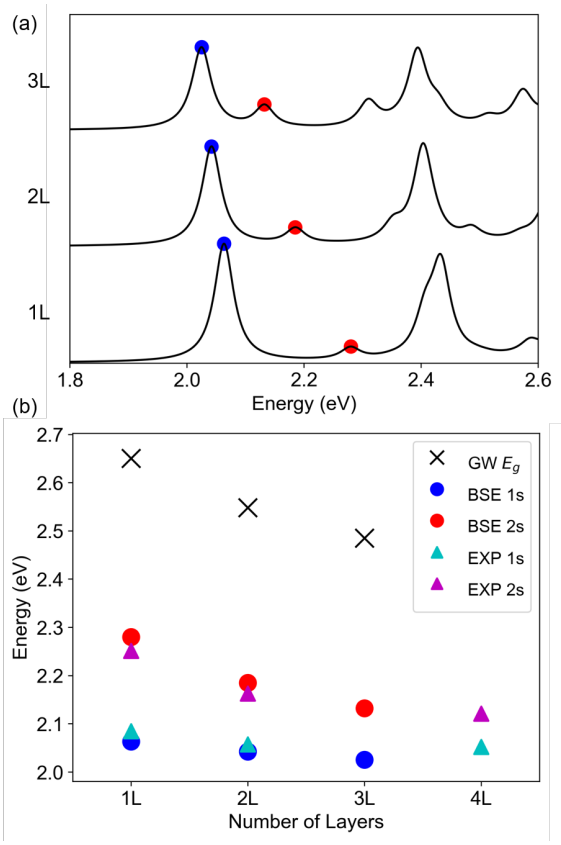

Figure 5.6: Layer dependence of optical properties of WS_2 a) calculated BSE absorption spectra for 1 layer(1L) $\rightarrow$ 3 layers (3L) WS_2 b) electronic gaps and optical excitation energies from GW and BSE, in comparison with experimental exciton energies [20].

$$\times \delta(E(\boldsymbol{Q}_{ex}) - \hbar c q_L), \tag{5.5}$$

where G denotes the ground-state wavefunction, $S(\boldsymbol{Q}_{ex})$ the excited state, $E(\boldsymbol{Q}_{ex})$ the excitation energy, $\boldsymbol{q}_L$ photon wave-vector, λ photon polarization direction and $\boldsymbol{Q}_{ex}$ exciton wave-vector. Then the radiative decay rate can be defined as the summation of each photon mode:

$$\gamma(\boldsymbol{Q}_{ex}) = \sum_{\boldsymbol{q}_L \lambda=1,2} \gamma(\boldsymbol{Q}_{ex}, \boldsymbol{q}_L, \lambda); \tag{5.6}$$

the corresponding radiative lifetime can be defined as the inverse of rate $\gamma(\boldsymbol{Q}_{ex})$. Furthermore, the radiative decay rate can be separated into two parts:

$$\gamma(\boldsymbol{Q}_{ex}) = \gamma_0 Y(\boldsymbol{Q}_{ex}), \tag{5.7}$$

Sub	Ω/eV	$\mu_S^2 \cdot \frac{8\pi}{V}$/eV	τ_0/fs
Vac	5.34	0.788	30.9
hBN	5.25	0.818	30.3
SnS_2	5.29	0.738	33.3
Gr	5.26	0.706	35.0
$SnSe_2$	5.19	0.729	34.3

Table 5.1: Monolayer hBN 1s exciton lifetime with different substrates at zero temperature, comparing with the free-standing one (Vac). V is the volume of unit cell.

Sub	Ω/eV	$\mu_S^2 \cdot \frac{8\pi}{V}$/eV	τ_0/fs
Vac	6.24	0.218	95.6
hBN	6.04	0.201	107.1
SnS_2	6.04	0.162	132.5
Gr	5.94	0.120	182.8
$SnSe_2$	5.92	0.159	138.1

Table 5.2: Monolayer hBN 2s exciton lifetime with different substrates at zero temperature, comparing with the free-standing one (Vac). V is the volume of unit cell.

where γ_0 is the exciton decay rate at $\boldsymbol{Q}_{\text{ex}} = 0$ and $\Upsilon(\boldsymbol{Q}_{\text{ex}})$ has exciton wave-vector dependence. Note that the $\boldsymbol{Q}_{\text{ex}}$ dependence will be only important to the exciton lifetime at finite temperature [125]. Therefore the zero-temperature lifetime is simply $1/\gamma_0$.

Specifically for two-dimensional exciton lifetime at zero temperature, we have [125]

$$\gamma_0 = \frac{8\pi}{cA} \cdot \Omega \mu_S^2, \tag{5.8}$$

where Ω is the exciton energy, A is the unit cell area, and μ_S^2 is the module square of dipole matrix elements [125].

The computed 1s and 2s exciton lifetimes of monolayer hBN on various substrates at zero temperature are shown in Table 5.1 and Table 5.2 respectively. The effect of substrate screening on τ_0 comes from the quench of oscillator strength (or dipole moment μ_S^2) and the red-shift of exciton energy, both of which increase the lifetime. In Table 5.1 and 5.2, μ_S^2 are reduced by a similar amount between 1s and 2s excitons with increasing substrate screening; however, the relative proportion of reduction is much larger in 2s exciton due to

Mat	τ_0/fs	τ_{RT}^{EM}/ps	τ_{RT}^{EXP}/ps
ML WS_2	334	923	806 [136]

Table 5.3: Monolayer (ML) WS_2 1s exciton radiative lifetime compares with experiment result. The zero temperature lifetime (τ_0) is directly computed based on BSE exciton energy and dipole moments. The room temperature lifetime (τ_{RT}^{EM}) is calculated with effective mass approximation with exciton effective mass $m_{exc} = 0.59$ [102]. The reference experiment result is obtained from room temperature time-resolved photoluminescence (TRPL) spectroscopy [136] .

its much weaker μ_S^2 than 1s exciton. This results in stronger increase in 2s exciton lifetime (i.e. increased by 30 ~ 80 fs) in Table 5.2. Instead, 1s exciton lifetime is rather insensitive to the substrate screening in Table 5.1.

Finite temperature exciton lifetime

The radiative exciton decay rate $\gamma(T)$ at finite temperature T can be calculated by the thermal average of all accessable excitonic states as follows:

$$\gamma(T) = \frac{\int d\boldsymbol{Q}_{ex} e^{-E(\boldsymbol{Q}_{ex})/k_B T} \gamma(\boldsymbol{Q}_{ex})}{Z} \tag{5.9}$$

$$Z = \int d\boldsymbol{Q}_{ex} e^{-E(\boldsymbol{Q}_{ex})/k_B T}, \tag{5.10}$$

where $E(\boldsymbol{Q}_{ex})$ is the exciton energy dispersion as a function of exciton wave-vector $\boldsymbol{Q}_{ex}$. Since a constant shift of $E(\boldsymbol{Q}_{ex})$ does not change the expression of rate γ, we will use $E(\boldsymbol{Q}_{ex}) - E_0$ to replace $E(\boldsymbol{Q}_{ex})$ in all later discussions, where $E_0 = E(\boldsymbol{Q}_{ex} = 0)$ is the lowest exciton energy. As the integration of Eqs. 5.9-5.10 requires the dispersion of exciton energy $E(\boldsymbol{Q}_{ex})$, we use the effective mass approximation for exciton energy dispersion.

First, we compute the room temperature (300K) exciton radiative lifetime of monolayer (ML) WS_2 to compare with experimental lifetime [136]. The effective mass approximation for exciton dispersion is defined as $E(\boldsymbol{Q}_{ex}) = E(\boldsymbol{Q}_{ex} = 0) + \hbar^2 Q_{ex}^2 / 2m_{exc}$, where m_{exc} is the exciton effective mass. m_{exc} is chosen to be the summation of electron and hole effective mass, which was shown adequate for Wannier excitons [60]. The electron (m_e) and hole (m_h) effective mass are from GW band structure results [102] ($m_e = 0.27, m_h = 0.32$). Our calculated lifetime at room temperature is 923 ps for monolayer WS_2, in excellent agreement with experimental lifetime 806 ps [136] as shown in Table 5.3.

We then apply the same methodology to compute the exciton radiative lifetime for monolayer hBN with various substrates at finite temperature, as shown in Table 5.4. We

Sub	τ_0/fs	τ_{RT}^{EM}/ps
Vac	30.9	33.3
hBN	30.3	32.6
SnS_2	33.3	35.8
Gr	35.0	37.7
SnS_2	34.3	37.0

Table 5.4: τ_0 is the monolayer hBN (1s) exciton lifetime with diffient substrate at zero temperature (0K), while τ_{RT}^{EM} is room temperature lifetime with effective mass approximation at 300K compare with free-standing (Vac).

find within the effective mass approximation, the room temperature exciton lifetime τ_{RT}^{EM} is much longer ($2 \sim 3$ orders) than the zero temperature lifetime τ_0. To confirm the exciton lifetime of monolayer hBN with substrates in Table 5.4 at finite temperature, future experimental work will be necessary.

5.3 Computational Details

The ground state calculations are performed based on Density functional theory (DFT) with the Perdew-Burke-Ernzerhof (PBE) exchange-correlation functional [74], using the open source plane-wave code QuantumEspresso [30]. We used Optimized Norm-Conserving Vanderbilt (ONCV) pseudopotentials [40] and a 80 Ry wave function cutoff for most systems except WS_2 (60 Ry). For monolayer WS_2, spin-orbit coupling is included through fully relativistic ONCV pseudopotentials. The interlayer distance and lattice constants of hBN interfaces and multiplayer WS_2 are obtained with PBE functionals with Van der Waals corrections [36, 6].

In this paper, the quasiparticle energies and optical properties are calculated with many-body perturbation theory at GW approximation and solving Bethe-Salpeter equation respectively, for hBN/substrate interfaces and multi-layer WS_2. To take into account the effect of substrates, we use our recently developed sum-up effective polarizability approach (χ_{eff}-sum) [39], implemented in a postprocessing code interfacing with the Yambo-code [59]. Briefly, we separate the total interface systems into subsystems [133] and perform GW/BSE calculations for monolayer hBN or WS_2 including the environmental screenings by the χ_{eff}-sum method. For lattice-mismatched interfaces, we use our reciprocal-space linear interpolation technique [39] to interpolate the corresponding ma-

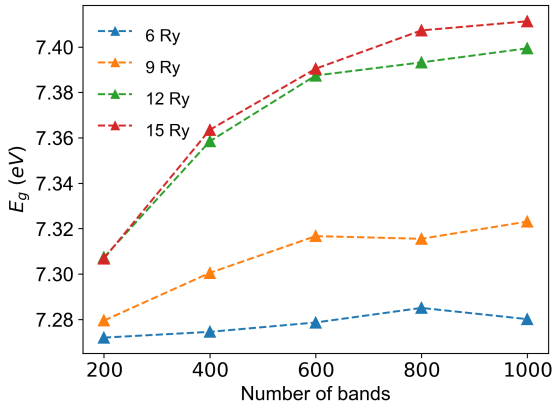

Figure 5.7: The convergence of GW energy cutoff and number of bands for the GW quasiparticle gap of monolayer hBN, computed at a fixed **k**-point $21 \times 21 \times 1$. We chose GW energy cutoff 15 Ry and number of bands 1000 for hBN results in the main text.

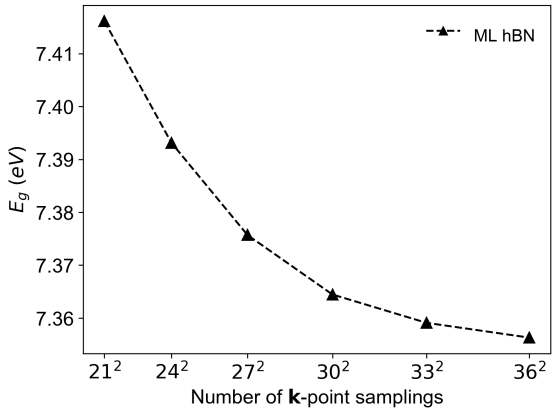

Figure 5.8: The convergence of **k**-point samplings of GW quasiparticle gaps of monolayer hBN at GW energy cutoff 15Ry and 1000 bands. We chose **k**-point sampling $36 \times 36 \times 1$ for hBN results in the main text.

trix elements from substrate to materials $\vec{q} + \vec{G}$ space before summing up the subsystems' effective polarizabilities.

In order to speed up convergence with respect to vacuum sizes, a 2D Coulomb truncation technique [95] was applied to GW and BSE calculations. The k-point convergence of quasiparticle gaps and BSE spectra for monolayer hBN is shown in SI Figure 2 and 3, where we show $36 \times 36 \times 1$ k points converge up to 20 meV, which was adopted for other calculations.

The structural parameters of hBN interfaces and multiplayer WS_2 are obtained with PBE functionals with van-der Waals corrections [36, 6]. The lattice constants after geometry relaxation are 2.51, 3.70, 3.87, 2.47 (Å) for the free-standing monolayer (ML) hBN, SnS_2,

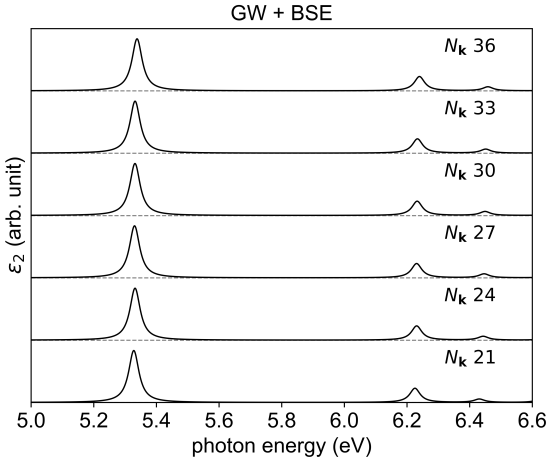

Figure 5.9: The convergence of **k**-point samplings of absorption spectra for monolayer hBN at BSE Hamiltonian cutoff energy 10 Ry. The **k**-point samplings are always chosen to be the same between GW and BSE, with GW energy cutoff 15Ry and 1000 bands.

$SnSe_2$ and graphene, respectively. For bilayer hBN, we set the interlayer distance to the bulk value of 3.85 (Å) for the AA' stacking configuration considered here. The relaxed hBN/SnS_2, hBN/$SnSe_2$, hBN/graphene interlayer distances were obtained as 3.31, 3.22, 3.11 (Å). For monolayer and few-layer WS_2, the lattice constant 3.19 (Å) and the stacking-layer distance 3.01 are chosen to be the same as those of fully relaxed bulk WS_2 structure.

In order to speed up convergence with respect to vacuum sizes, a 2D Coulomb truncation technique was applied to dielectric matrices and GW and BSE calculations [96]. The distance between the nearest periodic repetitions along the vacuum direction was set to be 20 Å for monolayer hBN, SnS2, graphene, and 35.5 Å for monolayer WS_2. The large vacuum is needed when we sum up the dielectric screening from different subsystems. The convergence of number of bands and cutoff for the GW quasiparticle gaps of monolayer hBN is shown in Figure 5.7, with a fixed k-point grid of $21\times21\times1$. We used 1000 bands and 15 Ry for the dielectric matrix and GW self-energies for our results in the main text. We then show the k-point convergence of quasiparticle gaps of monolayer hBN in Figure 5.8,where we show $21\times21\times1$ is already converged up to 50 meV. We used the most converged parameter $36\times36\times1$ k-point for the final calculations. The convergence of absorption spectra at GW+BSE of monolayer hBN is shown in Figure 5.9, where we show that at $36\times36\times1$ k-point the spectra are converged within 20 meV.

For GW/BSE calculations of other systems, we used $36 \times 36 \times 1$ k-points sampling for graphene and WS_2, $24 \times 24 \times 1$ for SnS_2 and $SnSe_2$ unit cells. The energy cutoffs of both dynamic and static dielectric matrix were set to 15 Ry for graphene, SnS_2, $SnSe_2$ and 10 Ry for WS_2. The number of bands for static and dynamic screening and GW self-energy

of unit cell calculations were set to 1000-2000 depending on each system's convergence speed. The Godby-Needs plasmon-pole approximation [33, 69] (PPA) was employed for frequency integration of self-energy in the the Yambo [59] code. For all systems, we used 10Ry for BSE Hamiltonian. The k-point samplings in BSE calculations were set to be the same as GW calculations. Our calculated monolayer WS_2 electronic band gap (2.65 eV) and optical gap (2.06 eV) have converged within 50meV, in good agreement with both previous experimental [20] and first principles [72] results.

5.4 Conclusion

In this work we examined the substrate screening effects on excitonic excitation and recombination lifetime of 2D materials. We applied our previously developed effective polarizablility (χ_{eff}-sum) method to efficiently calculate the electronic and optical spectra for arbitrary 2D interfaces with GW method and solving the BSE. We revealed the underlying mechanism of the non-rigid shifts of 1s and 2s peaks, i.e. why 2s red shifts much stronger than 1s in the presence of substrate screening. We explained this phenomenon through two steps: first, we showed a linear scaling (with a ratio of less than one) between 1s and 2s exciton binding energy both from our first-principle results and 2D Wannier exciton models; second, we presented the linear scaling between electronic gaps and exciton binding energies with a slope close to 1 for 1s and much smaller for 2s exciton while varying substrate screening. We further validated our method by reproducing the 1s and 2s exciton energy shift of WS_2 as a function of layer thickness observed experimentally. Finally we investigated the substrate effects on exciton lifetime and found the 2s exciton lifetime has a stronger dependence on substrates than 1s, due to the relative large change of exciton dipole moment.

Chapter 6

Conclusion

In this thesis, we have developed a comprehensive first-principles framework for evaluating phonon-assisted radiative recombination and exciton dynamics in solids. Starting from a second-quantized effective Hamiltonian that includes exciton-photon and exciton-phonon interactions, we derived the phonon-assisted radiative transition rate using time-dependent second-order perturbation theory within the many-body perturbation theory formalism. Applying this methodology to bulk hexagonal boron nitride (hBN) as a prototypical material, we computed phonon-assisted radiative lifetimes across a wide temperature range and found good agreement with available experimental data. The calculated temperature dependence reveals a non-monotonic behavior at low temperatures, explained by a two-valley model where differences in scattering rates between exciton valleys are critical. At higher temperatures, the lifetime decreases monotonically due to thermal occupation effects, in contrast to the conventional $T^{3/2}$ scaling seen in direct-gap materials.

To capture exciton relaxation under out-of-equilibrium conditions, we developed a real-time Lindblad quantum master equation that, in the semiclassical limit, reduces to the Boltzmann transport equation. This approach enables direct simulation of ultrafast exciton thermalization driven by exciton-phonon interactions. The real-time simulations provide access to exciton relaxation processes and establish a platform for future studies of quantum coherence, dephasing, and spin dynamics in realistic materials.

In addition, we developed an efficient and accurate interpolation technique for dielectric matrices that made quasiparticle energy calculations possible for arbitrarily mismatched interfaces free of strain, which is critical for predicting quasiparticle energies. We analytically demonstrated the connection between different approximate formulations, including the χ_{eff}-sum and χ_0-sum methods, and verified their equivalence at the RPA level. We also quantified the role of off-diagonal elements in the dielectric matrices of substrates and evaluated their impact on the quasiparticle corrections of supported 2D materials. To

overcome limitations in treating interfaces with arbitrary lattice mismatch, we developed a reciprocal-space linear interpolation technique that enables accurate computation of dielectric screening effects without applying artificial strain.

Building on this substrate-screening framework, we investigated the influence of substrates on excitonic properties in 2D materials. By solving the screened Bethe–Salpeter equation on top of screened GW calculations, we explained the observed non-rigid energy shifts of 1s and 2s excitons. We showed that these shifts originate from the combined scaling relations between exciton binding energies, quasiparticle gaps, and exciton dipole moments. Our results reproduced experimental trends for materials like monolayer WS_2 and provided insight into how different excitonic states respond to environmental screening. Furthermore, we demonstrated that 2s exciton radiative lifetimes are more sensitive to substrate effects than 1s states, due to the stronger variation of dipole matrix elements with screening.

Together, these results establish a unified *ab initio* framework for simulating radiative properties and exciton-phonon interactions in solids. The methodology developed in this work lays a solid foundation for future applications in photonics, quantum information, and optoelectronic device.

references

[1] Abidi, Irfan H, Noah Mendelson, Toan Trong Tran, Abhishek Tyagi, Minghao Zhuang, Lu-Tao Weng, Barbaros Özyilmaz, Igor Aharonovich, Milos Toth, and Zhengtang Luo. 2019. Selective defect formation in hexagonal boron nitride. *Advanced Optical Materials* 7(13):1900397.

[2] Abrikosov, Alekseĭ Alekseevich, Lev Petrovich Gorkov, and Igor Ekhielevich Dzyaloshinski. 2012. *Methods of quantum field theory in statistical physics*. Courier Corporation.

[3] Ahn, Junyeong, Sungjoon Park, and Bohm-Jung Yang. 2019. Failure of nielsen-ninomiya theorem and fragile topology in two-dimensional systems with space-time inversion symmetry: application to twisted bilayer graphene at magic angle. *Physical Review X* 9(2):021013.

[4] Antonius, Gabriel, and Steven G. Louie. 2022. Theory of exciton-phonon coupling. *Phys. Rev. B* 105:085111.

[5] Awschalom, David D, Lee C Bassett, Andrew S Dzurak, Evelyn L Hu, and Jason R Petta. 2013. Quantum spintronics: engineering and manipulating atom-like spins in semiconductors. *Science* 339(6124):1174–1179.

[6] Barone, Vincenzo, Maurizio Casarin, Daniel Forrer, Michele Pavone, Mauro Sambi, and Andrea Vittadini. 2009. Role and effective treatment of dispersive forces in materials: Polyethylene and graphite crystals as test cases. *Journal of Computational Chemistry* 30(6):934–939.

[7] Benedict, Lorin X, Eric L Shirley, and Robert B Bohn. 1998. Optical absorption of insulators and the electron-hole interaction: An ab initio calculation. *Physical review letters* 80(20):4514.

[8] Berger, JA, Lucia Reining, and Francesco Sottile. 2010. Ab initio calculations of electronic excitations: Collapsing spectral sums. *Physical Review B—Condensed Matter and Materials Physics* 82(4):041103.

[9] Birowska, Magdalena, Joanna Urban, Michał Baranowski, Duncan K Maude, Paulina Plochocka, and Nevill Gonzalez Szwacki. 2019. The impact of hexagonal boron nitride encapsulation on the structural and vibrational properties of few layer black phosphorus. *Nanotechnology* 30(19):195201.

[10] Bradley, Aaron J, Miguel M. Ugeda, Felipe H da Jornada, Diana Y Qiu, Wei Ruan, Yi Zhang, Sebastian Wickenburg, Alexander Riss, Jiong Lu, Sung-Kwan Mo, et al. 2015. Probing the role of interlayer coupling and coulomb interactions on electronic structure in few-layer mose2 nanostructures. *Nano Letters* 15(4):2594–2599.

[11] Brem, Samuel, August Ekman, Dominik Christiansen, Florian Katsch, Malte Selig, Cedric Robert, Xavier Marie, Bernhard Urbaszek, Andreas Knorr, and Ermin Malic. 2020. Phonon-assisted photoluminescence from indirect excitons in monolayers of transition-metal dichalcogenides. *Nano letters* 20(4):2849–2856.

[12] Bruneval, Fabien. 2005. Exchange and correlation in the electronic structure of solids, from silicon to cuprous oxide: Gw approximation and beyond. *PhD Thesis*.

[13] Cao, Yuan, Valla Fatemi, Ahmet Demir, Shiang Fang, Spencer L Tomarken, Jason Y Luo, Javier D Sanchez-Yamagishi, Kenji Watanabe, Takashi Taniguchi, Efthimios Kaxiras, et al. 2018. Correlated insulator behaviour at half-filling in magic-angle graphene superlattices. *Nature* 556(7699):80.

[14] Cao, Yuan, Valla Fatemi, Shiang Fang, Kenji Watanabe, Takashi Taniguchi, Efthimios Kaxiras, and Pablo Jarillo-Herrero. 2018. Unconventional superconductivity in magic-angle graphene superlattices. *Nature* 556(7699):43–50.

[15] Cassabois, Guillaume, Pierre Valvin, and Bernard Gil. 2016. Hexagonal boron nitride is an indirect bandgap semiconductor. *Nature photonics* 10(4):262–266.

[16] Ceperley, David M, and Berni J Alder. 1980. Ground state of the electron gas by a stochastic method. *Physical Review Letters* 45(7):566.

[17] Chan, Yang-hao, Jonah B Haber, Mit H Naik, Jeffrey B Neaton, Diana Y Qiu, Felipe H da Jornada, and Steven G Louie. 2023. Exciton lifetime and optical line width profile via exciton–phonon interactions: Theory and first-principles calculations for monolayer mos2. *Nano Letters* 23(9):3971–3977.

[18] Chen, Hsiao-Yi, Vatsal A. Jhalani, Maurizia Palummo, and Marco Bernardi. 2019. Ab initio calculations of exciton radiative lifetimes in bulk crystals, nanostructures, and molecules. *Phys. Rev. B* 100:075135.

[19] Chen, Hsiao-Yi, Davide Sangalli, and Marco Bernardi. 2020. Exciton-phonon interaction and relaxation times from first principles. *Phys. Rev. Lett.* 125:107401.

[20] Chernikov, Alexey, Timothy C Berkelbach, Heather M Hill, Albert Rigosi, Yilei Li, Ozgur Burak Aslan, David R Reichman, Mark S Hybertsen, and Tony F Heinz. 2014. Exciton binding energy and nonhydrogenic rydberg series in monolayer ws 2. *Physical Review Letters* 113(7):076802.

[21] Cho, Yeongsu, and Timothy C Berkelbach. 2018. Environmentally sensitive theory of electronic and optical transitions in atomically thin semiconductors. *Physical Review B* 97(4):041409.

[22] Choi, Jin-Ho, Ping Cui, Haiping Lan, and Zhenyu Zhang. 2015. Linear scaling of the exciton binding energy versus the band gap of two-dimensional materials. *Physical Review Letters* 115(6):066403.

[23] Deslippe, Jack, Georgy Samsonidze, David A Strubbe, Manish Jain, Marvin L Cohen, and Steven G Louie. 2012. Berkeleygw: A massively parallel computer package for the calculation of the quasiparticle and optical properties of materials and nanostructures. *Computer Physics Communications* 183(6):1269–1289.

[24] Felipe, H, Diana Y Qiu, and Steven G Louie. 2017. Nonuniform sampling schemes of the brillouin zone for many-electron perturbation-theory calculations in reduced dimensionality. *Physical Review B* 95(3):035109.

[25] Fetter, Alexander L, and John Dirk Walecka. 2012. *Quantum theory of many-particle systems*. Courier Corporation.

[26] Galvani, Thomas, Fulvio Paleari, Henrique PC Miranda, Alejandro Molina-Sánchez, Ludger Wirtz, Sylvain Latil, Hakim Amara, and François Ducastelle. 2016. Excitons in boron nitride single layer. *Physical Review B* 94(12):125303.

[27] Gao, Weiwei, Weiyi Xia, Xiang Gao, and Peihong Zhang. 2016. Speeding up gw calculations to meet the challenge of large scale quasiparticle predictions. *Scientific Reports* 6:36849.

[28] Gell-Mann, Murray, and Francis Low. 1951. Bound states in quantum field theory. *Phys. Rev.* 84:350–354.

[29] Gerace, Dario, and Lucio Claudio Andreani. 2007. Quantum theory of exciton-photon coupling in photonic crystal slabs with embedded quantum wells. *Phys. Rev. B* 75:235325.

[30] Giannozzi, P, O Andreussi, T Brumme, O Bunau, M Buongiorno Nardelli, M Calandra, R Car, C Cavazzoni, D Ceresoli, M Cococcioni, N Colonna, I Carnimeo, A Dal Corso, S de Gironcoli, P Delugas, R A DiStasio, A Ferretti, A Floris, G Fratesi, G Fugallo, R Gebauer, U Gerstmann, F Giustino, T Gorni, J Jia, M Kawamura, H-Y Ko, A Kokalj, E Küçükbenli, M Lazzeri, M Marsili, N Marzari, F Mauri, N L Nguyen, H-V Nguyen, A Otero de-la Roza, L Paulatto, S Poncé, D Rocca, R Sabatini, B Santra, M Schlipf, A P Seitsonen, A Smogunov, I Timrov, T Thonhauser, P Umari, N Vast, X Wu, and S Baroni. 2017. Advanced capabilities for materials modelling with quantum ESPRESSO. *Journal of Physics: Condensed Matter* 29(46):465901.

[31] Giannozzi, Paolo, Stefano Baroni, Nicola Bonini, Matteo Calandra, Roberto Car, Carlo Cavazzoni, Davide Ceresoli, Guido L Chiarotti, Matteo Cococcioni, Ismaila Dabo, et al. 2009. Quantum espresso: a modular and open-source software project for quantum simulations of materials. *Journal of Physics: Condensed Matter* 21(39): 395502.

[32] Giustino, Feliciano. 2017. Electron-phonon interactions from first principles. *Rev. Mod. Phys.* 89:015003.

[33] Godby, Rex W, and RJ Needs. 1989. Metal-insulator transition in kohn-sham theory and quasiparticle theory. *Physical Review Letters* 62(10):1169.

[34] Gottscholl, Andreas, Mehran Kianinia, Victor Soltamov, Sergei Orlinskii, Georgy Mamin, Carlo Bradac, Christian Kasper, Klaus Krambrock, Andreas Sperlich, Milos Toth, Igor Aharonovich, and Vladimir Dyakonov. 2020. Initialization and read-out of intrinsic spin defects in a van der Waals crystal at room temperature. *Nature Materials* 19(5):540–545.

[35] Govoni, Marco, and Giulia Galli. 2015. Large scale gw calculations. *Journal of Chemical Theory and Computation* 11(6):2680–2696.

[36] Grimme, Stefan. 2006. Semiempirical gga-type density functional constructed with a long-range dispersion correction. *Journal of Computational Chemistry* 27(15):1787–1799.

[37] Guo, Chunhao, Gabriele Riva, Jacopo Simoni, Junqing Xu, and Yuan Ping. 2025. Phonon-assisted radiative lifetimes and exciton dynamics from first principles. *arXiv preprint arXiv:2504.18071*.

[38] Guo, Chunhao, Junqing Xu, and Yuan Ping. 2021. Substrate effect on excitonic shift and radiative lifetime of two-dimensional materials. *Journal of Physics: Condensed Matter* 33(23):234001.

[39] Guo, Chunhao, Junqing Xu, Dario Rocca, and Yuan Ping. 2020. Substrate screening approach for quasiparticle energies of two-dimensional interfaces with lattice mismatch. *Physical Review B* 102(20):205113.

[40] Hamann, DR. 2013. Optimized norm-conserving vanderbilt pseudopotentials. *Physical Review B* 88(8):085117.

[41] He, Yu-Ming, Genevieve Clark, John R Schaibley, Yu He, Ming-Cheng Chen, Yu-Jia Wei, Xing Ding, Qiang Zhang, Wang Yao, Xiaodong Xu, et al. 2015. Single quantum emitters in monolayer semiconductors. *Nature Nanotechnology* 10(6):497–502.

[42] Hedin, Lars. 1965. New method for calculating the one-particle green's function with application to the electron-gas problem. *Phys. Rev.* 139:A796–A823.

[43] Hedin, Lars, and Stig Lundqvist. 1970. Effects of electron-electron and electron-phonon interactions on the one-electron states of solids. In *Solid state physics*, vol. 23, 1–181. Elsevier.

[44] Hybertsen, Mark S, and Steven G Louie. 1987. Ab initio static dielectric matrices from the density-functional approach. i. formulation and application to semiconductors and insulators. *Physical Review B* 35(11):5585.

[45] Im, JS, A Moritz, F Steuber, V Härle, F Scholz, and A Hangleiter. 1997. Radiative carrier lifetime, momentum matrix element, and hole effective mass in gan. *Applied physics letters* 70(5):631–633.

[46] Jackson, John David. 1999. Classical electrodynamics.

[47] Jiang, Zeyu, Zhirong Liu, Yuanchang Li, and Wenhui Duan. 2017. Scaling universality between band gap and exciton binding energy of two-dimensional semiconductors. *Physical Review Letters* 118(26):266401.

[48] Kammerlander, David, Silvana Botti, Miguel AL Marques, Andrea Marini, and Claudio Attaccalite. 2012. Speeding up the solution of the bethe-salpeter equation by a double-grid method and wannier interpolation. *Physical Review B* 86(12):125203.

[49] Katzer, Manuel, Malte Selig, Lukas Sigl, Mirco Troue, Johannes Figueiredo, Jonas Kiemle, Florian Sigger, Ursula Wurstbauer, Alexander W. Holleitner, and Andreas Knorr. 2023. Exciton-phonon scattering: Competition between the bosonic and fermionic nature of bound electron-hole pairs. *Phys. Rev. B* 108:L121102.

[50] Krukau, Aliaksandr V, Oleg A Vydrov, Artur F Izmaylov, and Gustavo E Scuseria. 2006. Influence of the exchange screening parameter on the performance of screened hybrid functionals. *The Journal of Chemical Physics* 125(22):224106.

[51] Kubota, Yoichi, Kenji Watanabe, Osamu Tsuda, and Takashi Taniguchi. 2007. Deep ultraviolet light-emitting hexagonal boron nitride synthesized at atmospheric pressure. *Science* 317(5840):932–934.

[52] Lasher, Gordon, and Frank Stern. 1964. Spontaneous and stimulated recombination radiation in semiconductors. *Phys. Rev.* 133:A553–A563.

[53] Laturia, Akash, Maarten L Van de Put, and William G Vandenberghe. 2018. Dielectric properties of hexagonal boron nitride and transition metal dichalcogenides: from monolayer to bulk. *npj 2D Materials and Applications* 2(1):6.

[54] Lechifflart, Pierre, Fulvio Paleari, Davide Sangalli, and Claudio Attaccalite. 2023. First-principles study of luminescence in hexagonal boron nitride single layer: Exciton-phonon coupling and the role of substrate. *Phys. Rev. Mater.* 7:024006.

[55] Lee, Hyungjun, Samuel Poncé, Kyle Bushick, Samad Hajinazar, Jon Lafuente-Bartolome, Joshua Leveillee, Chao Lian, Jae-Mo Lihm, Francesco Macheda, Hitoshi Mori, et al. 2023. Electron–phonon physics from first principles using the epw code. *npj Computational Materials* 9(1):156.

[56] Liu, Zhen-Fei, Felipe H da Jornada, Steven G Louie, and Jeffrey B Neaton. 2019. Accelerating gw-based energy level alignment calculations for molecule–metal interfaces using a substrate screening approach. *Journal of Chemical Theory and Computation* 15(7):4218–4227.

[57] Macfarlane, G. G., T. P. McLean, J. E. Quarrington, and V. Roberts. 1958. Fine structure in the absorption-edge spectrum of si. *Phys. Rev.* 111:1245–1254.

[58] MARADUDIN, A. A., and S. H. VOSKO. 1968. Symmetry properties of the normal vibrations of a crystal. *Rev. Mod. Phys.* 40:1–37.

[59] Marini, Andrea, Conor Hogan, Myrta Grüning, and Daniele Varsano. 2009. Yambo: an ab initio tool for excited state calculations. *Computer Physics Communications* 180(8):1392–1403.

[60] Mattis, DC, and J-P Gallinar. 1984. What is the mass of an exciton? *Physical Review Letters* 53(14):1391.

[61] Mendelson, Noah, Dipankar Chugh, Jeffrey R Reimers, Tin S Cheng, Andreas Gottscholl, Hu Long, Christopher J Mellor, Alex Zettl, Vladimir Dyakonov, Peter H Beton, Sergei V Novikov, Chennupati Jagadish, Hark Hoe Tan, Michael J Ford, Milos Toth, Carlo Bradac, and Igor Aharonovich. 2020. Identifying carbon as the source of visible single-photon emission from hexagonal boron nitride. *Nature Materials*.

[62] Naik, Mit H, and Manish Jain. 2018. Substrate screening effects on the quasiparticle band gap and defect charge transition levels in mos 2. *Physical Review Materials* 2(8): 084002.

[63] Nguyen, Ngoc Linh, Nicola Colonna, Andrea Ferretti, and Nicola Marzari. 2018. Koopmans-compliant spectral functionals for extended systems. *Physical Review X* 8(2):021051.

[64] Noffsinger, Jesse, Emmanouil Kioupakis, Chris G. Van de Walle, Steven G. Louie, and Marvin L. Cohen. 2012. Phonon-assisted optical absorption in silicon from first principles. *Phys. Rev. Lett.* 108:167402.

[65] Novoselov, KS, A Mishchenko, A Carvalho, and AH Castro Neto. 2016. 2d materials and van der waals heterostructures. *Science* 353(6298):aac9439.

[66] Ohba, Nobuko, Kazutoshi Miwa, Naoyuki Nagasako, and Atsuo Fukumoto. 2001. First-principles study on structural, dielectric, and dynamical properties for three bn polytypes. *Phys. Rev. B* 63:115207.

[67] Olsen, Thomas, Simone Latini, Filip Rasmussen, and Kristian S Thygesen. 2016. Simple screened hydrogen model of excitons in two-dimensional materials. *Physical Review Letters* 116(5):056401.

[68] Onida, Giovanni, Lucia Reining, and Angel Rubio. 2002. Electronic excitations: density-functional versus many-body green's-function approaches. *Rev. Mod. Phys.* 74:601–659.

[69] Oschlies, A, RW Godby, and RJ Needs. 1995. Gw self-energy calculations of carrier-induced band-gap narrowing in n-type silicon. *Physical Review B* 51(3):1527.

[70] Paleari, Fulvio. 2019. First-principles approaches to the description of indirect absorption and luminescence spectroscopy: exciton-phonon coupling in hexagonal boron nitride. *PhD Thesis*.

[71] Paleari, Fulvio, and Andrea Marini. 2022. Exciton-phonon interaction calls for a revision of the "exciton" concept. *Phys. Rev. B* 106:125403.

[72] Palummo, Maurizia, Marco Bernardi, and Jeffrey C Grossman. 2015. Exciton radiative lifetimes in two-dimensional transition metal dichalcogenides. *Nano Letters* 15(5): 2794–2800.

[73] Patrick, Christopher E, and Feliciano Giustino. 2014. Unified theory of electron–phonon renormalization and phonon-assisted optical absorption. *Journal of Physics: Condensed Matter* 26(36):365503.

[74] Perdew, John P, Kieron Burke, and Matthias Ernzerhof. 1996. Generalized gradient approximation made simple. *Physical Review Letters* 77(18):3865.

[75] Pham, T Anh, Huy-Viet Nguyen, Dario Rocca, and Giulia Galli. 2013. G w calculations using the spectral decomposition of the dielectric matrix: Verification, validation, and comparison of methods. *Physical Review B* 87(15):155148.

[76] Pierret, Aurelie, David Mele, Holger Graef, Jose Palomo, Takashi Taniguchi, Kenji Watanabe, Y Li, Bérangère Toury, Catherine Journet, Philippe Steyer, et al. 2022. Dielectric permittivity, conductivity and breakdown field of hexagonal boron nitride. *Materials Research Express* 9(6):065901.

[77] Ping, Yuan, Dario Rocca, and Giulia Galli. 2013. Electronic excitations in light absorbers for photoelectrochemical energy conversion: first principles calculations based on many body perturbation theory. *Chemical Society Reviews* 42(6):2437–2469.

[78] Ping, Yuan, Dario Rocca, Deyu Lu, and Giulia Galli. 2012. Ab initio calculations of absorption spectra of semiconducting nanowires within many-body perturbation theory. *Physical Review B* 85(3):035316.

[79] Press, William H, Saul A Teukolsky, William T Vetterling, and Brian P Flannery. 2007. *Numerical recipes 3rd edition: The art of scientific computing*. Cambridge University Press.

[80] Qin, Wei, Leiqiang Li, and Zhenyu Zhang. 2019. Chiral topological superconductivity arising from the interplay of geometric phase and electron correlation. *Nature Physics* 15(8):796–802.

[81] Qin, Wei, and Zhenyu Zhang. 2014. Persistent ferromagnetism and topological phase transition at the interface of a superconductor and a topological insulator. *Physical Review Letters* 113(26):266806.

[82] Qiu, Diana Y., Ting Cao, and Steven G. Louie. 2015. Nonanalyticity, valley quantum phases, and lightlike exciton dispersion in monolayer transition metal dichalcogenides: Theory and first-principles calculations. *Phys. Rev. Lett.* 115:176801.

[83] Qiu, Diana Y., Felipe H. da Jornada, and Steven G. Louie. 2013. Optical spectrum of mos_2: Many-body effects and diversity of exciton states. *Phys. Rev. Lett.* 111:216805.

[84] Qiu, Diana Y, Felipe H da Jornada, and Steven G Louie. 2017. Environmental screening effects in 2d materials: renormalization of the bandgap, electronic structure, and optical spectra of few-layer black phosphorus. *Nano Letters* 17(8):4706–4712.

[85] Quinton, Joshua, Mayada Fadel, Junqing Xu, Adela Habib, Mani Chandra, Yuan Ping, and Ravishankar Sundararaman. 2025. Magnetic-field dependence of spin-phonon relaxation and dephasing due to g-factor fluctuations from first principles. *Phys. Rev. B* 111:115113.

[86] Raja, Archana, Andrey Chaves, Jaeeun Yu, Ghidewon Arefe, Heather M Hill, Albert F Rigosi, Timothy C Berkelbach, Philipp Nagler, Christian Schüller, Tobias Korn, et al. 2017. Coulomb engineering of the bandgap and excitons in two-dimensional materials. *Nature Communications* 8(1):1–7.

[87] Resta, R, and A Baldereschi. 1981. Dielectric matrices and local fields in polar semiconductors. *Physical Review B* 23(12):6615.

[88] Riis-Jensen, Anders C, Morten N Gjerding, Saverio Russo, and Kristian S Thygesen. 2020. Anomalous exciton rydberg series in two-dimensional semiconductors on high-κ dielectric substrates. *Physical Review B* 102(20):201402.

[89] Rocca, Dario, Yuan Ping, Ralph Gebauer, and Giulia Galli. 2012. Solution of the bethe-salpeter equation without empty electronic states: Application to the absorption spectra of bulk systems. *Physical Review B* 85(4):045116.

[90] Rohlfing, Michael, and Steven G Louie. 2000. Electron-hole excitations and optical spectra from first principles. *Physical Review B* 62(8):4927.

[91] Rosati, Roberto, Fabrizio Dolcini, and Fausto Rossi. 2015. Electron-phonon coupling in metallic carbon nanotubes: Dispersionless electron propagation despite dissipation. *Phys. Rev. B* 92:235423.

[92] Rosati, Roberto, Rita Claudia Iotti, Fabrizio Dolcini, and Fausto Rossi. 2014. Derivation of nonlinear single-particle equations via many-body lindblad superoperators: A density-matrix approach. *Phys. Rev. B* 90:125140.

[93] Rosati, Roberto, Koloman Wagner, Samuel Brem, Raul Perea-Causin, Edith Wietek, Jonas Zipfel, Jonas D Ziegler, Malte Selig, Takashi Taniguchi, Kenji Watanabe, et al. 2020. Temporal evolution of low-temperature phonon sidebands in transition metal dichalcogenides. *ACS Photonics* 7(10):2756–2764.

[94] Roux, Sébastien, Christophe Arnold, Fulvio Paleari, Lorenzo Sponza, Eli Janzen, James H. Edgar, Bérangère Toury, Catherine Journet, Vincent Garnier, Philippe Steyer, Takashi Taniguchi, Kenji Watanabe, Fran çois Ducastelle, Annick Loiseau, and Julien Barjon. 2021. Radiative lifetime of free excitons in hexagonal boron nitride. *Phys. Rev. B* 104:L161203.

[95] Rozzi, Carlo A., Daniele Varsano, Andrea Marini, Eberhard K. U. Gross, and Angel Rubio. 2006. Exact coulomb cutoff technique for supercell calculations. *Phys. Rev. B* 73:205119.

[96] Rozzi, Carlo A, Daniele Varsano, Andrea Marini, Eberhard KU Gross, and Angel Rubio. 2006. Exact coulomb cutoff technique for supercell calculations. *Physical Review B* 73(20):205119.

[97] Sajid, A, Michael J Ford, and Jeffrey R Reimers. 2020. Single-photon emitters in hexagonal boron nitride: a review of progress. *Reports on Progress in Physics* 83(4): 044501.

[98] Sakurai, Jun John, and Jim Napolitano. 2020. *Modern quantum mechanics*. Cambridge University Press.

[99] Sangalli, Davide, Andrea Ferretti, Henrique Miranda, Claudio Attaccalite, Ivan Marri, Elena Cannuccia, Pedro Melo, Margherita Marsili, Fulvio Paleari, Antimo Marrazzo, Gianluca Prandini, Pietro Bonfà, Michael O. Atambo, Fabio Affinito, Maurizia Palummo, Alejandro Molina Sanchez, Conor Hogan, Myrta Grüning, Daniele

Varsano, and Andrea Marini. 2019. Many-body perturbation theory calculations using the yambo code. *Journal of Physics: Condensed Matter* 31(32):325902.

[100] Schwinger, Julian. 1951. On the green's functions of quantized fields. ii. *Proceedings of the National Academy of Sciences* 37(7):455–459.

[101] Segura, A, Lluís Artús, Ramón Cuscó, Takashi Taniguchi, Guillaume Cassabois, and Bernard Gil. 2018. Natural optical anisotropy of h-bn: Highest giant birefringence in a bulk crystal through the mid-infrared to ultraviolet range. *Physical Review Materials* 2(2):024001.

[102] Shi, Hongliang, Hui Pan, Yong-Wei Zhang, and Boris I Yakobson. 2013. Quasiparticle band structures and optical properties of strained monolayer mos 2 and ws 2. *Physical Review B* 87(15):155304.

[103] Smart, Tyler J, Kejun Li, Junqing Xu, and Yuan Ping. 2020. Intersystem crossing and exciton-defect coupling of spin defects in hexagonal boron nitride. *arXiv preprint arXiv:2009.02830*.

[104] Smart, Tyler J, Feng Wu, Marco Govoni, and Yuan Ping. 2018. Fundamental principles for calculating charged defect ionization energies in ultrathin two-dimensional materials. *Physical Review Materials* 2(12):124002.

[105] Song, Zhida, Zhijun Wang, Wujun Shi, Gang Li, Chen Fang, and B Andrei Bernevig. 2019. All magic angles in twisted bilayer graphene are topological. *Physical Review Letters* 123(3):036401.

[106] Stefanucci, Gianluca, and Robert Van Leeuwen. 2013. *Nonequilibrium many-body theory of quantum systems: a modern introduction*. Cambridge University Press.

[107] Stein, Tamar, Helen Eisenberg, Leeor Kronik, and Roi Baer. 2010. Fundamental gaps in finite systems from eigenvalues of a generalized kohn-sham method. *Physical Review Letters* 105(26):266802.

[108] Strinati, Giancarlo. 1988. Application of the green's functions method to the study of the optical properties of semiconductors. *La Rivista del Nuovo Cimento (1978-1999)* 11(12):1–86.

[109] Sun, Zhengbo, Hanhan Xie, Siying Tang, Xue-Feng Yu, Zhinan Guo, Jundong Shao, Han Zhang, Hao Huang, Huaiyu Wang, and Paul K Chu. 2015. Ultrasmall black phosphorus quantum dots: synthesis and use as photothermal agents. *Angewandte Chemie International Edition* 54(39):11526–11530.

[110] Tiwari, Sabyasachi, Emmanouil Kioupakis, José Menendez, and Feliciano Giustino. 2024. Unified theory of optical absorption and luminescence including both direct and phonon-assisted processes. *Phys. Rev. B* 109:195127.

[111] Tran, Toan Trong, Kerem Bray, Michael J Ford, Milos Toth, and Igor Aharonovich. 2016. Quantum emission from hexagonal boron nitride monolayers. *Nature Nanotechnology* 11(1):37.

[112] Trolle, Mads L, Thomas G Pedersen, and Valerie Véniard. 2017. Model dielectric function for 2d semiconductors including substrate screening. *Scientific Reports* 7: 39844.

[113] Turiansky, M E, A Alkauskas, and C G Van de Walle. 2020. Spinning up quantum defects in 2D materials. *Nature Materials* 19(5):487–489.

[114] Ugeda, Miguel M, Aaron J Bradley, Su-Fei Shi, H Felipe, Yi Zhang, Diana Y Qiu, Wei Ruan, Sung-Kwan Mo, Zahid Hussain, Zhi-Xun Shen, et al. 2014. Giant bandgap renormalization and excitonic effects in a monolayer transition metal dichalcogenide semiconductor. *Nature Materials* 13(12):1091–1095.

[115] Van Setten, MJ, Matteo Giantomassi, Eric Bousquet, Matthieu J Verstraete, Don R Hamann, Xavier Gonze, and G-M Rignanese. 2018. The pseudodojo: Training and grading a 85 element optimized norm-conserving pseudopotential table. *Computer Physics Communications* 226:39–54.

[116] Vuong, T. Q. P., G. Cassabois, P. Valvin, S. Liu, J. H. Edgar, and B. Gil. 2017. Exciton-phonon interaction in the strong-coupling regime in hexagonal boron nitride. *Phys. Rev. B* 95:201202.

[117] Waldecker, Lutz, Archana Raja, Malte Rösner, Christina Steinke, Aaron Bostwick, Roland J Koch, Chris Jozwiak, Takashi Taniguchi, Kenji Watanabe, Eli Rotenberg, et al. 2019. Rigid band shifts in two-dimensional semiconductors through external dielectric screening. *Physical Review Letters* 123(20):206403.

[118] Wang, Dan, and Ravishankar Sundararaman. 2019. Substrate effects on charged defects in two-dimensional materials. *Physical Review Materials* 3(8):083803.

[119] Wang, Hui, Xianzhu Yang, Wei Shao, Shichuan Chen, Junfeng Xie, Xiaodong Zhang, Jun Wang, and Yi Xie. 2015. Ultrathin black phosphorus nanosheets for efficient singlet oxygen generation. *Journal of the American Chemical Society* 137(35):11376–11382.

[120] Weng, Mouyi, Sibai Li, Jiaxin Zheng, Feng Pan, and Lin-Wang Wang. 2018. Wannier koopmans method calculations of 2d material band gaps. *The Journal of Physical Chemistry Letters* 9(2):281–285. PMID: 29284265.

[121] Wick, G. C. 1950. The evaluation of the collision matrix. *Phys. Rev.* 80:268–272.

[122] Winther, Kirsten T, and Kristian S Thygesen. 2017. Band structure engineering in van der waals heterostructures via dielectric screening: the gδw method. *2D Materials* 4(2):025059.

[123] Wolf, SA, DD Awschalom, RA Buhrman, JM Daughton, von S von Molnár, ML Roukes, A Yu Chtchelkanova, and DM Treger. 2001. Spintronics: a spin-based electronics vision for the future. *Science* 294(5546):1488–1495.

[124] Wu, Feng, Andrew Galatas, Ravishankar Sundararaman, Dario Rocca, and Yuan Ping. 2017. First-principles engineering of charged defects for two-dimensional quantum technologies. *Physical Review Materials* 1(7):071001.

[125] Wu, Feng, Dario Rocca, and Yuan Ping. 2019. Dimensionality and anisotropicity dependence of radiative recombination in nanostructured phosphorene. *Journal of Materials Chemistry C* 7(41):12891–12897.

[126] Wu, Feng, Tyler J. Smart, Junqing Xu, and Yuan Ping. 2019. Carrier recombination mechanism at defects in wide band gap two-dimensional materials from first principles. *Physical Review B* 100:081407.

[127] Wu, Feng, Tyler J Smart, Junqing Xu, and Yuan Ping. 2019. Carrier recombination mechanism at defects in wide band gap two-dimensional materials from first principles. *Physical Review B* 100(8):081407.

[128] Xu, Junqing, Adela Habib, Sushant Kumar, Feng Wu, Ravishankar Sundararaman, and Yuan Ping. 2020. Spin-phonon relaxation from a universal ab initio density-matrix approach. *Nature communications* 11(1):2780.

[129] Xu, Junqing, Adela Habib, Ravishankar Sundararaman, and Yuan Ping. 2021. Ab initio ultrafast spin dynamics in solids. *Phys. Rev. B* 104:184418.

[130] Xu, Junqing, Kejun Li, Uyen N Huynh, Mayada Fadel, Jinsong Huang, Ravishankar Sundararaman, Valy Vardeny, and Yuan Ping. 2024. How spin relaxes and dephases in bulk halide perovskites. *Nat. Commun.* 15(1):188.

[131] Xu, Junqing, and Yuan Ping. 2024. Ab initio predictions of spin relaxation, dephasing, and diffusion in solids. *Journal of Chemical Theory and Computation* 20(2):492–512. PMID: 38157422, https://doi.org/10.1021/acs.jctc.3c00598.

[132] Xuan, Fengyuan, Yifeng Chen, and Su Ying Quek. 2019. Quasiparticle levels at large interface systems from many-body perturbation theory: the xaf-gw method. *Journal of Chemical Theory and Computation* 15(6):3824–3835.

[133] Yan, Jun, Kristian S Thygesen, and Karsten W Jacobsen. 2011. Nonlocal screening of plasmons in graphene by semiconducting and metallic substrates: first-principles calculations. *Physical Review Letters* 106(14):146803.

[134] Yang, Deng-Ke, and Shin-Tson Wu. 2014. *Fundamentals of liquid crystal devices*. John Wiley & Sons.

[135] Yang, XL, SH Guo, FT Chan, KW Wong, and WY Ching. 1991. Analytic solution of a two-dimensional hydrogen atom. i. nonrelativistic theory. *Physical Review A* 43(3): 1186.

[136] Yuan, Long, and Libai Huang. 2015. Exciton dynamics and annihilation in ws 2 2d semiconductors. *Nanoscale* 7(16):7402–7408.

[137] Zheng, Huihuo, Marco Govoni, and Giulia Galli. 2019. Dielectric-dependent hybrid functionals for heterogeneous materials. *Physical Review Materials* 3(7):073803.

[138] Žutić, Igor, Jaroslav Fabian, and S Das Sarma. 2004. Spintronics: Fundamentals and applications. *Reviews of Modern Physics* 76(2):323.